Development of a Punching Technique for Ductile Fracture Testing Over a Wide Range of Stress States and Strain Rates

by

Carey Leroy Walters

B.S. Mechanical Engineering
University of Massachusetts at Amherst, 2001

SUBMITTED TO THE DEPARTMENT OF MECHANICAL ENGINEERING
IN PARTIAL FULFILLMENT OF THE REQUIREMENST FOR THE DEGREE OF

DOCTOR OF PHILOSOPHY IN MECHANICAL ENGINEERING
AT THE
MASSACHUSETTS INSTITUTE OF TECHNOLOGY

September, 2009

Signature of Author……………………………………………………………………….
Department of Mechanical Engineering
August, 2009

Certified by……………………………………………………………...…………………
Tomasz Wierzbicki
Professor of Applied Mechanics
Thesis Supervisor

Accepted by ……………………………………………………………………..……...
David E. Hardt
Professor, Mechanical Engineering
Chairman, Department Committee on Graduate Students

Development of a Punching Technique for Ductile Fracture Testing Over a Wide Range of Stress States and Strain Rates

by

Carey Leroy Walters

Submitted to the Department of Mechanical Engineering
On August 6, 2009 in Partial Fulfillment of the
Requirements for the Degree of Doctor of Philosophy in
Mechanical Engineering

Abstract

Advanced High Strength Steels (AHSS) are becoming increasingly popular in automotive design because of possible weight savings due to the high strength. However, traditional methods are not capable of predicting fracture in AHSS, leading to expensive redesign due to poor prediction of stamping and crashworthiness. Many scenarios in which fracture is a concern in automotive applications are in the range of quasi-static through intermediate strain rates (up to 850/s). Studies with high-speed hydraulic equipment and Hopkinson bars have shown that there is a dependence of fracture on strain rate, and that it may be a complex relationship. Recent work on quasi-static fracture has shown that the dependence of ductility on the stress triaxiality and Lode parameter must be accounted for, but this dependence has not been investigated in the dynamic range. The aim of the current thesis is to contribute a new methodology based on an instrumented drop tower that will allow for testing of ductility for low to intermediate strain rates over stress triaxialities ranging from one third to two thirds. The methodology begins with a very in-depth understanding of plasticity based on multi-axial experiments, continues with qusi-static punching experiments, and finishes with dynamic punching experiments. In the punching experiments, a thin sheet is clamped into a circular die and loaded in membrane tension through out-of-plane punching. The state of stress is changed from equi-biaxial to approximately uniaxial through the introduction of cutouts in the sides the membrane specimen. The quasi-static punching experiments are verified against a multi-axial fracture testing technique previously demonstrated by other researchers.

From application of the aforementioned methodology to a steels used in sheet metal forming and crashworthiness, the current thesis has shed insight into the dependence of ductility on stress triaxiality, Lode parameter, and strain rate for quasi-static to intermediate strain rates.

Thesis Supervisor: Tomasz Wierzbicki
Title: Professor of Applied Mechanics

Biographical Note

Mr. Carey Walters graduated with a Bachelor's of Science in Mechanical Engineering from the University of Massachusetts at Amherst. Immediately following graduation, he joined the Loads and Criteria/Survivability and Vulnerability group at Sikorsky Aircraft Corporation. While working at Sikorsky Aircraft, Mr. Walters' responsibilities focused primarily on development and demonstration of finite element analysis for application to the analysis of crashing helicopters. Mr. Walters also analyzed helicopter ground loads and fatigue characterization due to landing cycles of helicopters. After four years working for Sikorsky Aircraft, Mr. Walters returned to Academia to pursue a Ph.D. under the direction of Professor Tomasz Wierzbicki at MIT in September, 2004. Since he has been at MIT, Mr. Walters has been a research assistant for nine semesters under the direction of Professor Wierzbicki. Mr. Walters has also been a Teaching Assistant for a first year graduate-level class in Mechanical Engineering, for which he was awarded the GSC Teaching Award under the recommendation of the course instructor and multiple students. Capitalizing on his aerospace experience before MIT, Mr. Walters has completed multiple projects and papers with Professor Chiara Bisagni of the Politecnico di Milano (Polytechnic University of Milan, Italy) on deformation and failure of composite materials and structures. Mr. Walters has also represented Professor Wierzbicki's laboratory as a consultant to Ferrari.

Acknowledgements

Table of Contents

List of Figures

14

15

List of Tables

Symbols and Acronyms

β	Angle describing the ratio of the vertical force to the horizontal, $\beta \equiv \tan^{-1} \dfrac{F_V}{F_H}$
δ	Deflection of the center point of a punch into a plate
$\dot{\delta}$	Velocity of the center point of a punch into a plate $d\delta/dt$
$\ddot{\delta}$	Acceleration of the center point (and drop mass) of a punch into a plate $d\dot{\delta}/dt$
Δt	Discrete time step used for simulating a punch experiment
ε	Strain
$\dot{\varepsilon}$	Strain rate, $d\varepsilon/dt$
$\dot{\varepsilon}_0$	Reference strain rate for Cowper-Symonds plasticity law
$\dot{\bar{\varepsilon}}^p$	Effective plastic strain rate, $d\bar{\varepsilon}^p/dt$
$\dot{\bar{\varepsilon}}^p_{SpAvg}$	Spatial average of strain rate over the entire specimen
$\dot{\bar{\varepsilon}}^p_{TAvg}$	Temporal and spatial average of strain rate over specimen, $\dot{\bar{\varepsilon}}^p_{TAvg} = \dfrac{1}{t_f} \displaystyle\int_0^{t_f} \dot{\bar{\varepsilon}}^p_{SpAvg} dt$
$\bar{\varepsilon}_f$	Effective strain to failure
$\bar{\varepsilon}^p$	Effective plastic strain
η	Stress triaxiality, $\sigma_m/\bar{\sigma}$
θ	Tangential coordinate in a circular plate
$\bar{\theta}$	Lode angle
ξ	Third invariant of the stress tensor, $\left[\dfrac{27}{2} (\sigma_I - \sigma_m)(\sigma_{II} - \sigma_m)(\sigma_{III} - \sigma_m) \right]^{1/3}$
ξ_0	Dimensionless punch radius, R_b/R_0
ξ_c	Dimensionless contact radius, R_c/R_0
σ	Cauchy stress
σ_m	Hydrostatic tension, $\dfrac{1}{3}(\sigma_I + \sigma_{II} + \sigma_{III})$
$\sigma_I, \sigma_{II}, \sigma_{III}$	Principal stresses with $\sigma_I \geq \sigma_{II} \geq \sigma_{III}$
σ_0	Plastic flow stress for a rigid-perfectly-plastic plasticity model
σ^0	Static yield stress for comparison against dynamic yield stress
σ_{VM}	Von Mises stress, $\sqrt{\dfrac{1}{2} \left[(\sigma_I - \sigma_{II})^2 + (\sigma_{II} - \sigma_{III})^2 + (\sigma_{III} - \sigma_I)^2 \right]}$
$\bar{\sigma}$	Equivalent stress, most often Hill equivalent stress
ψ	Contact angle between a hemispherical punch and an indented plate

A_0	Initial cross-sectional area of the specimen
c_1, c_2, c_3	Calibration constants for modified Mohr-Coulomb fracture criterion
C	Coefficient for the power hardening plasticity law
F, G, H	Coefficients for Hill plasticity model corresponding to normal terms
F_H	Horizontal force
F_V	Vertical force
L, M, N	Coefficients for Hill plasticity model corresponding to shear terms
M	Mass
N_0	Generalized membrane stress
n_{CS}	Calibration constant for Cowper-Symonds plasticity law
n_H	Exponent for the power hardening plasticity law
P	Vertical force applied to a punch
r	Radial coordinate in a circular plate
R	Yield stress ratio, $R(\dot{\bar{\varepsilon}}^p) \equiv \dfrac{\bar{\sigma}}{\sigma^0}$
R_b	Radius of punch for Hasek test
R_c	Radius of contact between a hemispherical punch and an indented plate
R_N	Radius of cutouts in sides of plate for Hasek test
R_0	Radius of die for Hasek test
t	Time
t_0	Initial thickness of a plate
t_f	Time at first fracture
V_0	Impact velocity of dynamic experiments
X	Width coordinate of the specimens
Y	Hight coordinate of the specimens

AHSS	Advanced High Strength Steel
DIC	Digital Image Correlation
DP780	Dual-Phase AHSS with an ultimate tensile strength of at least 780 MPa
FEA	Finite Element Analysis
FFLD	Fracture Forming Limit Diagram
FLD	Forming Limit Diagram
ICL	Impact and Crashworthiness Laboratory
IPPT	Polish Academy of Sciences
MIT	Massachusetts Institute of Technology
MMC	Modified Mohr-Coloumb fracture criterion
SHB	Split Hopkinson Bar; also known as Kolsky bar
TRIP	TRansformation Induced Plasticity AHSS

Chapter 1

Introduction

1.1 Motivation

The family of Advanced High Strength Steels (AHSS) are increasingly being implemented into automotive body parts, where they hold the potential to reduce the vehicle weight while maintaining the strength and stiffness of the car. As well, continued pressure on automotive manufacturers for improved fuel economy increases the interest in reducing sheet metal thicknesses to the lowest possible. However, the analysis of failure in AHSS has proven difficult. For example, the parts shown in Fig. 1.1 are of nominally the same material, and even though the one on the right featured better ductility and a higher hardening exponent, it fractured while the other one did not (Schmid, 2008). Clearly, traditional analyses can not be used to assess the failure behavior of these materials for stamping and crash simulations. A newer method is needed that can better predict the fracture of AHSS sheets under stamping and crash deformation.

Meanwhile, the intermediate range of strain rates between 1/s and 100/s is important for crash studies (Zhao, 2007). It is hoped that this thesis will help the understanding of fracture in low to intermediate strain rates to improve crash analysis and design.
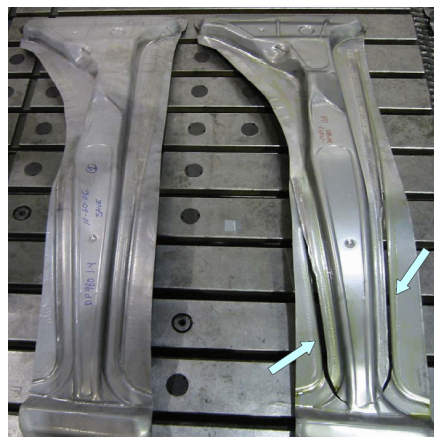
Figure 1.1: The same part stamped out of the same grade of AHSS provided by different suppliers. Traditional analysis would predict that the part on the right would perform better. (Schmid, 2008)

1.2 Research Objective and Scope of Work

The current thesis will characterize the quasi-static plastic and fracture properties of a sample AHSS. The applicability of the chosen fracture model will be shown, and the fracture model will be extrapolated into another dimension: strain rate. Strain rates in the range of quasi-static through intermediate (850/s) will be the focus of the current study. Because of the equipment available at the Impact and Crashworthiness Laboratory (ICL) at the Massachusetts Institute of Technology (MIT), the experiments will focus on application of a spring-assisted drop tower for the dynamic portion of the experiments.

The current study will focus on one particular material that is deemed representative. Dual Phase (DP) 780 was chosen as the basis for this study and represents a popular class of steels for automotive structures.

1.3 Background

1.3.1 Ductile Fracture

Researchers have traditionally seen the fracture locus of the ductility as a functional depending on the state of stress. An example of such a dependency is shown in Eq. (1.1).

$$\bar{\varepsilon}_f^p = f\left(\eta, \bar{\theta}\right) \tag{1.1}$$

where η (the stress triaxiality) and $\bar{\theta}$ (the Lode angle) are defined in Eq. (1.2) and (1.3), respectively.

$$\eta \equiv \frac{\sigma_m}{\sigma_{VM}} = \frac{\frac{1}{3}\left(\sigma_I + \sigma_{II} + \sigma_{III}\right)}{\sqrt{\frac{1}{2}\left[\left(\sigma_I - \sigma_{II}\right)^2 + \left(\sigma_{II} - \sigma_{III}\right)^2 + \left(\sigma_{III} - \sigma_I\right)^2\right]}} \tag{1.2}$$

$$\bar{\theta} \equiv 1 - \frac{3}{\pi}\cos^{-1}\left(\frac{\xi}{\sigma_{VM}}\right)^3 = 1 - \frac{2}{\pi}\cos^{-1}\left(\frac{\frac{27}{2}\left(\sigma_I - \sigma_m\right)\left(\sigma_{II} - \sigma_m\right)\left(\sigma_{III} - \sigma_m\right)}{\left[\frac{1}{2}\left[\left(\sigma_I - \sigma_{II}\right)^2 + \left(\sigma_{II} - \sigma_{III}\right)^2 + \left(\sigma_{III} - \sigma_I\right)^2\right]\right]^{3/2}}\right) \tag{1.3}$$

where σ_I, σ_{II}, and σ_{III} are principal stresses with $\sigma_I \geq \sigma_{II} \geq \sigma_{III}$, ξ is the third invariant of the stresstensor, σ_m is the mean stress $\frac{1}{3}\left(\sigma_I + \sigma_{II} + \sigma_{III}\right)$, σ_{VM} is the von Mises stress.

Physically, the stress triaxiality can be seen as the normalized pressure while the Lode parameter can be seen as the tendency of one of the principal stresses to dominate over the other two. For

example, the state of uniaxial tension corresponds to a stress triaxiality of one third and a Lode angle of unity while the state of equi-biaxial tension corresponds to a stress triaxiality of two thirds and a Lode angle of negative unity. Pure shear is zero for both stress triaxiality and Lode angle.

Ductile fracture has been studied in-depth since the 1960's. McClintock (1968) and Rice and Tracey (1969) both attempted to create novel fracture loci through the use of closed-form analytical solutions. Both teams arrived at a very similar conclusion, which formed the basis for decades of fracture theories: ductility depends strongly on the hydrostatic pressure, or stress triaxiality in normalized form, applied to the region in question. The Rice and Tracey team also noticed that their solution depends on the Lode parameter, but they found that it was a weak dependence and disregarded it. The McClintock and Rice/Tracey fracture theories were subsequently homogenized into a single theory by Hancock and Mackenzie (1976), which formed the basis for yet further development.

A parallel development was the invention of a physics-based method started by Gurson (Gurson, 1977, Needleman and Tvergaard, 1984). This method considers the initiation and growth of voids in the material as these voids affect first the plastic flow properties of the material and subsequently the softening and failure of the material. This class of fracture models requires the density of initial voids as input and is therefore more difficult to implement.

In Xue's Ph.D. thesis (2007), he showed that ductility is a function of both stress triaxiality and the Lode parameter. While the finding that fracture depends on the Lode parameter goes as far back as Rice and Tracey, Xue found that the dependence is strong enough that it needs to be accounted for in realistic simulations. His model was subsequently simplified by Bai (Bai, 2008), who made the assumption that the material follows the Mohr-Coulomb assumption for fracture, even for ductile materials. Bai's fracture locus is shown in Fig. 1.2. Both Xue's and Bai's theories were developed for and validated with bulk materials but not necessarily sheet metals.
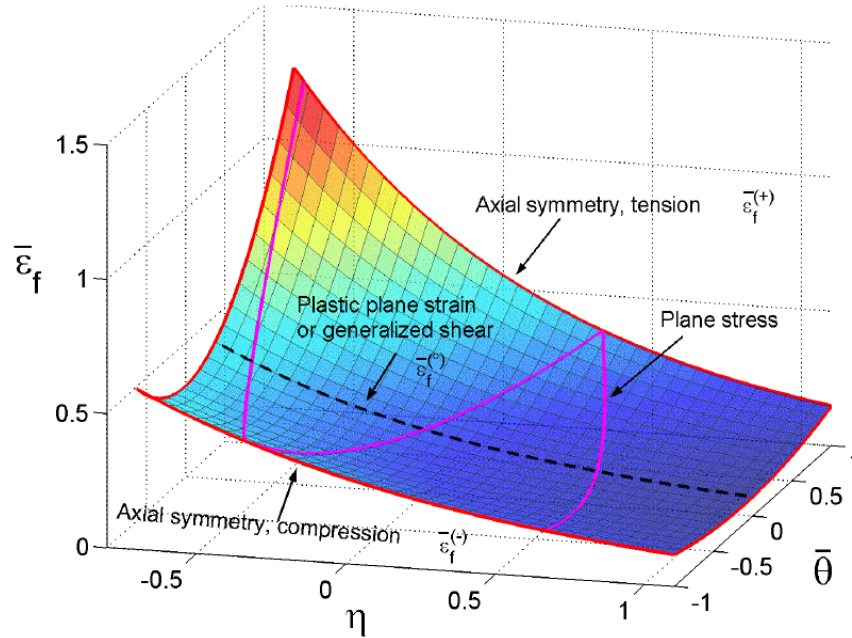
Figure 1.2: Fracture model proposed by Y. Bai, in which ductility depends on stress triaxiality (η) and the deviatoric state parameter ($\bar{\theta}$). After Bai, 2008.

1.3.2 Sheet Metal Forming

The sheet metal community has developed its own methodologies and frameworks in parallel to the academic development of fracture. Fracture in sheet metals has traditionally been assessed through the completion of a battery of Nakazima tests. The Nakazima test features a set of sheet metal strips of various widths that are clamped into a circular die and punched transversely by a hemisphere. Through this method, the specimens are deformed in membrane loading under a variety of different combinations of in-plane strain (and consequently different combinations of multi-axial stresses). Several tested Nakazima specimens are shown in Fig. 1.3. The strain is traditionally assessed post-mortem by the measurement of squares or circles that were inscribed into the material before the experiment and a composite fracture/necking envelope is represented in two dimensions on a Forming Limit Diagram (FLD), shown in Fig. 1.4. The FLD shows the locus of points of fracture or necking, expressed as the major fracture strain versus the minor fracture strain. Hasek improved upon the Nakazima test in 1978 by introducing arced cutouts into the specimen rather than using straight strips (Hasek, 1978). The cutouts allowed the experiments to achieve approximately the same combinations of in-plane strains as with the Nakazima experiments, but the curvature caused fracture to occur closer to the center and therefore closer to the desired combination of principal strains. Some post-test Hasek experiments are shown in Fig. 1.5.

23
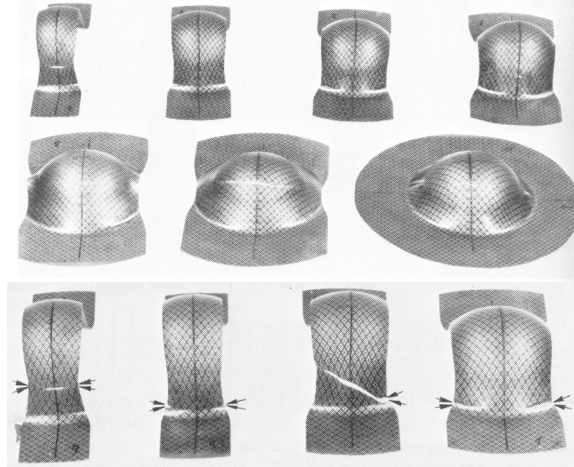
Figure 1.3: Post-test Nakazima specimens. A full battery of experiments is shown on top, and particular cases are highlighted on the bottom to show that the location of fracture is not at the center. (Hasek, 1978)
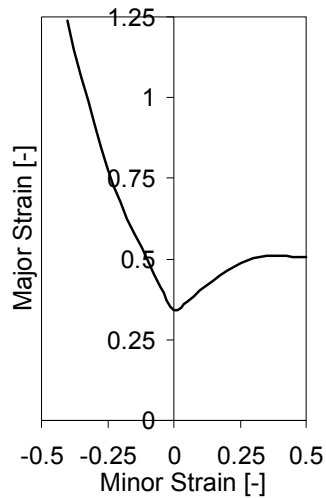
Figure 1.4: An example Fracture Forming Limit Diagram (FLD) representing the traditional 2-Dimensional approach to fracture in which the fracture envelope is interpreted as a limiting curve of the major fracture strain as compared to the minor fracture strain. After Chen and Zhou (2008).
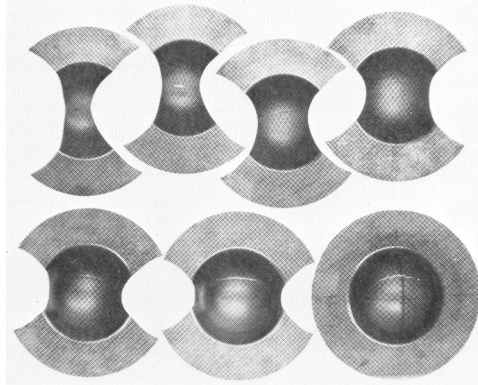
Figure 1.5: Hasek's improvement over the Nakazima experiment, in which his specimens have curved sides with different cutout radii in them so that fracture always occurs close to the center. (Hasek, 1978)

1.3.3 Intermediate Strain Rates

The effect of intermediate strain rates on plasticity and fracture has been difficult to measure because intermediate strain rates are measured at time scales smaller than traditional quasi-static methods of force/extension measurements are capable of measuring while they are measured for time durations longer than traditional Hopkinson bars are capable of. One key method of measuring material properties in this range is through the use of high-speed hydraulic equipment, e.g. Larour et. al. (2004) and Roos and Mayer (2003). However, this equipment comes with severe limitations in its ability to properly measure both displacement and force signals (Bleck and Larour, 2003). Some of these limitations can be easily seen in Fig. 1.6, which shows stress-strain curves from two different investigating teams. In both cases, the teams used high-speed hydraulic equipment to load the specimen and a combination of piezoelectric load cells and strain gages on the specimen to measure the force on the specimen. In both cases, the investigators found a large oscillatory response due to the dynamics of the fixtures superposed onto the material data.
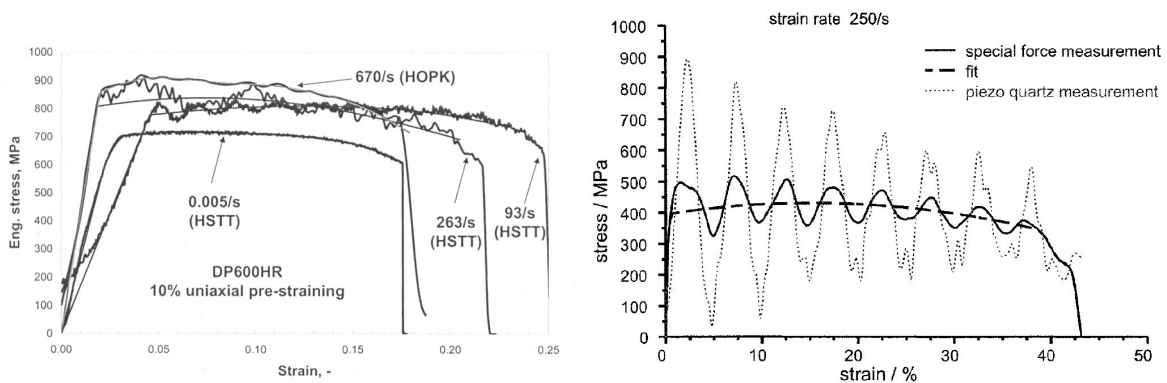
Figure 1.6: Stress vs. strain curves from two different universities as measured by high-speed hydraulic equipment showing oscillatory force signals. Left after Larour et. al. (2004). Right after Roos and Mayer (2003).

A number of researchers have attempted to quantify the effect of strain rate on fracture (for example, Johnson and Cook, 1985, Mirza et. al., 1996, Alves and Jones, 1999, Hopperstad, Borvik, et. al., 2003, and Larour et. al, 2004) with mixed results. Johnson and Cook found a dependence, which they quantified into what is probably the most popular strain-rate dependent fracture law. Johnson and Cook's fracture locus, shown in Eq. (1.4), indicates a monotonic increase of ductility with strain rate.

$$\bar{\varepsilon}_{fracture}^{p} = \left[D_1 + D_2 \exp(D_3 \eta) \right] \left[1 + D_4 \ln\left(\frac{\dot{\varepsilon}}{\dot{\varepsilon}_0} \right) \right] \left[1 + D_5 T^* \right] \qquad (1.4)$$

Mirza et. al. (1996) found that there was no dependence of ductility on strain rate for iron or aluminum alloy, but there is a dependence for mild steel under certain states of stress, in which the failure mode transfers from ductile to brittle. However, it is difficult to see the impact of this transition on the ductility from the fracture strain data that the authors present. Alves and Jones (1999) found that there was no dependence of ductility on strain rate for mild steel.

Larour et. al. (2004) reported the effect of strain rate on fracture for DP600LN, and some of their results are shown in Fig. 1.7. This data is hindered by the aforementioned limitations of high-speed hydraulic testing equipment, and this data only represents one state of stress: uni-axial tension. It is impossible to determine how the shape of the fracture locus like that shown in Fig. 1.2 changes with only one state of stress. Also, there is a large scatter on the last data point on the curve, which was measured with both Hopkinson bar and high-speed hydraulic test frame. The large difference between the same data measured with a high-speed hydraulic frame and Hopkison bar opens all of the data up to interpretation. However, the data in Fig. 1.7 shows that there is a dependence of strain rate on ductility.
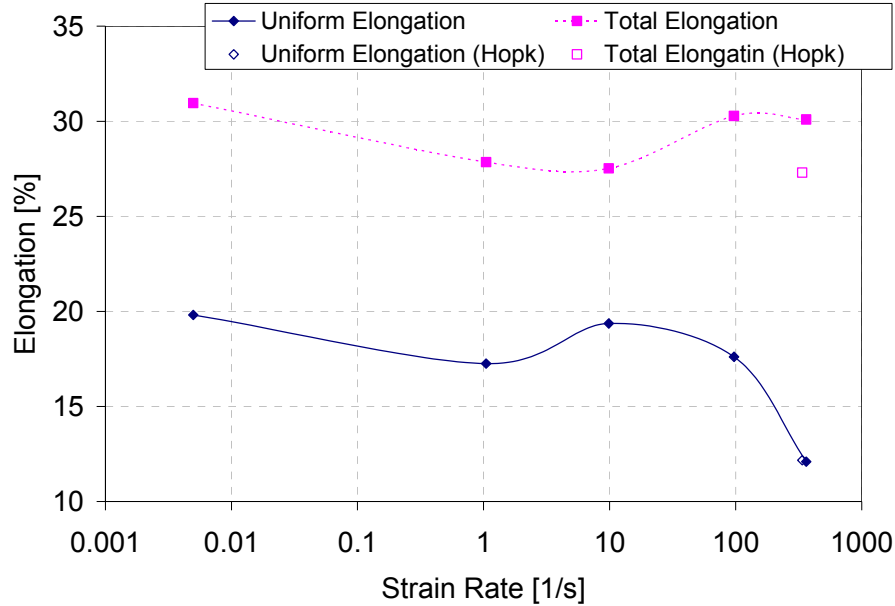
Figure 1.7: Ductility data for DP600HR as measured by Larour et. al. (2004) in uniaxial tension. Closed points represent measurements with a high-speed hydraulic frame, and open points (only at the highest strain rates) represent measurements made with a split Hopkinson bar.

Hopperstad, Borvik, et. al. (2003) attempted to determine the effect of both stress triaxiality and strain rate on Weldox 460 E structural steel. Some of their findings are shown in Fig. 1.8. A key feature is that there appears to be a very large dependence of ductility on strain rate for the uniaxial state of stress but not for other states of stress. The authors indicate that they do not know why this may happen. This data emphsizes the weakness of the work by Laurour et. al, in which only one state of stress is tested.

With the exception of Larour et. al., all of the above-mentioned teams did their fracture work on bulk materials and adjusted stress triaxiality by notches in axisymmetric specimens. Larour et. al. made no attempt to adjust stress triaxiality, but instead relied on uni-axial specimens.

The combination of the data from Larour et. al. and Hopperstad, Borvik, et. al. shows a far more complex dependence of ductility on strain rate than would be expected from Johnson and Cook's analysis. As well, there is nothing currently in the literature that accounts for the joint dependence of ductility on stress triaxiality, Lode parameter, and strain rate.
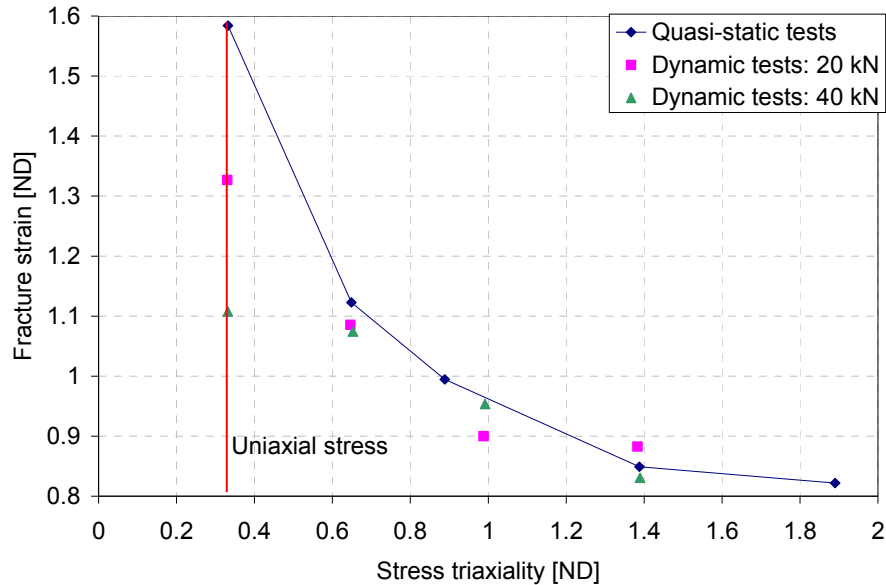
Figure 1.8: Ductility data measured by Hopperstad, Borvik, et. al (2003) for Weldox 460 E. The dynamic preloads (20 kN and 40 kN) correspond to increasing strain rate. It was observed by the experimenters that the ductility for the pure uniaxial stress state appeared to have a large dependence on strain rate while other cases were very insensitive to it.

Therefore, a method is being proposed in which a drop tower spans and augments the data between fast hydraulic systems equipped with traditional force/displacement measurement equipment on the low end and much faster Hopkinson bar data on the high end. This research will also aim to calibrate a fracture locus for multiple strain rates and determine the evolution of the shape and amplitude of said fracture locus with strain rate.

1.4 Research Strategy

The research is divided into several tasks which build upon one another. The chronology and interdependence of the techniques will be outlined here, and then each technique will be developed in further detail in subsequent sections. Some key themes are present in multiple chapters, so some key definitions and formulas are repeated where appropriate.

Each step is necessary for the one immediately after it. The ultimate goal of the research is to better understand the effect of strain rate on ductile fracture, with application to sheet steel. In order to do this, a method will be needed that can test the steel to fracture over a wide range of strain rates and stress states. The Hasek test done in a drop tower was chosen for this. However, the drop tower is not applicable below a certain testing velocity, so a series of tests in an electromechnaical load frame will be used in addition to the drop tower to span a larger range of strain rates. The Hasek tests have yet to be demonstrated in conjunction with the current state-of-the-art fracture methodology, the Mohr-Coulomb fracture locus, which was developed using butterfly fracture specimens. Therefore, butterfly fracture tests, which have been successfully use to calibrate the Mohr-Coulomb fracture locus, will be completed (See the section "Butterfly Fracture Tests"). Use of the butterfly fracture tests relies on a precise knowledge of the plastic

properties of the material. Therefore, there will first be a detailed characterization of the material under quasi-static and dynamic loading (see the sections for quasi-static and dynamic characterization of plasticity). This procedure is outlined chronologically in Fig. 1.9.
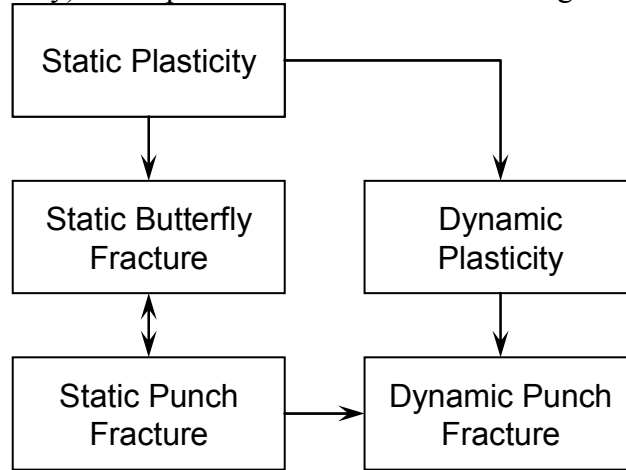
Figure 1.9: Plan of research showing interdependence of various steps.

1.4.1: Quasi-static Plasticity

The methodology, experiments, and results for the quasi-static plasticity section is given in Chapter 2 and very briefly summarized here. They key contribution of this section of the thesis is to provide very detailed isotropic plasticity data for use by analytical tools or by the finite element method to better understand all of the other experiments.

In the first part, plasticity data was determined through the tensile testing of dogbone specimens that were cut in different orientations with respect to the rolling direction of the sheet. From this data, the Lankford parameter was calculated for three tensile directions, and the plate was determined to be in-plane isotropic.

The plasticity of the material was further developed through a series of experiments developed by Mohr and Oswald (2007). In the approach of Mohr and Oswald (2007), a very short but wide specimen is subjected to a number of different combinations of shear and tension. This specimen was designed by finding a geometry in which the stress and strain fields are sufficiently homogenous that they can be determined by closed form equations from force and displacement measurements. Jacquemin (2007) subsequently extended this methodology to characterize for anisotropy by taking specimens from multiple orientations relative to the parent sheet.

The current research uses the original Mohr-Oswald geometry tested in two directions (rolling and cross-rolling) relative to the parent sheet. Five different combinations of shear and tension are tested for each orientation, ranging from pure tension to pure shear, with three combined tension/shear cases. Additionally, this thesis proposes a specimen design similar to Mohr and Oswalds (2007) geometry without a reduced thickness. Because of the requirement that the area is reduced from the grip sections to the gage section so that frictional forces in the grips can balance the stress in the gage section, the full-thickness specimen has a less wide gage section. The development and assessment of the full-thickness specimen is also presented in Chapter 2.

1.4.2: Quasi-static Fracture Tests (Butterfly Specimen)

The methodology, specimen, and results relating to the butterfly specimen are given in detail in Chapter 3. This section of the thesis is intended to provide a baseline fracture locus against which the punch style methods can be assessed. The key features of this procedure will be summarized here.

After the material was characterized for plasticity, it was characterized for fracture in quasi-static strain rates according to the butterfly procedure developed by Bai (2008). Bai's (2008) method was chosen because it has previously been well validated and had the unique feature that it was able to achieve a very large range of different stress triaxialities with the same specimen. It also initiates fracture in the center of the gage section (as opposed to free surfaces), minimizing the effects of manufacturing on the ductility of the specimen. Bai's (2008) method focused on the application of various types of loading to a butterfly-shaped specimen that features a lofted cutout at the center, see Fig. 1.10.
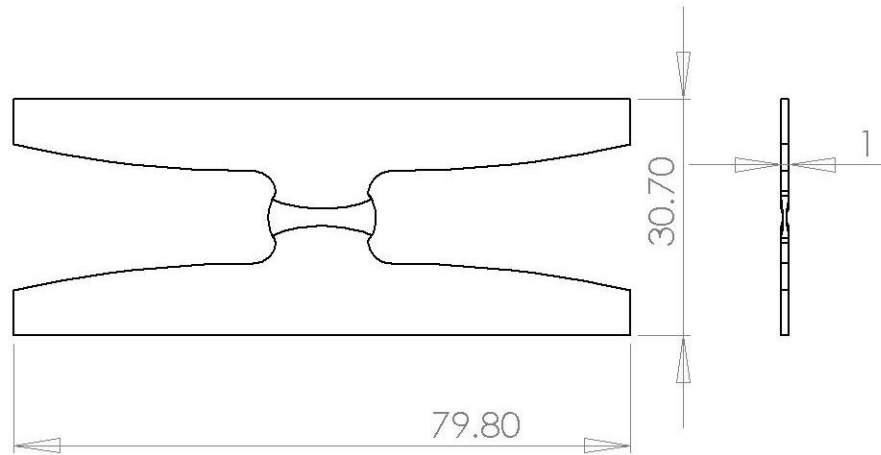
Figure 1.10: Butterfly fracture specimen with double-curvature geometry that produces fracture in the center and is resistant to edge effects. After Bai (2008).

Unfortunately, the butterfly specimen is not readily applicable to dynamic loading. This was found by simulating the butterfly geometry in an idealized drop tower test. The top of the butterfly specimen was constrained not to move, while the bottom was assigned a large mass and an initial downward velocity, see Fig. 1.11. The force on the top and bottom of the specimen were recorded, and they are shown as a time history in Fig. 1.12. As can be seen in the force data, the specimen never achieves equilibrium between the top and bottom. This is due to the complex geometry in the center, which serves to diffract the stress waves passing through the specimen. The fact that the specimen never achieves equilibrium and the very transient nature of the force time history imply that it will be nearly impossible to convert force data from this specimen into stress data when the specimen is loaded dynamically. This realization helped to motivate a desire for a different type of test that could span a large range of stress states but is less susceptible to dynamic effects.
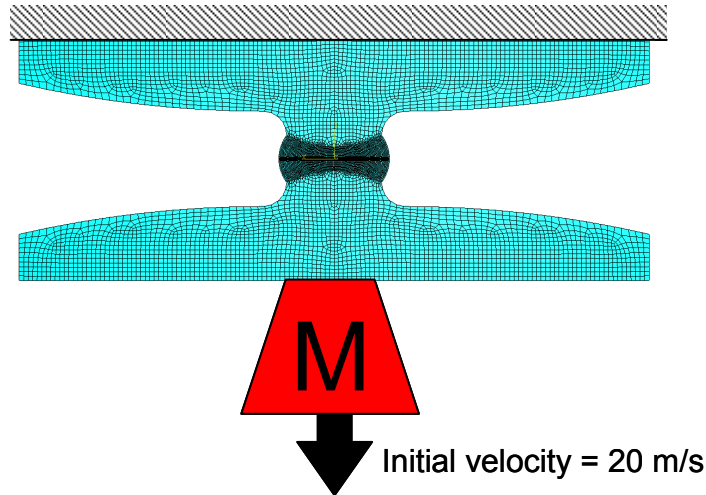
Figure 1.11: Finite element model used to evaluate the butterfly specimen geometry for application to dynamic testing
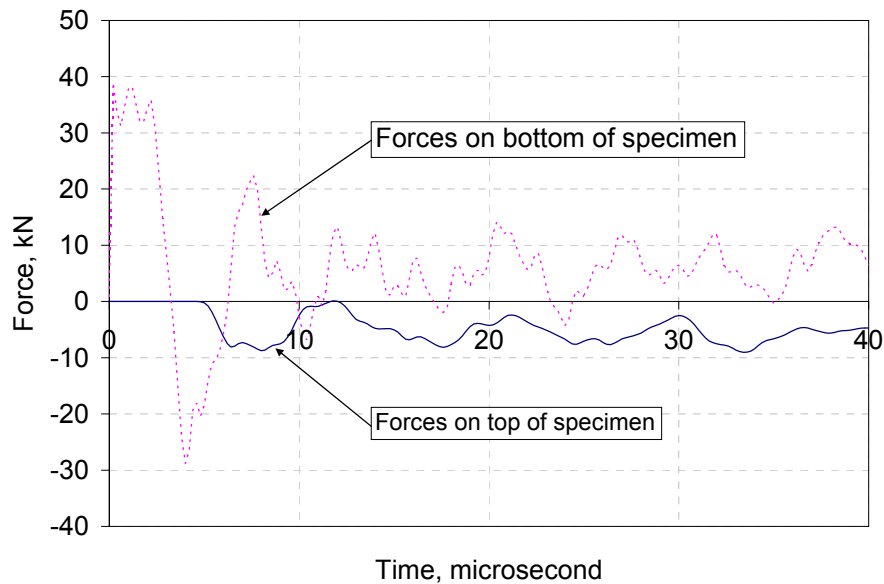
Figure 1.12: Time history of forces recorded on the butterfly specimen when the top was fixed and the bottom was given a mass and initial velocity. This shows that the specimen is not in equilibrium.

1.4.3: Quasi-static Fracture Tests (Punch experiments)

A more full description of the Hasek experiments and their results is presented in Chapter 3. This section of the thesis will provide a bridge from the butterfly specimens to the dynamic experiments. Because it is quasi-static, it can be readily compared to the butterfly experiments. The favorable dynamics of the experiment allow it to be extend into the dynamic range.

The Hasek Test is a method of testing for fracture by laterally indenting a circular plate by a hemispherical punch. The state of stress in the specimen can be adjusted from almost uniaxial to

equi-biaxial by introducing cutouts in the plate. This test has the advantage that it is much better suited than the butterfly experiments to dynamic loading. Unfortunately, the Hasek test has a key limitation that the state of stress can not be directly measured. For this purpose, force and punch depth were recorded, and correlated with a finite element model of the test case. The state of stress, strain, and strain rate for every point in the test will thus be taken from the finite element model. Alternatively, the state of stress expressed as stress triaxiality can be inferred directly from the state of strain and only a single parameter from the plasticity model. This method is presented in Chapter 3. It is also compared against the butterfly experiment in the same chapter.

1.4.4: Dynamic Plasticity Tests

The work done on validating the dynamic plasticity model is presented in Chapter 4. This section is intended to evaluate a plasticity model so that the dynamic experiments can be interpreted through the use of FEA.

Just as interpretation of the quasi-static Hasek test requires a good plasticity model, interpretation of the dynamic Hasek test requires a good strain-rate dependent plasticity model. Most of the work on strain rate dependent plasticity in the literature has been done with either a split Hopkinson bar or with a high-speed hydraulic apparatus. See, for example, Van Slycken et. al. (2007), Zhao and Gary (1996), Johnson and Cook (1985), Nemat-Nasser et. al. (1999), Rusinek et. al (2003), Roos and Mayer (2003) and Larour et. al. (2004). However, the current work concentrates on the intermediate range of strain rates done in a drop tower.

There is a large number of strain-rate dependent plasticity models available in the open literature (e.g. Cowper and Symonds (1958), Zhao (1997), Bronkhorst et. al. (2006), Johnson and Cook (1985), Cheng et. al. (2001), Fallansbee and Kocks (1988), and Rusinek et. al. (2007)). These plasticity models have varying levels of complexity. The simplest approaches are one like that of Johnson and Cook (1985) or Bodner and Symonds (1978), who propose that the strain rate can be accounted for as a multiplier of the hardening curve, Eq. (1.5).

$$\bar{\sigma} = \sigma^0\left(\bar{\varepsilon}^p\right) R\left(\dot{\bar{\varepsilon}}^p\right)$$ (1.5)

Many papers by Symonds (e.g. Cowper and Symonds (1958), Symonds and Chon (1974), and Bodner and Symonds (1978)) present a power law relationship for the factor $R\left(\dot{\bar{\varepsilon}}^p\right)$, which is shown in Eq. (1.6).

$$R\left(\dot{\bar{\varepsilon}}^p\right) \equiv \frac{\bar{\sigma}}{\sigma^0} = 1 + \left(\frac{\dot{\varepsilon}}{\dot{\varepsilon}_0}\right)^{1/n_{CS}}$$ (1.6)

This form has become commonly referred to as the Cowper-Symonds law. Within Chapter 4, the Cowper-Symonds law will be fit to test data for Dual Phase steel, and a parametric study will be done to assess the impact of different levels of strain rate sensitivity on the correlation of test

with simulation. Finally, the strain rate of the experiments will be assessed as temporal and spatial distributions, then averages, and the importance of the value of $R\left(\dot{\bar{\varepsilon}}^{\,p}\right)$ is discussed.

1.4.5: Dynamic Punch Fracture Tests

The dynamic punch experiments are discussed in detail in Chapter 5. That chapter capitalizes on all of the prior work (plasticity, quasi-static fracture experiments) to establish a new method for determining the fracture of sheet steels under intermediate strain rates. Further, this chapter presents the data obtained for a sample material (DP780) and interprets it in the context of the three-dimensional fracture locus.

The fracture punch tests in Chapter 3 were done in a relatively slow but high-capacity screw-driven loading frame. After the punch fracture tests were validated against butterfly fracture tests in quasi-static loading, the punch fracture test procedure was extended to various strain rates by doing the tests in a drop tower. The available drop tower is capable of speeds up to 15.5 m/s or masses up to 80 kg. It is shown in Fig. 1.13. The strain rate can be adjusted over a wide range (theoretically greater than 2000/s, with a small enough punch and die) by changing the initial velocity, drop mass, punch diameter, and specimen diameter.

Figure 1.13: Drop tower available at the Impact and Crashworthiness Laboratory at MIT. This drop tower is capable of speeds up to 15.5 m/s or masses up to 80 kg.

Simonsen (2000) created an analytical solution for a circular plate subjected to lateral punch by a hemispherical punch. His solution allowed for the calculation of a reaction force given a punch depth and the maximum strain in the plate. Based on this, a MATLAB routine was created that numerically solves the dynamic equations of motion as the drop mass impacts the plate. The strain rates can be found by numerically differentiating the strain data with respect to time. This software was run iteratively to find the range of strain rates for various drop masses, velocities,

die diameters, and punch diameters. Examples of the findings are shown in Fig. 1.14, which shows the extremely high strain rates that can be accomplished with the maximum drop velocity, the smallest punch, and the smallest die.
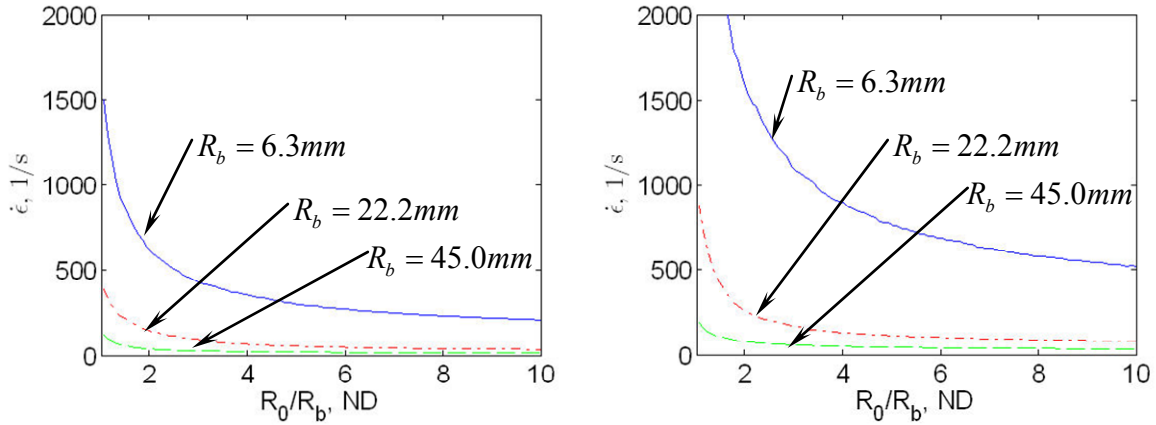
Figure 1.14: Strain rates that the drop tower is capable of achieving for punching a circular plate with various punch radii (R_b) and die radii (R_0). The plot on the left corresponds to the maximum drop mass with the corresponding maximum drop velocity. The plot on the right corresponds to the maximum drop velocity with the corresponding drop mass.

1.5 Conclusions

A gap exists in the literature in which little research is being done on the effect of stress triaxiality, Lode parameter, and strain rate on ductility. A procedure for filling this gap has been outlined in this introductory chapter and will be developed in greater detail throughout the remaining chapters of this thesis.

Chapter 2

Characterization of Plasticity

2.1 Abstract

Tests were performed on three types of biaxial plasticity sheet steel specimens: full-thickness with an optimized 2-D profile, symmetrically reduced thickness with a nearly rectangular gage area, and reduced thickness with nearly rectangular gage area in which thickness was reduced only from one side. While the shape of the specimens with a nearly rectangular area had previously been optimized by Mohr and Oswald (2008), the full-thickness specimen was optimized and first presented here. The 2-D geometry of the full-thickness has been iteratively optimized through testing and analysis, and further iterations are believed to give only minimal improvements with the currently available hardware. Simulation of the full-thickness specimen and comparison of the full-thickness specimen against the symmetrical reduced thickness specimens shows that the full-thickness specimen can not accurately be used with traditional analysis to determine plasticity parameters of sheet steels. However, the width of this specimen was limited by machine force capacity, and a higher-capacity machine would allow a larger width and consequently closer approximation to the assumptions of traditional closed-form analysis. If the full-thickness specimen is used, then it must be used with iterative simulation of a multi-element, geometrically accurate finite element model for calibration of plasticity. Alternatively, simulation of tests on the full-thickness specimen will serve as a validation tool for an existing characterization for in-plane plasticity of a sheet steel. Using the above methods plus traditional dog bone specimens, the plasticity parameters of an Advanced High Strength Steel (AHSS) sheet metal DP780 was calibrated with the symmetrically reduced thickness specimen, and then compared with full-thickness specimens. It was found that the steel could be adequately characterized for in-plane properties with both von Mises and Hill 48 models, but only the Hill 48 was able to capture the reduction in thickness due to tensile strain.

2.2 Introduction

An experimental technique for biaxial testing of Advanced High Strength Steel sheets was previously demonstrated by Mohr and Oswald (2008). In this technique, a short and wide specimen with a reduced gage thickness is subjected to different combinations of tension and shear. However, through the process of rolling, steel sheets can produce through-thickness textural inhomogeneity and thus differences in mechanical properties through the thickness of steel sheets (Park, Park, and Chin, 2002). Therefore, creation of a specimen that does not require thickness reduction holds the potential to increase the fidelity of testing by accounting for the mechanical properties of the full thickness of the material.

Wide availability of computer-controlled abrasive jet machines as well as availability of computer-controlled wire Electrical Discharge Machining (EDM) makes the production of two-dimensional shapes in arbitrarily hard steels quite easy. Removal of material from the thickness requires either the use of a second technique, like Sinker EDM or conventional milling. Electrical Discharge Machining operates through the melting of material, so this process typically features layers of melted and re-cast layers and a heat-affected zone where the mechanical properties have been changed (Bleys et. al., 2006). When the machined surface is the two-dimensional profile of a sheet metal specimen (as in the case of a wire EDM), this effect is insignificant, as it is a tiny fraction of the width of the material. However, when the material removal is in the thickness direction, then the heat-affected area can be a more significant fraction of the remaining thickness. As well, the sinker EDM typically results in a larger heat affected zone than a wire EDM (Bleys et. al., 2006). Conventional machining has its own limitations, especially in Advanced High-Strength Steels, which can have a relatively high specific energy to fracture, which correlates to temperature rise due to machining. Conventional machining of steels can produce work hardening of the machined surface, residual stresses, and heating of the machined surface (Outeiro et. al., 2006). Moreover, Outeiro et. al. (2006) show that the residual stresses associated with machining can penetrate to a depth of 0.1 mm for a first-pass cut and more for a multi-pass cut. With the symmetrical removal of material and 0.5 mm thickness of the Mohr and Oswald (2008) specimen, the residual stresses could account for 40% of the thickness. The additional process of either sinker EDM or conventional machining would require additional equipment and skills, and it could add significant lead time and expense to a testing program. A two-dimensional specimen that does not rely on the removal of material in the thickness direction will be sought to avoid loss of information about through-thickness inhomogeneity and reduce machining affects on the specimen surface, additional cost, and additional lead-time. .

The work described in this paper aims to characterize the plasticity of a sample sheet steel (Dual-Phase DP780 provided by US Steel) with both the well-established technique featuring a reduced-thickness gage section and a new method that has not reduction in thickness. The effects of through-thickness inhomogeneity will also be assessed by comparing specimens in which the thickness was reduced symmetrically from both faces of the material against specimens in which the thickness was reduced by removing exactly half of the thickness from one side, thus preserving one of the original surfaces of the material in the gage section. First, standard uniaxial tension tests are performed to estimate material hardening curves and anisotropic parameters.

Traditional flat dog-bone specimens have a reduced width but not thickness. The present technique aims at extending the applicability of full thickness specimens into biaxial testing.

2.3 Uniaxial Tension Experimental Technique

Six standard uniaxial tension tests conforming to ASTM E 8M were performed. Dogbone samples were extracted from sheets at 0, 45, and 90 degrees with respect to the rolling direction; two specimens were taken for each direction. The specimens were removed by an Omax abrasive jet machine. All specimens were tested to fracture on an MTS 200 kN electromechanical load frame equipped with a 200 kN load cell and wedge grips.

Displacements are measured through VIC-2D, which is a Digital Image Correlation (DIC) package made by Correlated Solutions, Inc (West Columbia, SC). With this method, the specimen is painted white and then sprayed with a black speckle pattern. The VIC-2D software is able to track the displacement of arbitrary positions in each of the pictures by comparing the deformed image to the original. A DIC subset of 29 was used for all experiments. Using the DIC method, the vertical displacement of two points on the horizontal centerline of the specimen was measured as well as the lateral displacement of two points on the vertical centerline.

Forces measured by the load cell and displacements measured by DIC were converted into true stress and true strain. The true stress versus true strain data are presented in Fig. 2.1.
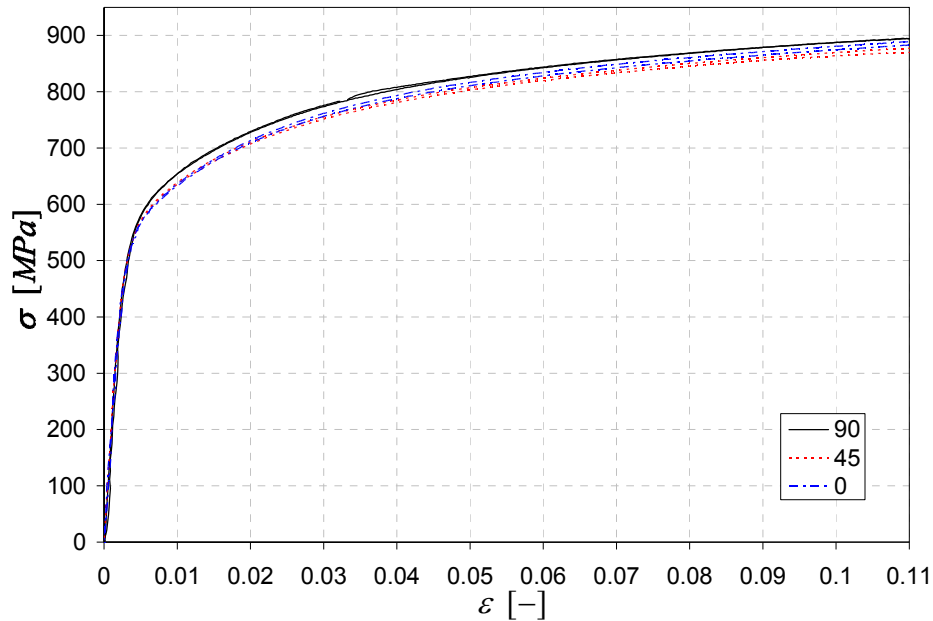
Figure 2.1: True stress versus true strain test data for DP780 for specimens cut 0, 45, and 90 degrees with respect to the rolling direction of the sheet material.

2.4 Determination of Anisotropy

The uniaxial tests were used to determine the anisotropy of the material by the determination of the Lankford parameter, defined in Eq. (2.1).

$$r_\alpha \equiv \frac{d\varepsilon_w^p}{d\varepsilon_t^p} \tag{2.1}$$

where $d\varepsilon_w^p$ is the width plastic strain under uniaxial tension, $d\varepsilon_t^p$ is the thickness plastic strain under uniaxial tension, and the subscript α indicates the angle with respect to the rolling direction. To find the Lankford parameter, the thickness strain must first be determined. This value was found by measuring the in-plane axial and width strains and applying the assumption of plastic incompressibility. The Lankford parameter itself was found by taking a least-squares-

37

fit slope between the width plastic strain and the thickness plastic strain in a region where the relationships were very close to linear. The relationships were linear throughout most of the experiment; elimination of the nonlinear parts only precluded the use of the data immediately following yield and after necking. Lankford's parameter as a function of tensile direction relative to the rolling direction is shown in Fig. 2.2. The fact that the Lankford parameter is not unity and not equal for all directions implies that the material is anisotropic.

If a Hill '48 anisotropic model is assumed, then the Lankford parameters can be quickly converted into Hill parameters using the associated flow rule. Hill's equivalent stress is shown in Eq. (2).

$$\bar{\sigma}_{Hill} = \sqrt{F(\sigma_{22} - \sigma_{33})^2 + G(\sigma_{33} - \sigma_{11})^2 + H(\sigma_{11} - \sigma_{22})^2 + 2L\sigma_{23}^2 + 2M\sigma_{13}^2 + 2N\sigma_{12}^2} \qquad (2.2)$$

where F, G, H, L, M, and N are material constants. The fact that $r_0 = r_{90}$ implies transverse anisotropy, meaning that the in-plane behavior of the material is mostly isotropic and that anisotropy comes primarily from its out-of-plane behavior. This observation implies that we can find the normal anisotropy parameters through Eq. (3), which gives the Hill parameters $F=G=0.436$ and $H=0.564$.

$$F = G = 1 - H = \frac{1}{2}\sqrt{\frac{2}{r_0 + 1}} \qquad (2.3)$$
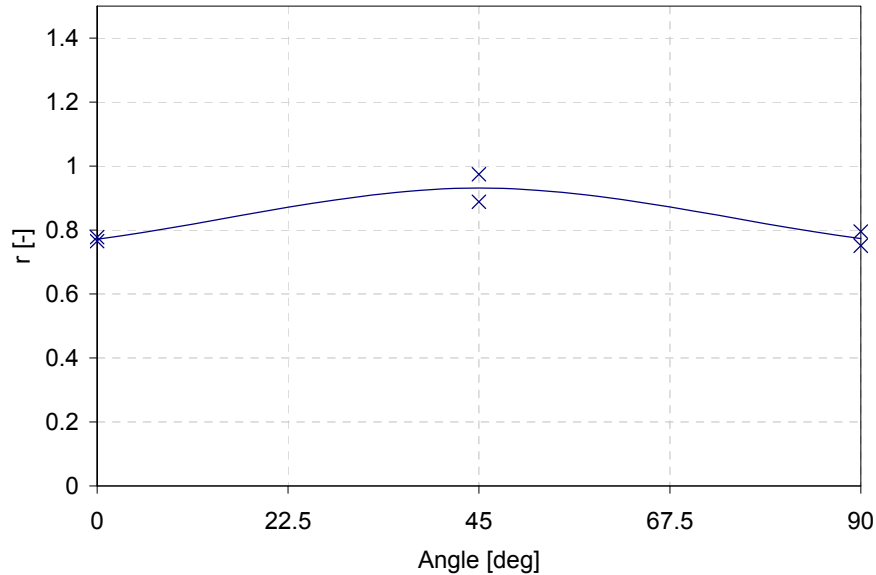
Figure 2.2: Lankford parameter as a function of angle with respect to the rolling direction of the material. Note that the Lankford parameter is identical for the 0 and 90 degree conditions, but it is not unity for any conditions.

2.5 Biaxial Experimental Technique

The experimental technique was treated in detail in Mohr and Oswald (2008), but it will be summarized here. The experimental technique for the full-thickness specimen is identical to that of the reduced-section specimen with the exception of the geometry and specimen preparation.

2.5.1 Specimen preparation

Three different types of specimens were prepared for the current series of experiments. One of the types is the same as that proposed by Mohr and Oswald (2008). In this geometry, the gage section is ten times wider than the gage height, and the gage section is approximately rectangular, see Fig. 2.3. Wider and thicker grips are supplied to achieve the necessary ratio of friction in gripping to sectional force in the gage section. Small geometric features are introduced in the corners of the rectangle, where the gage section joins to the grip section, to abate premature fracture due to tension in the corners. This geometry was optimized to eliminate shear buckling in shear loading conditions, premature fracture in the corners, and stress and strain field inhomogeneities due to geometry.

The second specimen geometry under consideration is a specimen that is a purely two-dimensional cutout from sheet metal. This geometry has a wide gage section, but somewhat less wide than the Mohr and Oswald specimen due to limitations in the maximum force of the available test frame. Also, the lack of reduction in thickness has necessitated a more dramatic width reduction from grip section to gage section in order for the friction in gripping to balance the forces due to stresses on the gage section of the material. A deeper gripping area increases the total frictional force acting on the gripping area. A more developed transition section from the gripping section into the gage section is used to distribute the stresses into the gage section as uniformly as possible while still allowing for a large area reduction. This geometry has also been iteratively optimized through simulation and experiment to address all of the potential problems mentioned for the aforementioned geometry. Both the Mohr and Oswald (2008) and the full-thickness specimen are shown in Fig. 2.3.

A third type of specimen, which is a close relative to the Mohr and Oswald (2008) specimen is shown in Fig. 2.4. In this geometry, the thickness of the gage section is reduced by removing material only from one face. This results in an asymmetrical specimen that preserves one of the faces and eliminates the centerline of the material. Comparison of the results from this type of specimen to those of the original Mohr and Oswald (2008) specimen is anticipated to show the importance of through-thickness inhomogeneity.

Specimens were extracted parallel to and perpendicular to the rolling direction of the steel sheets for both the symmetrical and asymmetrical versions of the Mohr and Oswald (2008) geometry. For the full-thickness geometry, specimens were only extracted with the tensile axis parallel to the rolling direction.

All specimens were cut from the same sheet of DP780 steel, provided by the United States Steel Corporation headquartered in Pittsburgh, PA. For the reduced-thickness specimens, the thickness in the gage section was subsequently reduced by a conventional end mill. Before each

test, all specimens were inspected, measured, and cleaned with acetone. Additionally, all specimens were prepared for strain measurement by Digital Image Correlation (DIC) by being painted white and then being speckled with black spray paint in the gage sections. Grip sections were masked to prevent paint from interfering with the gripping of the specimens.
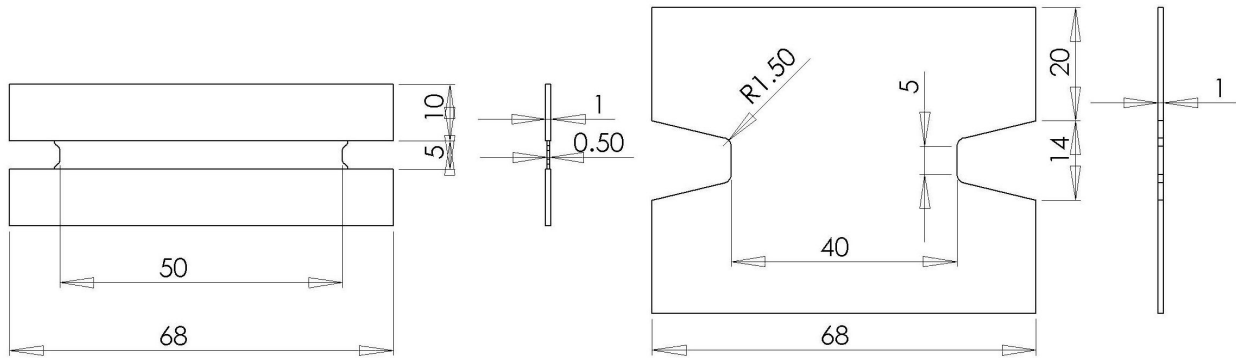
Figure 2.3: The Mohr and Oswald (2008) specimen (left) with a reduced gage section and the new full-thickness specimen (right).
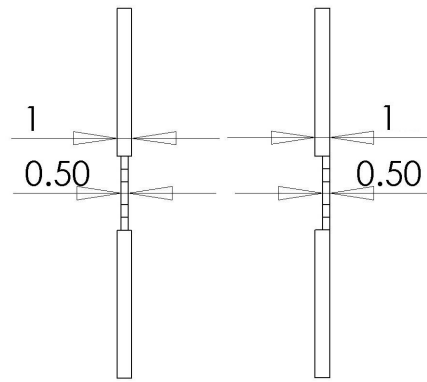
Figure 2.4: Profile drawings of two versions of the reduced-thickness specimen geometry are shown. In the original geometry (left), the thickness was reduced by removing material from both faces, resulting in a symmetrical configuration. In the altered version (right), material was removed from only one face to achieve the same final thickness.

2.5.2 Tension/Shear apparatus

A custom-made loading frame that can apply arbitrary combinations of tension and shear forces was employed for these experiments. The device, shown in Fig. 2.5, is designed with two independent hydraulic actuators. One of the actuators is arranged vertically and is used to apply tension and compression. The other one is arranged to apply horizontal forces to specimens so that it can apply shear forces to the specimen. Two load cells are arranged vertically to measure vertical forces or moments about an axis perpendicular to the two actuators. A third load cell is arranged horizontally to measure the shear forces.
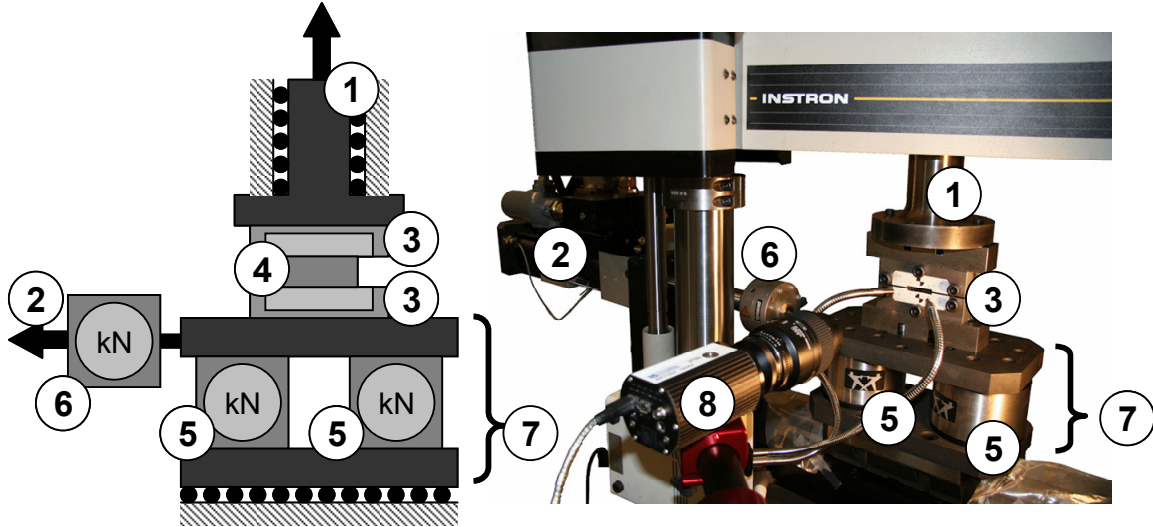
Figure 2.5: The Tension/Shear biaxial testing machine, as shown in schematic form (left) and in hardware (right). The major components are vertical actuator (1), horizontal actuator (2), grips (3), specimen (4), dual vertical load cells (5), horizontal load cell (6), sliding table assembly (7), and camera for displacement measurement by Digital Image Correlation (DIC) (8).

2.5.3 Loading conditions

In analogy to classical Arcan experiments, the loading angle is defined as a function of the ratio between tensile force and shear force; see Eq. (2.4). In this coordinate system, a 0-degree angle represents the pure shear condition while the 90-degree angle represents the pure tension condition.

$$\beta \equiv \tan^{-1} \frac{F_V}{F_H} \tag{2.4}$$

Because the cross-sectional area for all of the specimens for a given geometry was approximately the same, a so-called von Mises force is defined by Eq. (2.5).

$$F_{VM} \equiv \sqrt{F_V^2 + 3F_H^2} \tag{2.5}$$

All specimens were loaded with a constant β and the von Mises force increasing at a rate of 4.3 kN/min. This caused the specimens to yield and neck at approximately the same time and resulted in each experiment having approximately 240 data points before necking.

2.5.4 Measurement

As with the uniaxial tension specimens, displacements are measured through the VIC-2D software. Approximately 300 digital pictures of the specimen are taken as it is deforming. A DIC subset of 29 was used for all experiments. Two points, which are centered horizontally on the specimen and vertically equidistant from the center of the specimen were measured for all experiments. In the reduced-thickness specimens, the two points were 2 mm apart, and the

points were 5 mm apart for the full-thickness experiments. The points are represented for a typical full-thickness specimen in Fig. 2.6.

Horizontal forces were measured with the horizontal load cell. Frictional forces due to the design of the sliding table had previously been measured and found to be negligible (Mohr and Oswald, 2008). Vertical forces were measured as the sum of the two vertical load cells.
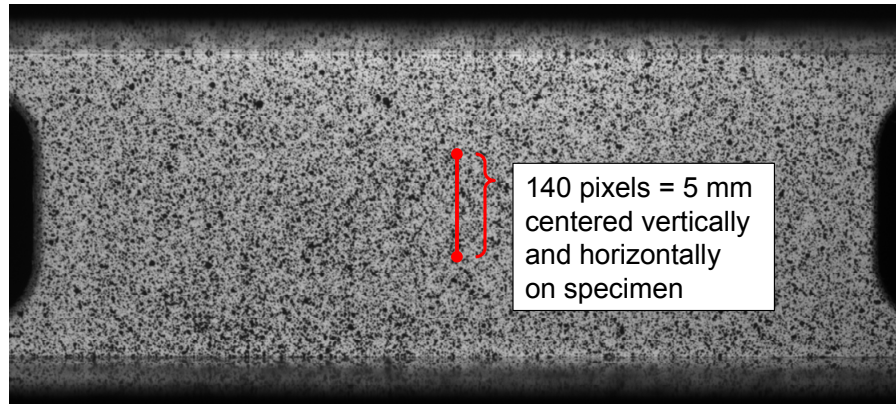
Figure 2.6: Typical picture taken for DIC purposes of the full-thickness specimen showing the two points used for strain measurement. The distance between the two points is as close to 5 mm apart as possible while still being an integer number of pixels. The points are centered horizontally, and they are equidistant from the vertical center.

2.6 Determination of Stress and Strains for Biaxial Cases

The principles of measuring stress and strain for both the full-thickness and the reduced-thickness materials are the same. As the procedure for the reduced-thickness specimen is already described in-depth in Mohr and Oswald (2008), only the full-thickness will be developed here.

The only means for direct measurement of stress is division of the vertical and horizontal forces by the cross-sectional area of the specimen. This assumption implies that the stress is approximately constant across the cross-section of the area. However, it is necessary for the stresses to be zero at the free boundary, and it is therefore known that the stresses are not uniform throughout the cross section. McClintock and Zhang (1993) observed such a boundary zone when studying fracture of thin metal strips. Therefore, a study of the stress distribution with finite elements was undertaken to determine and optimize the applicability of the assumption of constant stress and strain fields. In this study, a finite element model of the full-thickness specimen with shell elements whose typical edge length is 0.5 mm was subjected to similar tension and shear combinations as the experiments.

In this evaluation of the full-thickness specimen, two key ways of viewing the stress are important: global stress measured through parameters that can be measured in an experiment, and local stresses that represent the true stresses acting on the center of the specimen. The global stresses are determined by extracting from the finite element simulation only parameters that can be extracted for an experiment, e.g. vertical or horizontal force, and operating on them with traditional expressions. For example, the tensile true stress was found by dividing the force by

the initial area and multiplying by one plus the tensile engineering stress. Local stresses are merely the stress extracted from the center element. In an ideal experiment, the stresses would be constant across the width, and the stress on the central element would be the same as the average stress, and that would be the same as the stress determined from traditional methods.

A finite element model for the $\beta=45^0$ condition is shown in Fig. 2.7, displaying the constancy of the stress distribution. The profile of normal and shear stresses acting on all of the elements across the width for a vertically centered row of elements is shown in Fig. 2.8 for two different force magnitudes. In Fig. 2.8, the Cauchy stresses reported by each of the elements across the width have been normalized by the average true stress that was calculated as if it were an experiment. The coordinate in the width direction is normalized by the width. Both Figures 2.7 and 2.8 show a region at the periphery of the width in which the stresses are very different from the average stress across the width. Iteration on the design has shown that these areas of large stress variation are approximately the same length in millimeters regardless of the width, so widening the specimen will continue to deliver better results. However, the chosen geometry requires forces that are very close to the capacity of the available machine. Regardless of the width limitations, it can be seen from Fig. 2.8 that for $\beta=45^0$ at the magnitudes of force shown, the stress distribution across the width of the specimen is very close to the ideal condition in which the stress is constant across the width and equal to the force that would be calculated from global parameters. However, it can also be seen from Fig. 2.8 that the stress distribution evolves with applied force, so the errors of the specimen are not anticipated to be constant over the entire stress versus strain curve.
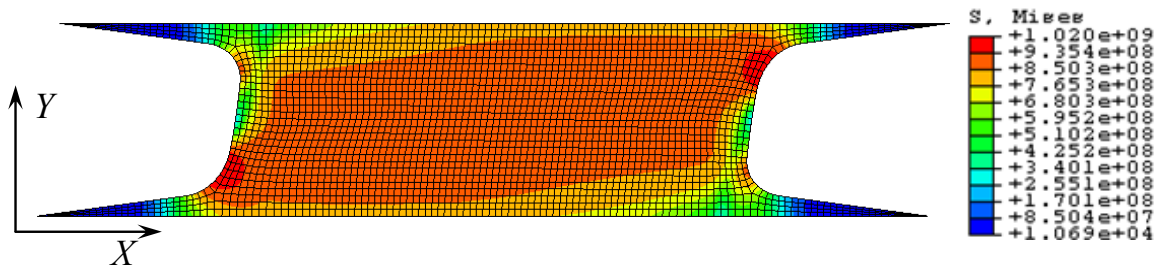
Figure 2.7: Finite element model of the full-thickness specimen subjected to loading $\beta=45^0$ and an imposed von Mises force of 35 kN (approximately the maximum experienced in testing before necking or fracture). The colors indicate the von Mises stresses acting on the specimen.
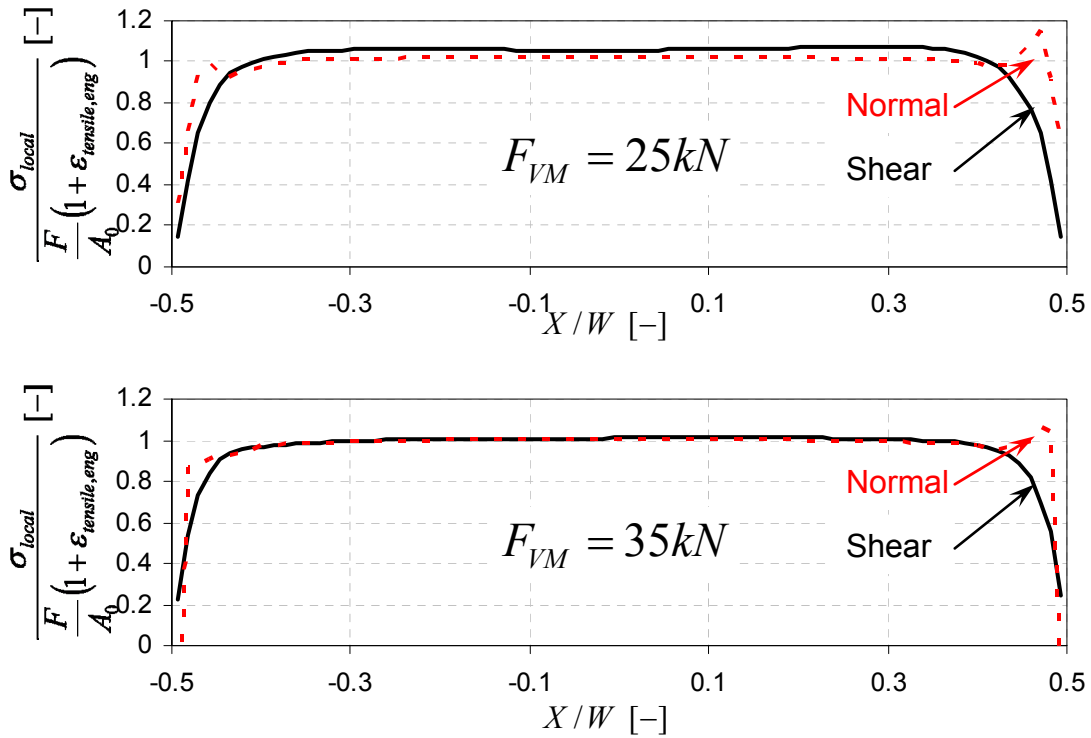
Figure 2.8: Cross-sectional distribution of shear and normal stresses in a full-thickness specimen at the vertical center line with $\beta=45^0$ at an imposed von Mises force of 25 kN (top) and 35 kN, approximately the maximum experienced in testing (bottom). The bottom plot corresponds to data taken from the stress state shown in Figure 2.7.

In addition to stress measurement, global strain measurement (i.e. the strain that is measureable in the experiment) must also be evaluated. As was indicated in the "Measurement" section, a DIC system is available which can measure the movement of two arbitrary points on the specimen relative to each other in two dimensions. The finite element model used in this study was meshed such that there are two horizontally centered nodes that are +/-2.5 mm from the vertical center of the specimen. The horizontal and vertical positions of these two nodes were retrieved from the results and used to evaluate the logarithmic strain in the specimen. The global (average) stress versus global logarithmic strain (i.e. the values that can be calculated from force sensor data and traditional analysis) for $\beta=45^0$ are plotted in Fig. 2.9 and compared with the Cauchy stress and logarithmic strain of the center element resolved into tension and shear components. As the global stress and strain represent parameters that can be determined from experimentation and the local ones represent the actual stress calculated locally by the finite element software, the difference between the two curves can be seen as the error of the specimen due to geometrical effects. The two tick marks ("X" and "+") indicated in Fig. 2.9 correspond exactly to the states of stress shown in Fig. 2.8. Similar comparisons between globally and locally determined stresses and strains for different β angles are shown in Fig. 2.10.
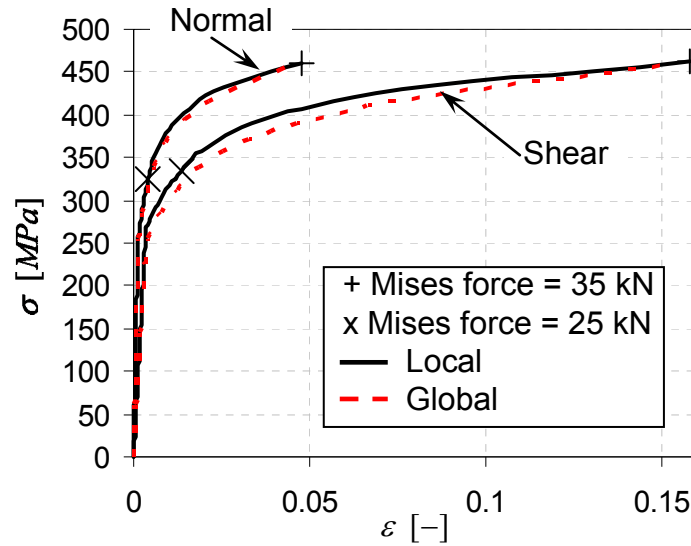
Figure 2.9: Analysis of a simulation comparing of Cauchy stresses and logarithmic strains on an element in the center of the specimen (local) with stresses calculated from forces acting globally on the specimen and motion of nodes measured +/-2.5 mm away from the center (global). The global case is intended to represent data available in an experiment. The condition shown corresponds to $\beta=45^0$, and the points indicated with "X" and "+" correspond to the states of stress shown in Figure 2.8.
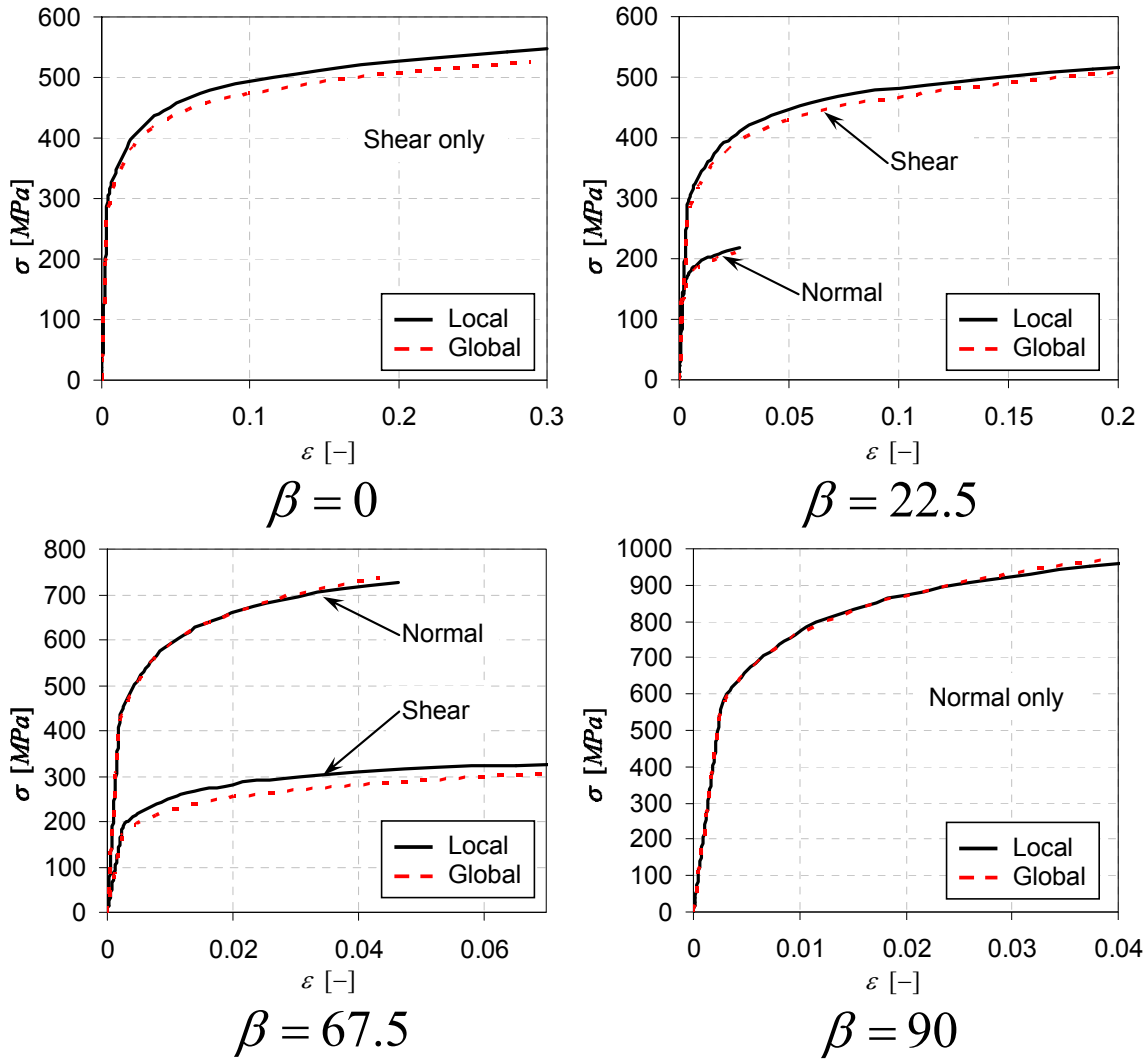
Figure 2.10: Globally-determined stress versus strain curves as compared to stresses and strains acting on an individual element. The globally-determined stress versus strain curves have been determined exclusively from parameters that can be directly measured in testing.

2.7 Plasticity Calibration

In a prior section, parameters of the Hill 1948 plasticity model were determined together with a hardening curve from uniaxial test data. The question is: is the traditional approach based on uniaxial test data will provide accurate results in the case of biaxial loading. To answer this question, an iterative procedure was developed in which the traditional data was used as the starting point in the iteration procedure. Introducing small changes in the hardening curve and the values of the Hill 1948 parameters, an improved set of parameters is obtained.

The plasticity model was calibrated through a procedure featuring the iterative modification of plasticity characterization and comparison of results between experiment and simulation.

Mohr and Oswald (2008) have shown that with their geometry, the stress fields in the specimen are sufficiently uniform that the engineering stresses and strains on a characteristic element within the material can be calculated by Eq. (2.6) – (2.9). Therefore, one can choose a single representative element.

$$\sigma_{normal,engineering} = \frac{F_V}{A_0} \tag{2.6}$$

$$\sigma_{shear,engineering} = \frac{F_H}{A_0} \tag{2.7}$$

$$\varepsilon_{normal,engineering} = \frac{Y_{top} - Y_{bottom}}{Y_{top,initial} - Y_{bottom,initial}} \tag{2.8}$$

$$\varepsilon_{shear,engineering} = \frac{X_{top} - X_{bottom}}{Y_{top,initial} - Y_{bottom,initial}} \tag{2.9}$$

The finite element model consisted of a single ABAQUS S4R shell element that was 1 mm cubed. The element had an associated material model defined in true stress versus true strain coordinates. A single node on the bottom of the element was constrained not to move, and the other bottom node was constrained such that it could move, but a portion of the loading from the fixed boundary condition was shared with it. Forces were applied to a node on the top of the element so that the element had the same level of engineering stresses that the specimen experienced during the experiment. The two nodes on the top of the element were constrained together so that the applied forces were shared appropriately across the top. This finite model was not intended to be geometrically representative of the specimen, but rather serve as a means of using ABAQUS to solve the material model for all of the states of loading applied to the specimen. The uniformity of stress shown by Mohr and Oswald (2008) justifies this analysis.

In the current thesis, the material plasticity was calibrated by a multi-step iterative approach. For the first iteration, the plasticity model was assumed to be identical to that found with the uniaxial tensile tests the uniaxial tests reported earlier in this paper. A finite element analysis was then run for each of the conditions for which experimental data was available, and the results of the finite element analysis were exported as engineering stress and strain relationships. The engineering force versus strain relationships were compared against the engineering stress versus strain relationships for all cases for both normal and shear conditions. In this analysis, the engineering stress versus strain relationships were not regarded as stress relationships, but rather normalized force and displacement relationships against which correlation could be judged. If the engineering stress versus strain relationships did not agree sufficiently well for all cases, then the material law in ABAQUS was modified, and another iteration was completed.

The results from uniaxial tests presented earlier in this paper provided evidence that an anisotropic model was necessary, but the simplicity of the von Mises model was desired. For this reason, both the von Mises model and the Hill 1948 model were calibrated for this material with the iterative procedure described above. The comparison of the engineering stress versus strain curves for the simulations with a von Mises material are compared to the experiments in

Figure 2.11. The comparisons of experiment with simulation for the Hill 1948 material model are shown in Figure 2.12.

The hardening curves for both the von Mises material and the Hill material are compared with the uniaxial test data from Fig. 2.1 in Fig. 2.13. The elastic parameters along with the Hill anisotropic parameters are presented in Table 2.1, and the resulting hardening curves for both the von Mises and Hill characterizations are presented in Table 2.2. This material can also be described very well with the power-law plasticity model shown in Eq. (2.10).

$$\overline{\sigma} = C\overline{\varepsilon}^{n_H} \tag{2.10}$$

where C and n_H are material calibration constants and are 1208. MPa and 0.133, respectively. As can be seen by comparing Figures 2.11 and 2.12, there is very little difference between the two characterizations for the material when tested in-plane. The results from the iterative calibration of the biaxial stress-strain relationships and the analysis on the uniaxial tensile specimen both indicate that the anisotropy for this material comes primarily from its out-of-plane behavior, and that its in-plane behavior is approximately isotropic.
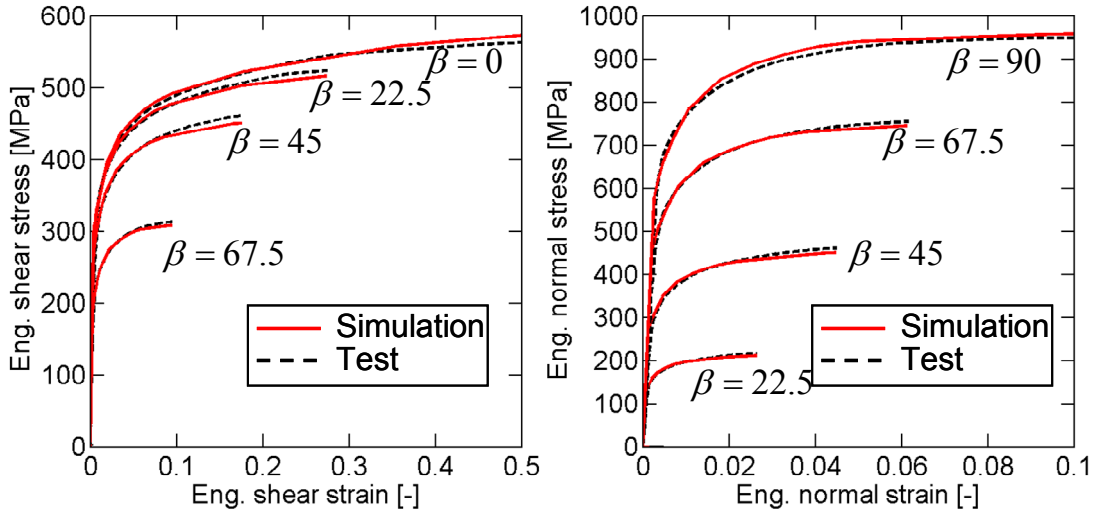
(a) Tensile axis aligned with rolling direction
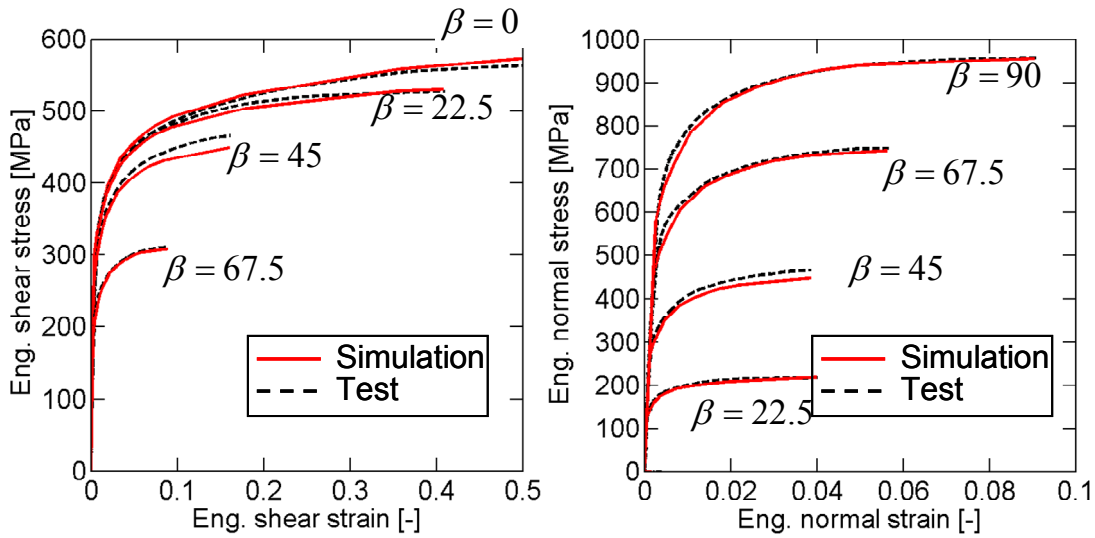
(b) Tensile axis perpendicular to rolling direction

Figure 2.11: Comparison of ABAQUS single-element simulation with a von Mises material against experiments for Mohr and Oswald (2008) specimen.
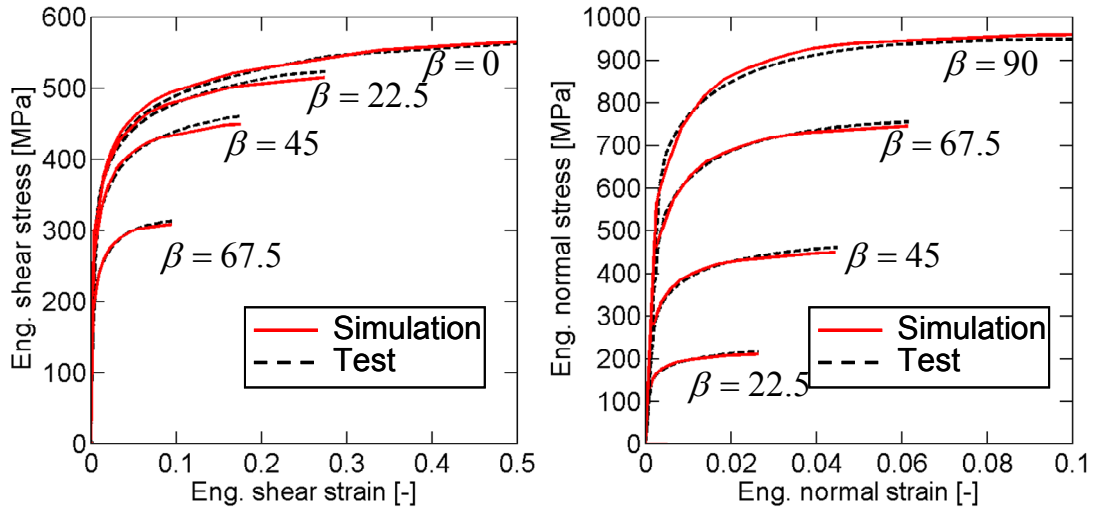
(a) Tensile axis aligned with rolling direction
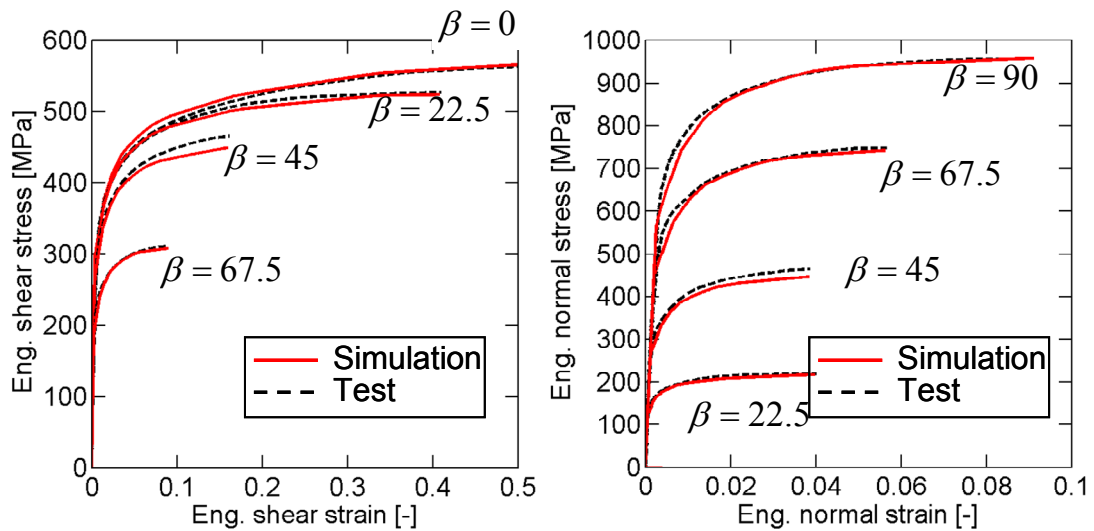
(b) Tensile axis perpendicular to rolling direction

Figure 2.12: Comparison of ABAQUS single-element simulation with a Hill '48 material against experiments for Mohr and Oswald (2008) specimen.
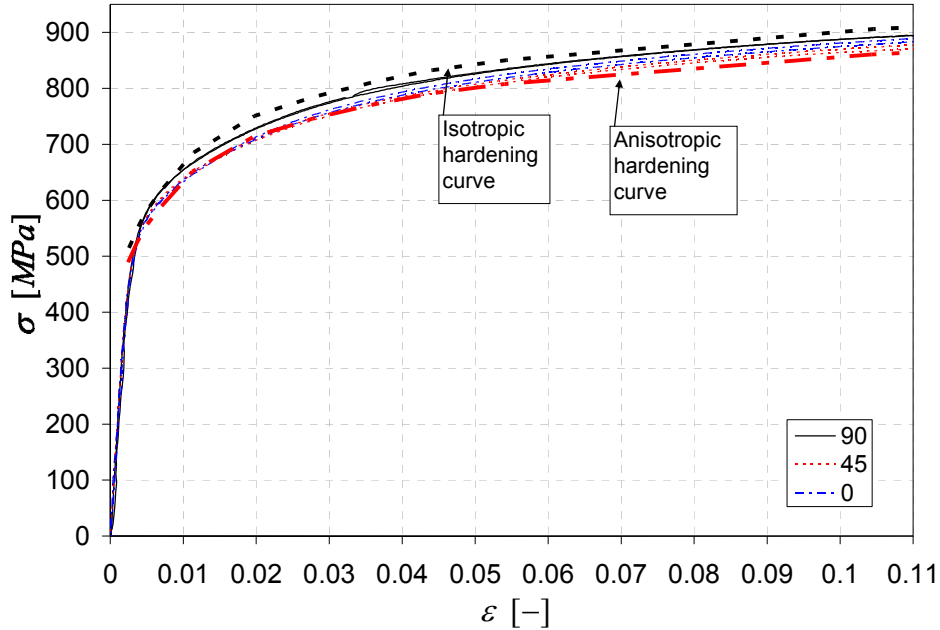
Figure 2.13: Comparison of true stress versus true strain hardening curves found through iterative procedure for both the von Mises material and the Hill material against uniaxial test data. The iterative procedure was performed on experiments with the Mohr and Oswald (2008) specimen.

Table 2.1: Hill anisotropic parameters

E [Gpa]	n [-]	F	G	H	L	M	N
200	0.3	0.4363	0.4357	0.5643	1.5	1.5	1.3477

Table 2.2: Hardening curves for both Hill and von Mises characterizations

Plastic Strain	Yield Stress, MPa	
[-]	Hill	Mises
0	489.3	515.
0.001	522.1	549.6
0.002	550.4	579.4
0.004	588.5	619.5
0.008	651.1	685.4
0.016	712.9	750.4
0.024	745.5	784.7
0.032	770.5	811.
0.04	790.8	832.4
0.05	807.8	850.3
0.1	860.5	905.8
0.2	917.7	966.
0.4	978.5	1030.6
0.6	1007.	1060.7
1	1064.	6177.

51

2.8 Full-Thickness Model Validation

To validate the plasticity models determined above, a test was performed and simulated that represented a state of stress not employed in the calibration. This experiment captured the equi-biaxial state of stress due to membrane stretching. The experimental apparatus is summarized in Fig. 2.14. In this apparatus, a circular plate was clamped into a circular die, then punched with a hemispherical punch. The radius of the die (R_0) was 24.6 mm; the radius of the punch (R_b) was 22.2 mm. The punch was loaded with a 200 kN electromechanical loading frame. The force was measured with a 200 kN MTS load cell. Displacements were measured through VIC-3D, which is a Digital Image Correlation (DIC) package made by Correlated Solutions, Inc (West Columbia, SC). This system is different from VIC-2D in that it uses two cameras (rather than one) and is able to measure out-of-plane motion. A MATLAB script was created that interprets the VIC-3D displacement field output by first identifying the center of the specimen, then creating a history of the out-of-plane displacement of the center point.

The finite element model used the S4R shell element in ABAQUS to simulate the experiment with both the von Mises and the Hill material models determined iteratively, as described above. The die and the punch were modeled as rigid analytical geometry. Comparison of the test data for the force-deflection relationship against the simulations is presented in Fig. 2.16. It can be seen that both material models produce very good results for this condition.
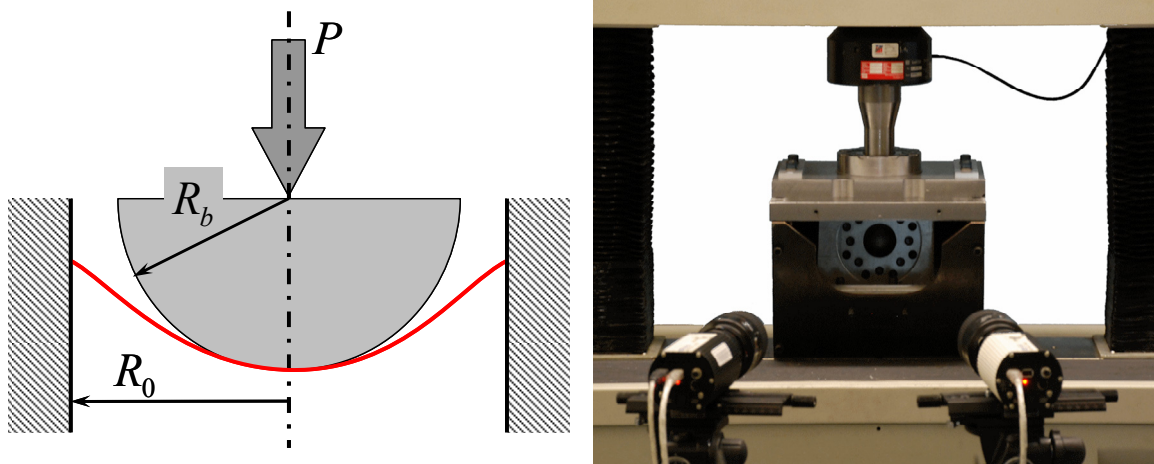
Figure 2.14: Experimental apparatus for punch test in schematic form (left) and in physical form (right)
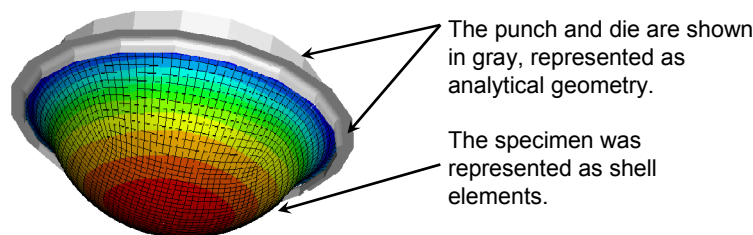
Figure 2.15: Finite element model of punch tests showing the key geometrical features.
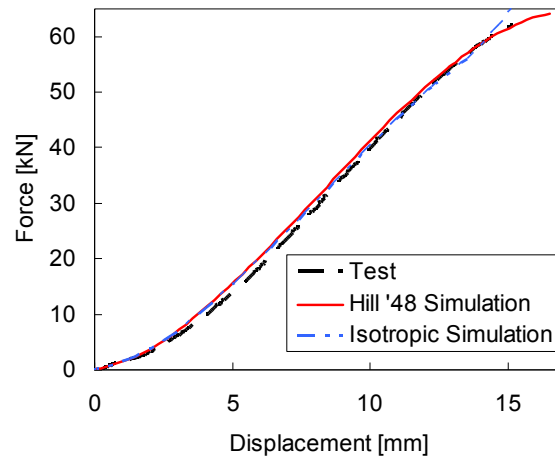
Figure 2.16: Comparison of punch experiment with FEA prediction with calibrated model and with von Mises material. Both the von Mises and Hill models are able to capture the in-plane behavior.

2.9 Evaluation of Through-Thickness Inhomogeneity

The comparison of the engineering stress versus strain curves obtained experimentally for both the original symmetrical Mohr and Oswald (2008) specimens and the asymmetrical specimens is shown in Fig. 2.17. The asymmetrical specimen had lower stresses than the symmetrical one in some cases, but not others. In other cases, they agreed exactly. The difference between the cases can be seen as scatter in the experimental measurements, and the material is therefore concluded to have negligible through-thickness inhomogeneity in the plasticity parameters.
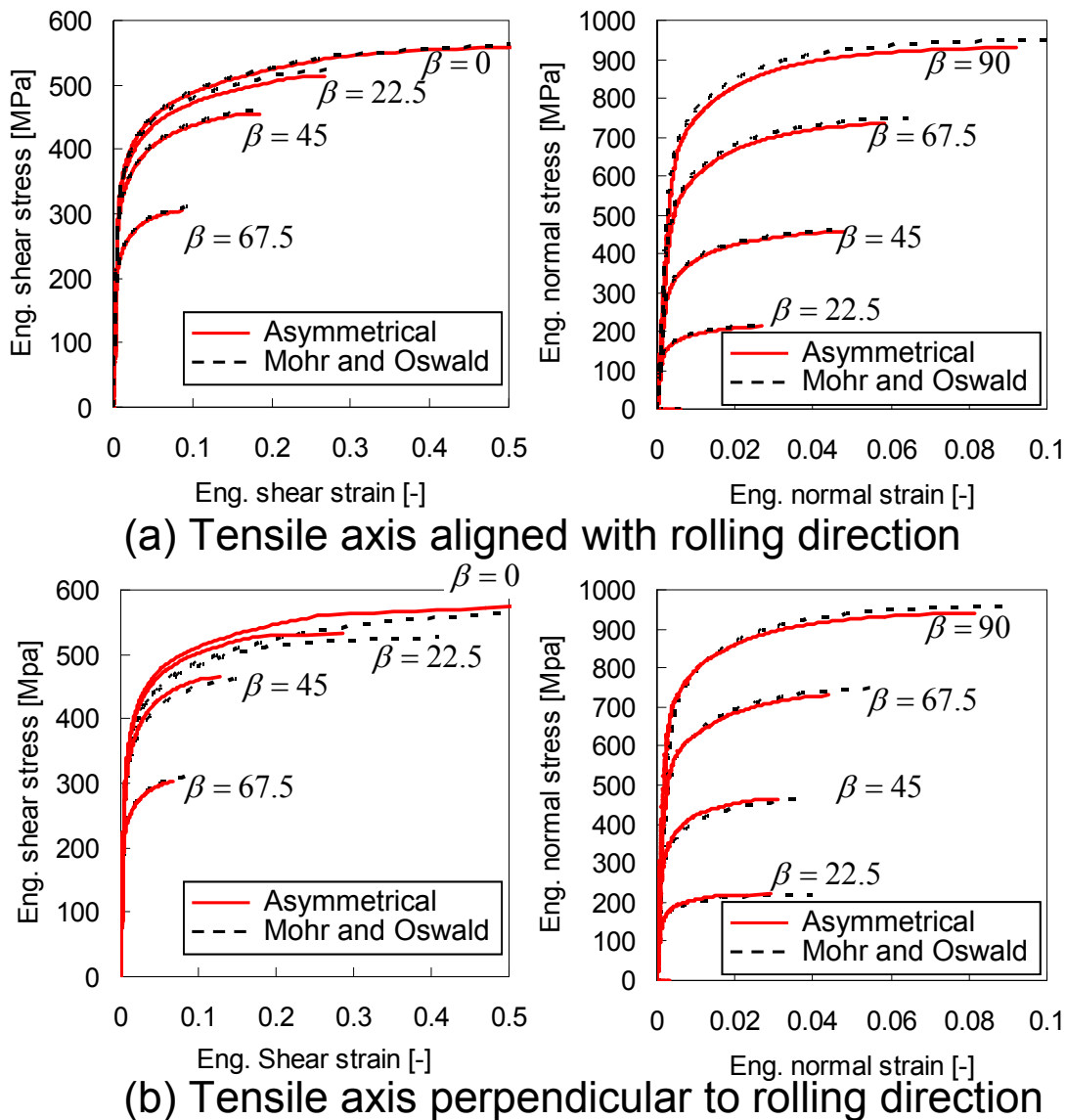
Figure 2.17: Comparison of symmetrical and asymmetrical specimens

2.10 Comparison of Full Thickness Specimen to Reduced Thickness Specimen

A comparison of the test results from the Mohr and Oswald (2008) specimen with the reduced thickness against the full-thickness specimen is shown in Fig. 2.18. Assuming that the Mohr and Oswald (2008) specimen gives a reasonably accurate representation of the stress and strain behavior of a central element, we can see that the full-thickness specimen consistently under-predicts the stress for a given strain for all loading angles. This outcome can be attributed to the stress concentrations due to the specimen geometry and was predicted by the finite element analysis presented in Fig. 2.10. Based on the finite element model and its verification through testing, some conclusions can be reached on the accuracy of the of the full-thickness specimen in predicting the stress and strain states of the material.

54
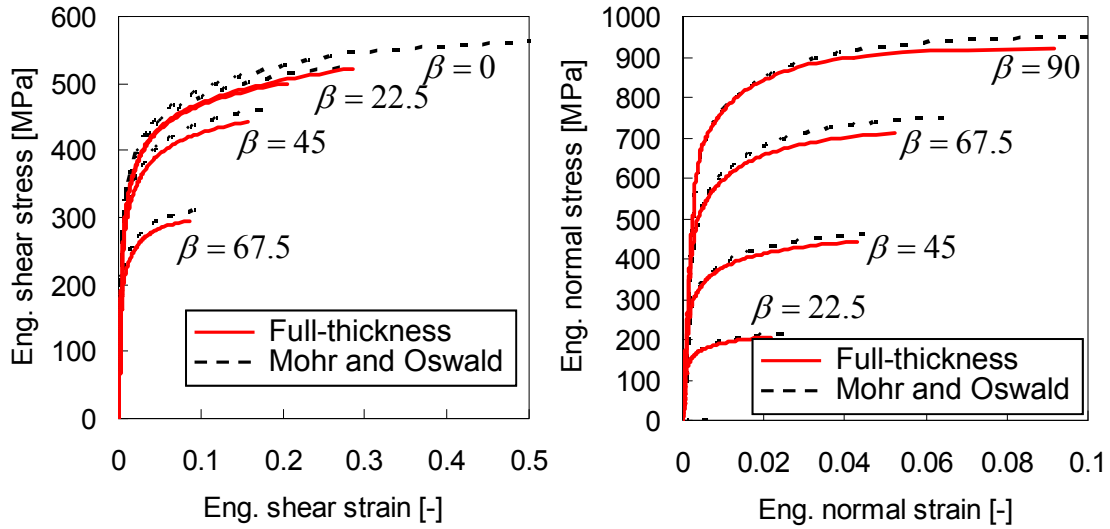
Figure 2.18: Comparison of test data with Mohr and Oswald (2008) specimen with the full-thickness specimen presented in this paper.

The full-thickness specimen performs better in representing tensile stress than shear stress. The tensile state of stress as determined from the global force measurements is consistently within 5% of the stress of a central element. Use of the full-thickness specimen tends to under-predict the shear stress in conditions of low shear stress. This effect can be seen especially by inspecting the condition of β=67.5 in Fig. 2.10. The error in for both tensile stresses and shear stress typically starts off high and decreases throughout the deformation, so the stress values determined for higher states of strain are more reliable.

Analysis of the full-thickness specimen typically under-predicts the tensile strain by approximately 5% for all cases. Of the conditions investigated (β=0, 22.5, 45, 67.5, and 90) shear strain was inconsequential for the case of β=90 and within 1% error for the case of β=67.5. For all other cases, the error of the shear strain was under-predicted by approximately 5%.

2.11 Conclusions

The Advanced High Strength Steel DP780 was calibrated for both von Mises and Hill 48 plasticity models. Both models fit the data very well for in-plane loading for various combinations of tension and shear. Both models also agree very well with an experiment for equi-biaxial tension. However, careful analysis of the Lankford parameters has shown that an anisotropic model (e.g. Hill 48) is necessary for capturing out-of-plane behavior. The material did not exhibit significant variations in mechanical properties through the thickness, so the Mohr and Oswald (2008) specimen was deemed appropriate for this material.

The proposed full-thickness specimen is promising for approximate flow parameters, but it has enough stress concentrations that iterative simulation with a simplified finite element model or traditional methods of calculating stress and strain from experimental data do not produce

sufficiently accurate measurements for good characterization. However, the full-thickness specimen could provide a reasonable basis for iterative calibration featuring a finite element model with more detailed geometric representation of the specimen. Alternatively, comparison of test data taken from the full-thickness specimen against a finite element simulation of the experiment can be used as a rigorous validation of an in-plane plasticity model. Due to the constraints in developing the full-thickness specimen, the current geometry is considered to be close to optimal for the available test equipment. Further improvements in stress homogeneity due to geometrical optimizations are not anticipated within the constraints of the available testing equipment. However, the specimen improved consistently with increased width, and the width of the test section was constrained by the maximum force of the available test equipment. A higher capacity biaxial test frame could allow for enough increase in width that this specimen can be re-optimized to produce considerably better results and be applicable for general calibrations.

Chapter 3

Characterization of Quasi-Static Fracture

3.1 Abstract

An Advanced High Strength Steel (AHSS) was characterized for fracture with two different methods, and the results are compared. The first method, representative of procedures used in the sheet metal forming industry, features specimens with different shapes being punched out of plane by a hemispherical punch. By changing the shape of the specimen, different the states of stress (triaxiality and Lode parameter) in the specimen are obtained. In the other method, the specimen featured a lofted cutout geometry in the center, all of the specimens were the same shape, and the state of stress was changed by applying different combinations of shear and tensile forces to the specimen.

Comparison between the two methods showed that while the states of stress achieved in the methods spanned different ranges of triaxiality and Lode parameter, both methods agreed very well for the modified Mohr Coulomb fracture surface with the same set of calibration parameters. One key limitation of the punching test was that it produced stress triaxialities over such a limited range that the calibration based solely on the punching test was valid for only a small range. However, the method featuring the lofted cutout spanned a large enough range of stress triaxiality and Lode parameter that it was more widely applicable. The addition of one shear test to the punch tests would greatly improve the range of its applicability.

3.2 Introduction

A summary of the historical development of a fracture methodology has been given in Chapter 1. The introduction in this chapter will focus only on areas specifically relevant to this chapter. The current fracture locus, known as the Modified Mohr-Coulomb (MMC) fracture criterion, was first presented by Bai (2008). This relationship is shown in equation form in Eq. (3.1) and graphically in Fig. 3.1.

$$\bar{\varepsilon}_f^p = \left\{ \frac{C}{c_2} \left[c_3 + \frac{\sqrt{3}}{2-\sqrt{3}}(1-c_3)\left(\sec\left(\frac{\bar{\theta}\pi}{6}\right)-1\right) \right]\left[\sqrt{\frac{1+c_1^2}{3}}\cos\left(\frac{\bar{\theta}\pi}{6}\right)+c_1\left(\eta+\frac{1}{3}\sin\left(\frac{\bar{\theta}\pi}{6}\right)\right) \right] \right\}^{-\frac{1}{n_H}}$$

(3.1)

where c_1, c_2, and c_3 are material constants to be found from a suitable calibration procedure. C and n_H are the constants from the power hardening law ($\bar{\sigma} = C\bar{\varepsilon}^{n_H}$). The stress variables η (stress triaxiality) add $\bar{\theta}$ (Lode parameter) were defined earlier.
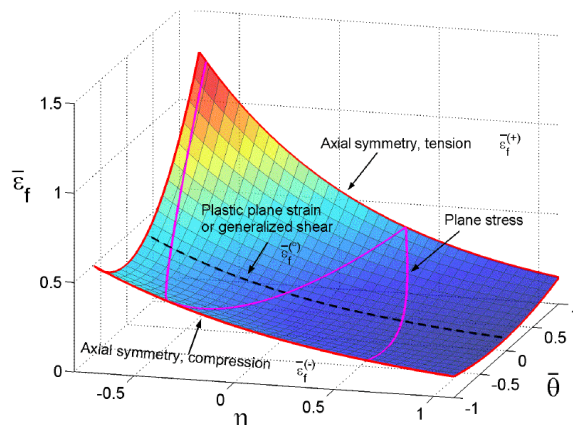
Figure 3.1: Fracture model proposed by Y. Bai, in which ductility depends on stress triaxiality (η) and the deviatoric state parameter ($\bar{\theta}$). After Bai, 2008.

The MMC criterion showed very good agreement with a variety of different scenarios and built upon a long history of fracture development. As well, the procedure developed for calibration of the MMC (biaxial testing of a special butterfly specimen) had shown promise for producing an accurate calibration. However, the MMC criterion as well as the calibration procedure were primarily designed and validated for bulk materials.

The sheet metal industry had developed its own methodologies culminating in the Hasek test, which is a battery of experiments in which a sheet metal membrane is punched laterally to necking and fracture. The sheet metal industry had a strong history with the Forming Limit Diagram (FLD) and the Fracture Forming Limit Diagram (FFLD), which are beginning to encounter limitations in their ability to predict fracture in simulation.

Calibration of the MMC with both butterfly and punch-style experiments could lend insight into both the applicability of Bai's (2008) approach to sheet metal fracture as well as the limitations of the traditional approach of punching tests coupled with FLD's and FFLD's.

3.3 Hasek Experimental Setup

Hasek's (1978) punching fracture experiment features a sheet metal specimen clamped into a circular die. The state of stress in the specimen is controlled through diametrically-opposed arced cutouts on the specimen, located on the circumference of the die. A schematic representation of the specimen is shown in Fig. 3.2. By changing the radius of the cutout, the state of stress in the material due to punching can be changed from equi-biaxial (the radius of the cutout R_N is zero) to almost uni-axial (R_N is very close to the die radius R_0). A schematic

representation of Hasek's (1978) specimens and the experimental configuration can be seen in Fig. 3.2. For all cases presented in this thesis, $R_b = 22.225mm$ and $R_0 = 24.5mm$. The cutout radii (R_N) tested are listed in Table 3.1. All of the Hasek specimens were cut with the tensile axis perpendicular to the rolling direction.

Traditionally, fracture strain on punch-style sheet metal fracture tests was found through the deformation of inscribed circles or squares on the surface of the material. With this method, strains could only be measured post-mortem. In the current investigation, there was interest in measuring the surface strains throughout the experiment, so Digital Image Correlation (DIC) was used. The die was raised up from the bottom of the machine by a stiff steel fixture, and a first-surface mirror tilted 45 degrees from the horizontal was inserted underneath the die so that the deformation would be visible to the cameras. A picture of the setup is shown in Fig. 3.3. The VIC-3D software from Correlated Solutions, Inc. in Columbia, SC was used to interpret the stereo-optic digital pictures into deformations and strain fields. For all cases, the pictures were recorded as uncompressed .tif images that were 1300 pixels wide by 1030 pixels tall. This resulted in each pixel corresponding to approximately 0.06 mm. All specimens were speckled to create a random pattern that the DIC algorithm could track. For the Hasek experiments presented here, the speckle pattern was created with DYKEM Steel Blue Layout Fluid prayed over bare metal. Layout fluid was used in lieu of spray paint because spray paint (even high-quality fabric spray paint) has shown a tendency to shear from the metal due to the very high strains possible in equi-biaxial tests. The layout fluid had the serendipitous advantage that because it is semi-transparent, more unique patterns could be achieved when speckles overlap because the overlapping speckles have a different level of opacity (seen as darkness in grayscale pictures) than non-overlapping speckles.
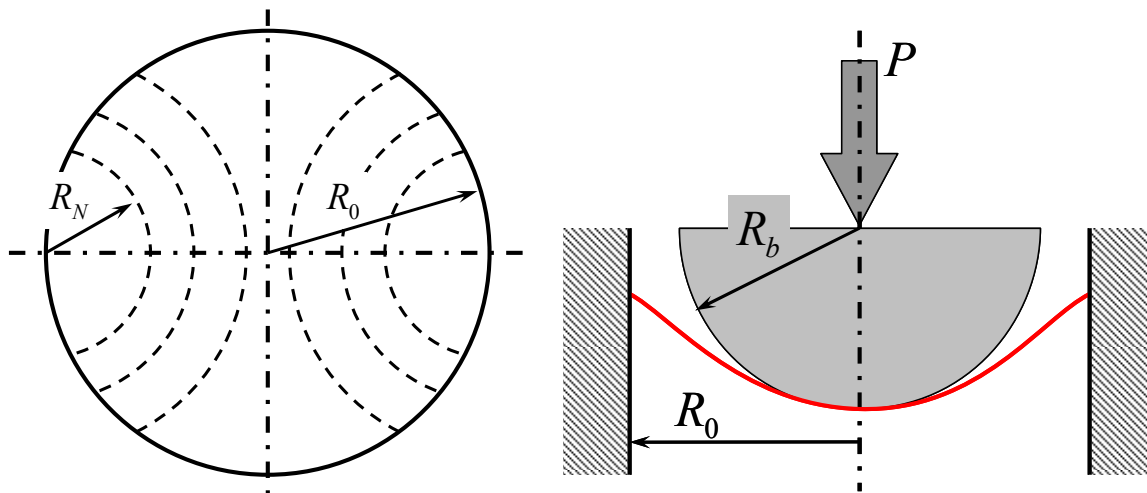
Figure 3.2: Hasek specimen geometry ranging from equi-biaxial ($R_N = 0$) to almost uni-axial ($R_N \cong R_0$), depending on the cutout radius (left) and the schematic representation of the circular clamped die and loading of these specimens by a hemispherical punch (right).

Table 3.1: Values of cutout radii (R_N) tested in the quasi-static regime

Case	1	2	3	4	5	6	7	8	9
$R_N [mm]$	22.154	19.692	17.846	16.000	14.154	12.308	9.846	4.923	0.000
$R_N / R_0 [-]$	0.904	0.804	0.728	0.653	0.578	0.502	0.402	0.201	0.000

For all conditions listed in this paper, the contact between the punch and the specimen was lubricated by five layers of 0.05 mm thick Teflon, with metal-free anti-seize lubricant between each layer. This combination of Teflon and lubricant has been found to produce negligible friction. For all specimen geometries, the specimen cracked in the center, and the crack ran parallel to the rolling direction of the material. This is considered to reflect a sufficiently low friction because prior tests that featured less or no Teflon had cracks that were off-center. The post-test specimens are shown in Fig. 3.4.
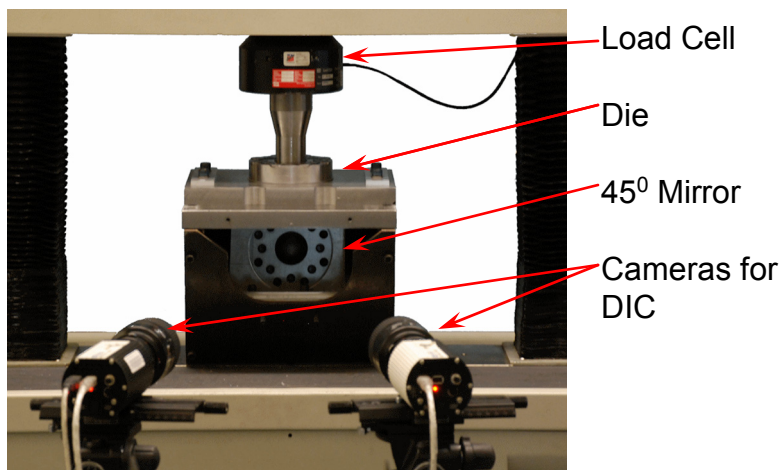
Figure 3.3: Physical implementation of the Hasek test featuring two cameras for Digital Image Correlation (foreground), a first-surface mirror underneath the specimen to reflect the image of the specimen being deformed (below the die), and a punch mounted onto a 200 kN load cell on an Electro-Mechanical screw-driven testing machine.
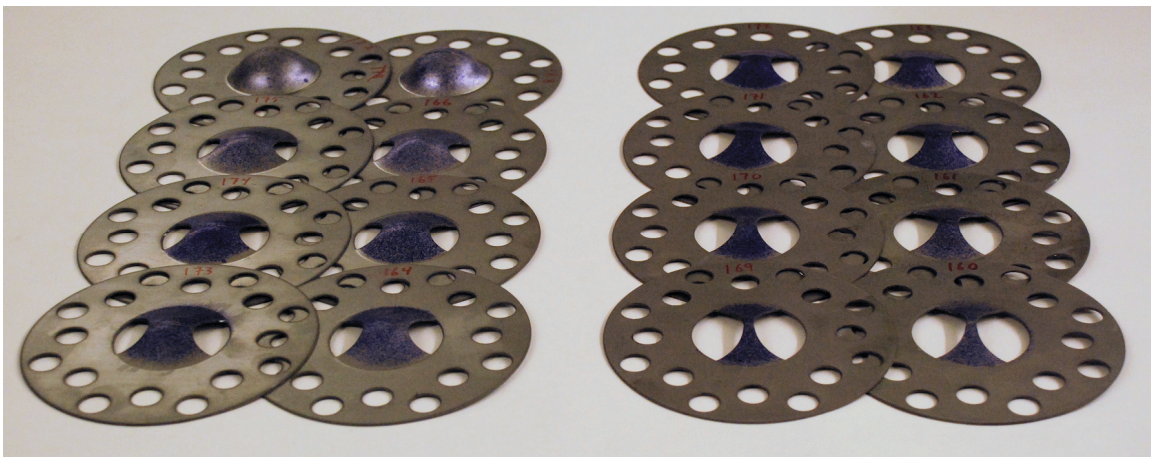
Figure 3.4: Battery of Hasek experiments after fracture.

3.4 Analysis of the Hasek Experiments

The goal of the current testing program is to find the effect of stress triaxiality and Lode parameter on fracture. Therefore, it is of key interest to measure these parameters from the data available: force and surface strains. These parameters are calculated in this paper directly from the strain data available from DIC.

Because DIC measures only strains, and stress triaxiality and Lode parameter are defined in terms of stress, a plasticity model is first needed. The material used in this study has been identified as transverse isotropic Hill 1948 material in Chapter 2. Hill's 1948 equivalent stress is shown in Eq. (3.2).

$$\bar{\sigma}_{Hill} = \sqrt{F(\sigma_{22} - \sigma_{33})^2 + G(\sigma_{33} - \sigma_{11})^2 + H(\sigma_{11} - \sigma_{22})^2 + 2L\sigma_{23}^2 + 2M\sigma_{13}^2 + 2N\sigma_{12}^2} \qquad (3.2)$$

Transverse anisotropy implies the Hill parameters F=G and H=1-F, and for the current material, F=0.436. The material being tested is sheet metal, which implies plane stress throughout most of the deformation. Also, only surface strains are being measured, and the stress at the free surface of the specimen will always be in the state of plane stress. Also, because the material the anisotropy of the material comes from the out-of-plane direction, it can be treated as isotropic in plane. Therefore, the stress and strain space can be freely rotated into principal stress/principal strain space. In this paper, principal stresses and strain states will be denoted by subscript Roman numerals with $\sigma_I \geq \sigma_{II} \geq \sigma_{III}$. The equivalent stress is simplified for principal plane stress with the transverse anisotropic condition, as shown in Eq. (3.3). The work conjugate incremental equivalent plastic strain is given in Eq. (3.4).

$$F = \bar{\sigma}_{Hill} - \sqrt{\sigma_I^2 + 2(F-1)\sigma_I \sigma_{II} + \sigma_I^2} \qquad (3.3)$$

$$d\bar{\varepsilon}^P = \frac{1}{\sqrt{F(2-F)}} \sqrt{(F+H)(d\varepsilon_i^p)^2 + (H+G)(d\varepsilon_{Ii}^p)^2 + 2H(d\varepsilon_I^p)(d\varepsilon_{II}^p)} \qquad (3.4)$$

The Levy-Mises flow rule is shown in Eq. (3.5).

$$d\varepsilon_{\alpha\beta} = d\lambda \frac{df}{d\sigma_{\alpha\beta}} \qquad (3.5)$$

Assuming that elastic strains are negligible, application of the Levy-Mises flow rule and the definition of the strain rate ratio produces the relationships given in Eq. (3.6) and (3.7). Application of the definition of the strain rate ratio to the incremental equivalent plastic strain produces the relationship in Eq. (3.8)

$$\sigma_I = \bar{\sigma} \frac{1 - \alpha F + \alpha}{\sqrt{2F - F^2 + \alpha(4F - 6F^2 + 2F^3) + \alpha^2(2F - F^2)}} \qquad (3.6)$$

$$\sigma_{II} = \bar{\sigma} \frac{\alpha - F + 1}{\sqrt{2F - F^2 + \alpha(4F - 6F^2 + 2F^3) + \alpha^2(2F - F^2)}} \tag{3.7}$$

$$d\bar{\varepsilon}^P = \frac{1}{\sqrt{F(2-F)}} d\varepsilon_I^P \sqrt{1 + \alpha + \alpha^2} \tag{3.8}$$

where the strain-rate ratio (α) given in Eq. (3.9) is assumed.

$$\alpha \equiv \frac{d\varepsilon_{II}}{d\varepsilon_I} \tag{3.9}$$

The definition of the mean stress is given in Eq. (3.10). The Von Mises stress for principal, plane stress space is given in Eq. (3.11). The definition of the stress triaxiality is given in Eq. (3.12).

$$\sigma_m = \frac{1}{3}(\sigma_I + \sigma_{II} + \sigma_{III}) \tag{3.10}$$

$$\sigma_{VM} = \sqrt{\sigma_I^2 - \sigma_I \sigma_{II} + \sigma_{II}^2} \tag{3.11}$$

$$\eta = \frac{\sigma_m}{\sigma_{VM}} \tag{3.12}$$

Substitution of Eq. (3.7), (3.8), (3.10), and (3.11) into Eq. (3.12) gives an expression for the stress triaxiality expressed only in terms of the anisotropy constant F and the strain rate ratio α, shown in Eq. (3.13).

$$\eta = \frac{(\alpha + 1)(2 - F)}{3\sqrt{(1 - F + F^2) + \alpha(2 - 2F - F^2) + \alpha^2(1 - F + F^2)}} \tag{3.13}$$

The Lode parameter is defined in Eq. (3.14) in terms of the third invariant of the stress tensor, $\bar{\theta}$. The plane stress assumption ($\sigma_{III} = 0$) implies that the Lode parameter is uniquely related to the stress triaxiality, Eq. (3.15).

$$\bar{\theta} \equiv 1 - \frac{2}{\pi} \cos^{-1}\left[\left(\frac{r}{\sigma_{VM}}\right)^3\right] \tag{3.14}$$

$$\bar{\theta} = 1 - \frac{2}{\pi} \cos^{-1}\left[\left(-\frac{27}{2}\eta\left(\eta^2 - \frac{1}{3}\right)\right)^3\right] \tag{3.15}$$

The DIC software automatically determines strains from the deformation of the specimen and resolves them into principal strains. The strain that the system delivers is Lagrange strains. The Lagrange strains are converted into logarithmic strains through the relationship:

62

$$\varepsilon_{\log} = \frac{1}{2}\ln\left(2\varepsilon_{Lagrange} + 1\right)$$ (3.16)

All of the tests were processed with the DIC system with a subset of 35 and a step of 5. The subset represents the size of a square, in pixels, that is used to correlate the location on one image to the next. The step indicates the number of pixels between point that is tracked. Further details can be found in Sutton et. al. (2000).

Each of the experiments was analyzed with VIC-3D with the same user settings. Text files were exported from VIC-3D into text formats. A MATLAB script was written that interpreted the VIC-3D output. The MATLAB script found the point of maximum deflection (assumed to be the center of the specimen), then evaluated the stress triaxiality and effective plastic strain at that point for a series of photograph sets associated with different times of the test. The MATLAB software then evaluated the strain average of the stress triaxiality and Lode parameter, given in Eq. (3.17). This strain averaging technique reflects the methodology set for in Bao (2003).

$$\eta_{AV} = \frac{1}{\bar{\varepsilon}_f^P}\int_0^{\bar{\varepsilon}_f^P}\eta d\bar{\varepsilon}^P \qquad , \qquad \bar{\theta}_{AV} = \frac{1}{\bar{\varepsilon}_f^P}\int_0^{\bar{\varepsilon}_f^P}\bar{\theta}d\bar{\varepsilon}^P$$ (3.17)

This analysis produced the effective plastic strain to fracture along with averaged Lode parameters and stress triaxialities for each case, which will form the basis for a fracture calibration based on Lode parameter and stress triaxiality.

Note that with Eq. (3.17), the average is processed over the effective plastic strain, which is a time-like parameter. Stress triaxiality, Lode angle, and strains are not spatially averaged, but only taken for the center point, which is considered to be the most critical point.

3.5 Comparison of DIC and FEA for Fracture Punch Experiments

As an alternative to the interpretation of DIC data into stress space, an Abaqus implicit FEA model was also used to interpret the effective plastic strain, stress triaxiality, and Lode parameter associated with each experiment. The model for one condition is shown in Fig. 3.5. All models consisted of the same three components: a hemisphere, a die, and the specimen. The hemisphere and die were both modeled as analytical rigid geometry; the faceted surfaces shown in Fig. 3.6 are only for visualization. The specimen was modeled with quadrilateral shell elements with 11 integration points through the thickness. Each model was adjusted geometrically to reflect the specimen it was simulating for both thickness and the size of the cutouts, when appropriate. Contact was specified between the punch and the specimen and between the die and the specimen. The material model described at the beginning of this section was applied to the specimen. Force and displacement were recorded for each specimen and correlated to those measured in experimentation. An example of this correlation is shown in Fig. 3.6 for the two most extreme cases and one in the middle.

The punch and die are shown in gray, represented as analytical geometry.

The specimen was represented as shell elements.
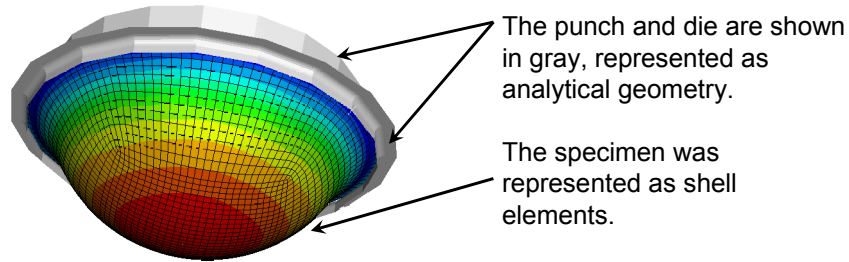
Figure 3.5: Finite element model of the experiment, showing the specimen along with the analytical rigid die and punch. Note that the faceting on the analytical rigid surfaces is only for display.
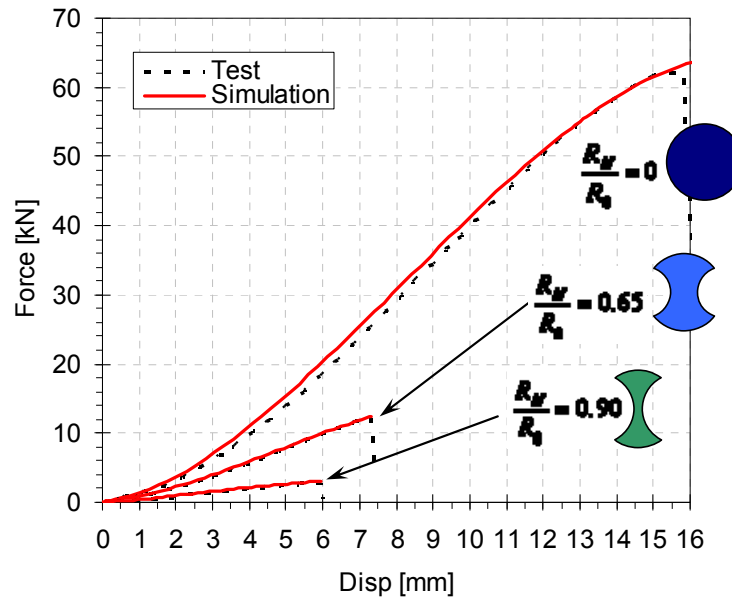
Figure 3.6: Sample correlation of force-deflection curves comparing test and the finite element simulation for the two extreme cases plus one in the middle.

A comparison between the stress triaxialities and Lode parameters calculated from simulation and from analysis of DIC is shown in Fig. 3.7. This comparison has some very interesting features. First of all, the qualitative agreement is very good between the simulation and the DIC, and the magnitude is approximately correct. Also, major features that are present in the experiment were capture by both the simulation and the DIC interpretation. For example, in the case of $R_N / R_0 = 0.65$, it can be seen that the stress state starts off as approximately equi-biaxial ($\alpha = 2/3$), but then changes with very little change in effective stress when the effective strain reaches 0.1. This feature is captured by both the simulation and the DIC, and it is explained by close inspection of the FE simulation. In this case, the very tip of the punch encounters the center of the specimen, far from the edges that are introduced by the cutouts. At this point, it acts as if it is equi-biaxial (similar to the specimen with no cutouts). As the hemisphere continues to punch into the specimen, eventually the deformed region of the plate reaches to the cutouts of the specimen. At that point, the strain in the center of the specimen doesn't change appreciably as the punch continues to advance, and the state of stress changes to account for the

interaction of the deformation field with the edges introduced by the cutouts. This effect is particularly dramatic when seen in terms of the Lode parameter, which changes from almost negative unity to almost positive unity.

As another point of evaluating the simulation and DIC analysis, an analytical solution exists for the stress triaxiality of the equi-biaxial case; if $R_N / R_0 = 0$, then $\alpha = 1$, and $\eta = 2/3$. Not only is this theoretical value reproduced by both the DIC analysis and the finite element analysis, but the correlation is so close that only one of them can be seen on the plot.
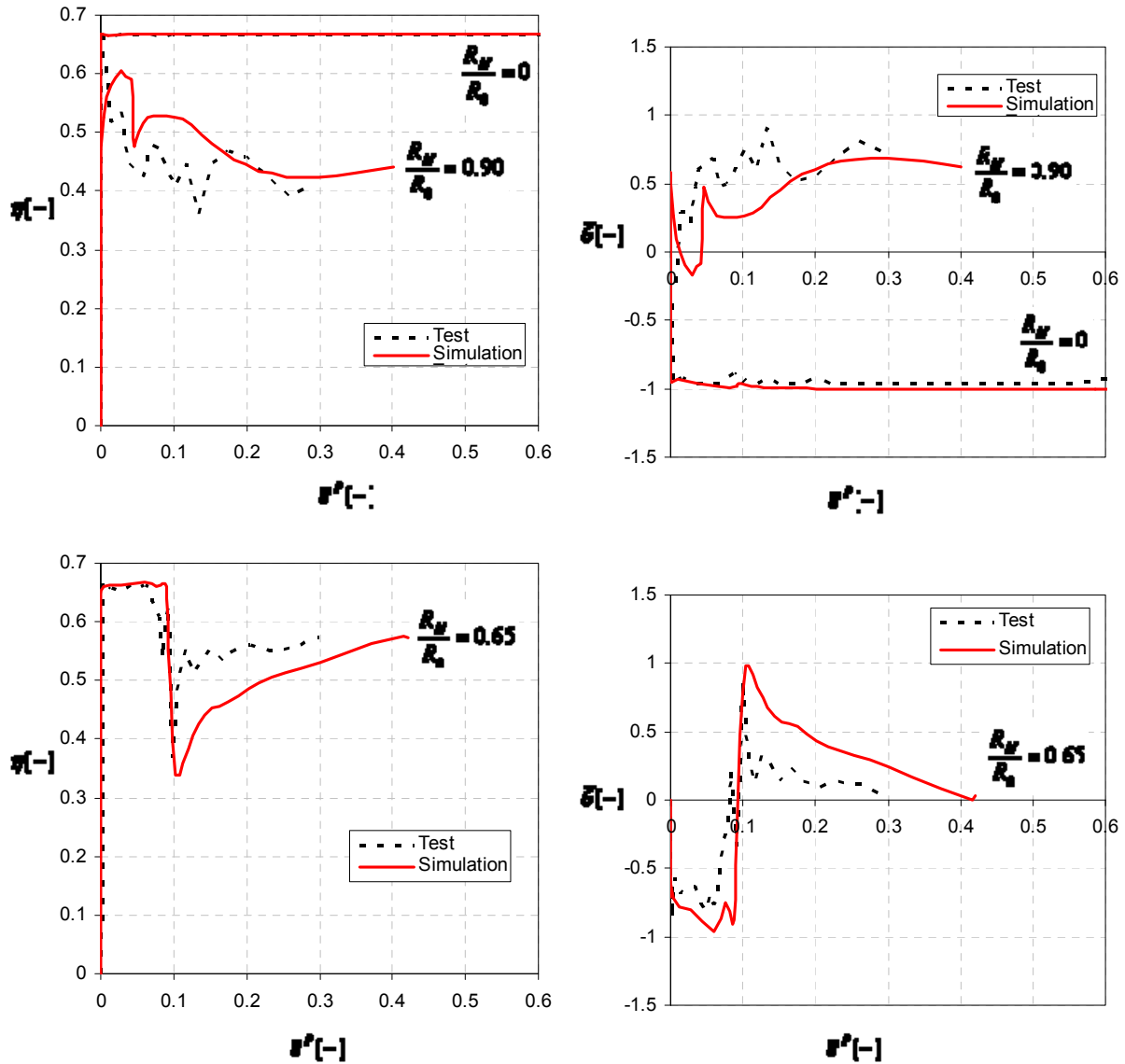
Figure 3.7: History of the evolution of stress triaxiality (left) and Lode parameter (right) for the two extreme cases (top) and an intermediate case (bottom). The Lode angle and stress triaxiality for the test were determined directly from DIC measurements whereas the simulation was taken from an Abaqus simulation of the experiments.

3.6 Evaluation of Shell FEA Model for Simulation of Punch Experiments

In order to verify the applicability of a shell element model and the assumption that fracture would start at the outside surface, a detailed model meshed with solid elements was created and executed for three critical punch experiments. The specimen was meshed with 16 elements through the thickness, resulting in the through-thickness element edge length of approximately 0.063 mm for all specimens. The typical in-plane edge length near the center for the middle and full-circle cases were approximately 0.3mm, and the typical in-plane edge length near the center for the narrow case was approximately 0.12mm. The models exploited quarter symmetry for reduced simulation time. Each of them was modeled with the same rigid surfaces and geometry as for the shell simulation. The three solid models are shown in Fig. 3.8.
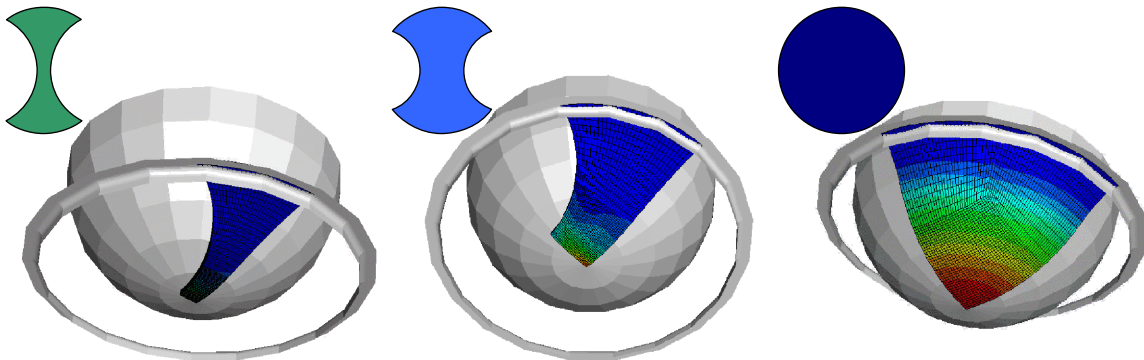
Figure 3.8: Quarter-symmetric solid FEA models of the three critical cases.

The force versus deflection curves for the three models is compared in Fig. 3.9 for the shell simulation, solid simulation, and for the experiment itself. It can be seen that the shell model agrees well with experiment in all cases, and the solid model compares well for the middle and equi-biaxial (full circle) cases. It is determined that the shell model is adequate for simulation of this scenario.
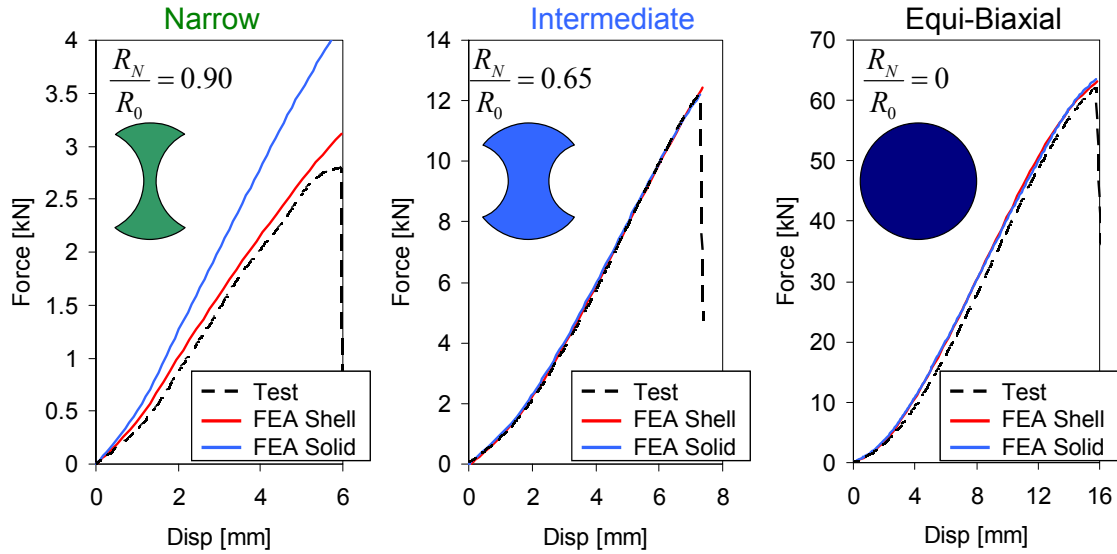
Figure 3.9: Force versus deflection curves comparing both shell and solid Finite Element models with experimental data.

In the prior analysis, both in DIC and the shell element, there was an implicit assumption that the bottom of the plate (furthest from the punch) represented the most critical surface. In the case of the DIC, this assumption was manifested by taking pictures of the bottom of the plate. In the case of the shell model, the assumption was manifested by using the integration point furthest from the punch. The assumption that the bottom of the plate is most critical can be evaluated with the solid element model. The effective plastic strain for all of the elements through the thickness of the plate is plotted against the punch displacement in Fig. 3.10. The bottom element is dark black. As can be seen in the figure, the bottom element exhibits the most strain throughout the travel of the punch up to a point close to fracture. In the case of the equi-biaxial case, the bottom element experiences the most strain throughout the entire experiment. In the case of the other two, when one of the other elements overtakes the bottom element close to the end of the experiment, it does not experience much more strain than the bottom element. As well, it should be noted that while the top of the plate is under higher hydrostatic pressure (lower stress triaxiality) because it is interacting with the punch while the bottom of the plate has no through-thickness stress. Therefore, it is believed that the assumption that the bottom of the plate is critical is a good engineering approximation.

67
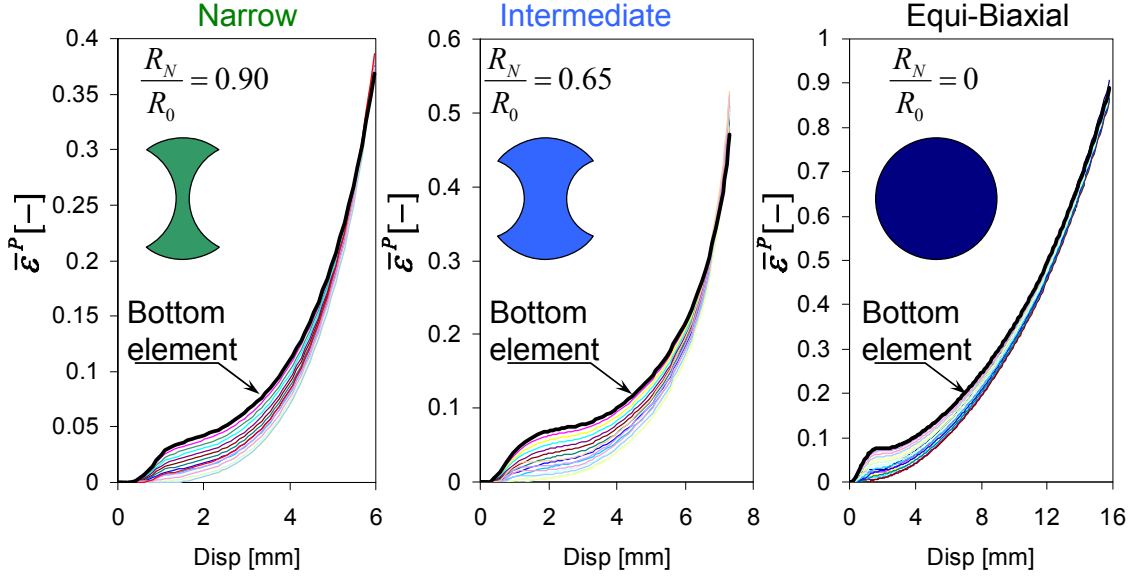
Figure 3.10: Time histories of effective plastic strain for all 16 elements through the thickness in the center of the specimen. The dark black line corresponds to the time history of the element on the die side of the plate, furthest from the punch.

3.7 Butterfly Experimental Setup

The butterfly test was first described by Mohr and Henn (2007) and subsequently modified by Bai (2008), who added a complex lofted surface cut into the center to assure that fracture always occurred at the same location. More results currently exist in the literature for Bai's geometry than Mohr and Henn's, so Bai's will be used for this study. The butterfly test was designed for fracture experiments in which it was subjected to combined tension and shear loading. The geometry of Bai's butterfly specimen is shown in Fig. 3.11. The most important geometric feature of the specimen is the complex geometry of the center, which was defined as a lofted surface consisting of arcs spaced 2 mm apart in the X direction in the specimen coordinates. The loft lines for this surface are shown in Fig. 3.11. Another way of representing this surface is by Eq. (3.18).

$$Z = \min\left\{ {t_{grips}}\Big/{2} , r + {t_{\min}}\Big/{2} + \sqrt{r^2 - Y^2} \right\} \tag{3.18}$$

where Z is the thickness coordinate, t_{grips} is the thickness of the grip section (the full thickness of the sheet metal in the current paper), $t_{\min}$ is the lowest thickness in the gage section (the middle), Y is the height coordinate, and r is the radius of the arc defining the loft lines, given in Eq. (3.19).

$$r = \left[\left(12.75 + 1.5 - \sqrt{12.75^2 - X^2} \right)^2 + 0.25 \right] [mm] \tag{3.19}$$

The center point of the arcs defining the loft lines is given in Eq. (3.20).

$$Z_{cp} = r + {t_{min}}\big/{2} \qquad (3.20)$$

The profile of the specimens was machined with a numerically controlled end mill. The gage section was machined with a hemispherical "ball-end" mill on a three-axis numerically controlled milling machine.
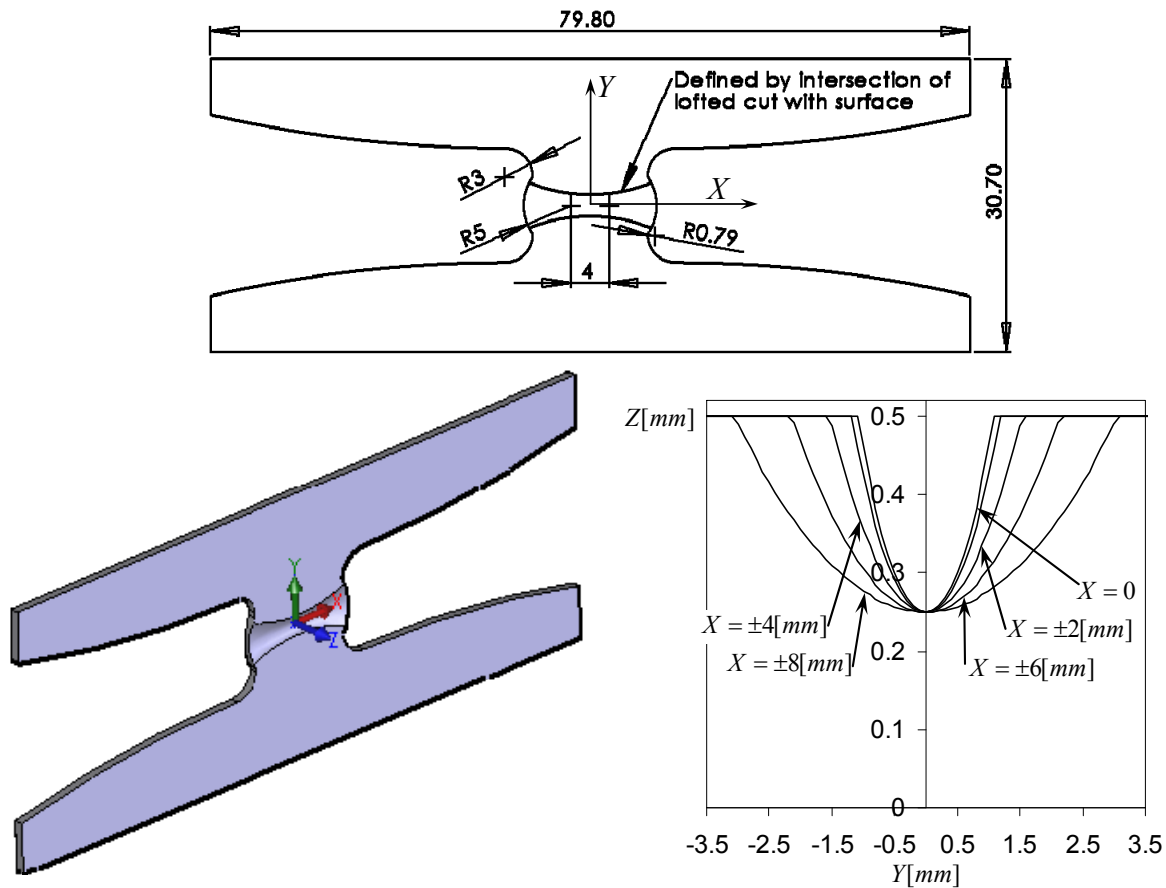
Figure 3.11: Geometry of the butterfly specimen with the coordinate system and origin indicated (top and bottom left) and the lofting lines defining the gage section (bottom right).

The specimens were tested on the dual-actuator testing machine shown in Fig. 3.12. The key feature of this machine is that it has two perpendicular actuators: one for shear (horizontal) motion and one for tension/compressions (vertical) motion. These two actuators can be moved independently in either force or displacement control. In analogy with the traditional Arcan apparatus, an angle β is defined in Eq. (3.21) which gives the ratio of the vertical force (or displacement) to the horizontal force (or displacement).

$$\beta \equiv \tan^{-1} \frac{F_V}{F_H} \quad , \qquad \beta \equiv \tan^{-1} \frac{U_V}{U_H} \qquad\qquad (3.21)$$

The forces were recorded by the horizontal load cell and the sum of the two vertical load cells. For all tests, the motion was recorded by a single camera and interpreted in planar motion by the VIC-2D software. Only displacements were desired for this experiment (as opposed to the state of strain at the fracture location), so the gage section was not painted. Because the area that was painted was not highly deformed during the experiment, white SAE fabric paint was first sprayed on, and the random speckle pattern was generated by black SAE fabric paint. The pictures were recorded as uncompressed .tif images that were 1300 pixels wide by 1030 pixels tall. This resulted in each pixel corresponding to approximately 0.0117 mm. The vertical and horizontal displacements were recorded by a virtual extensometer horizontally centered on the specimen with points at the top and the bottom. In addition, the rotation of the top and bottom of the specimen was measured by two virtual extensometers (top and bottom), which were arranged horizontally and centered on the specimen. Between the three virtual extensometers, the data was interpreted into four different signals: the vertical displacement of the top relative to the bottom, the horizontal displacement of the top relative to the bottom, the rotation of the bottom about a point centered on the bottom, and the rotation of the top about a point centered on the top. The six points (three extensometers) are indicated on a typical picture from the DIC system, shown in Fig. 3.13. In this study, nine conditions were measured: force control for -10, 0, 22.5, 45, 67.5, 90 degrees, and position control for 0, 45, 90 degrees. All conditions were performed with the rolling direction 0 and 90 degrees relative to the tensile axis. All conditions were performed twice to show reproducibility. The fractured force control specimens are shown in Fig. 3.14.
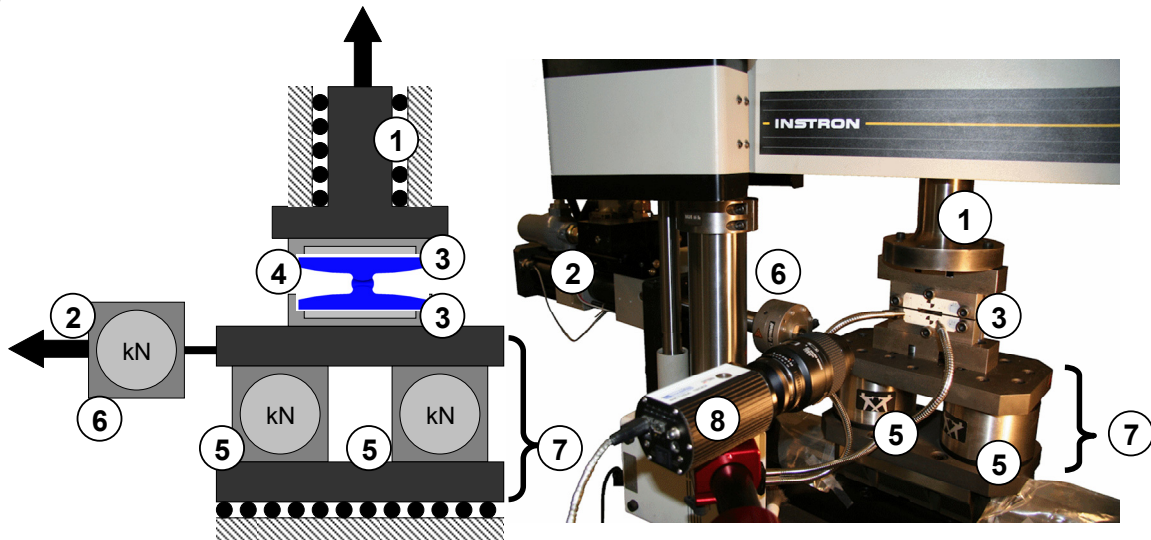
Figure 3.12: Biaxial testing machine in schematic form (left) and in physical form (right). Key components are vertical actuator (1), horizontal actuator (2), clamps (3), specimen (4), dual vertical load cells (5), horizontal load cell (6), sliding table assembly (7), and camera for DIC (8).
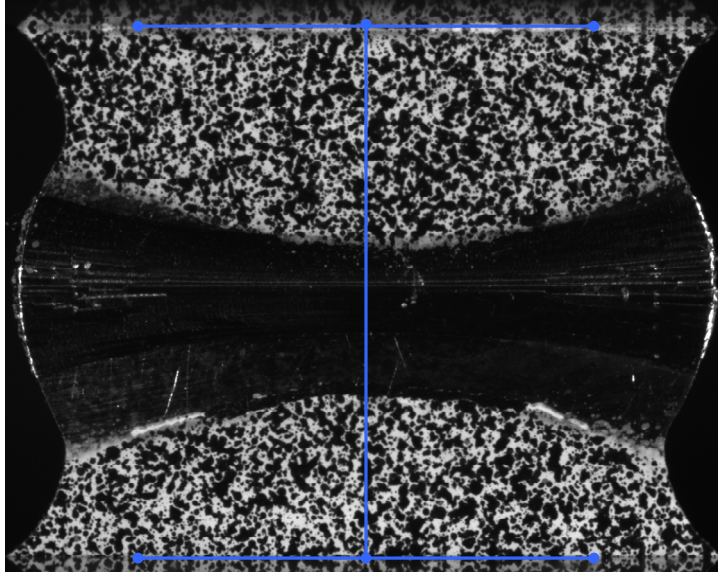
Figure 3.13: Characteristic picture taken from the DIC system with the locations of the tracked points indicated.
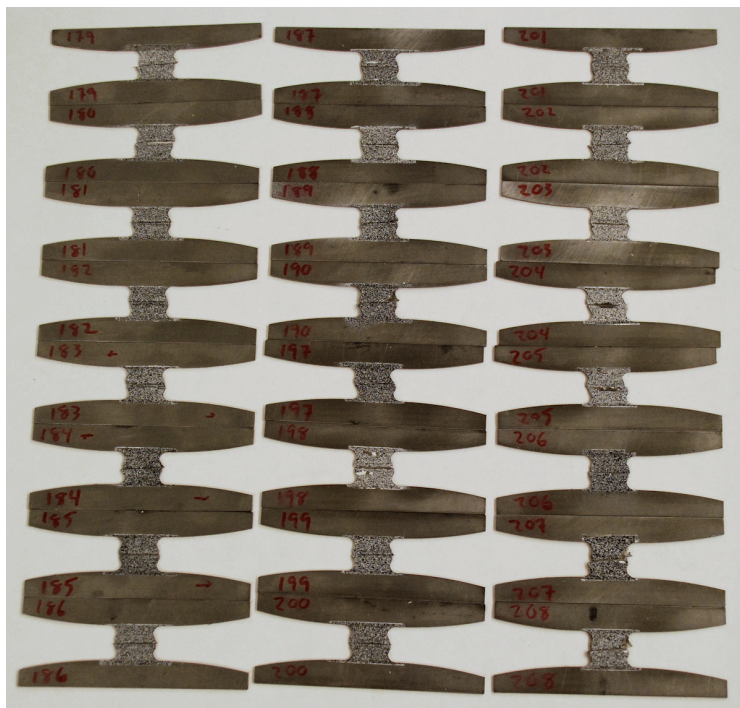
Figure 3.14: Butterfly specimens that have been tested to failure including double-redundancy of loading angles -10, 0, 22.5, 45, 67.5, and 90 degrees and specimens cut with the tensile axis 0 and 90 degrees relative to the rolling direction.

3.8 Analysis and Simulation of the Butterfly Experiments

Each experiment was simulated with an implicit Abaqus FEA model with a unique geometry and boundary conditions representative of the experiment. The mesh for a characteristic finite element model is shown in Fig. 3.15. The grip section was represented as a rigid body at the top and bottom of the mesh. The bottom rigid body was constrained not to translate, but to have a rotation about an axis parallel to the Z axis centered on the bottom of the specimen. The rotation of the Z axis was constrained to be the same as the rotation measured by the DIC system in the experiments. The rigid body on the top of the specimen was constrained to move in the X and Y direction according to the measurements by the DIC system. It was also constrained to rotate about an axis that was parallel to the Z axis but centered on the top of the specimen. This rotation was also given based on the measurements of the DIC system. These boundary conditions are also shown in Fig. 3.15. The plasticity model used for all simulations is the one given in Chapter 2.
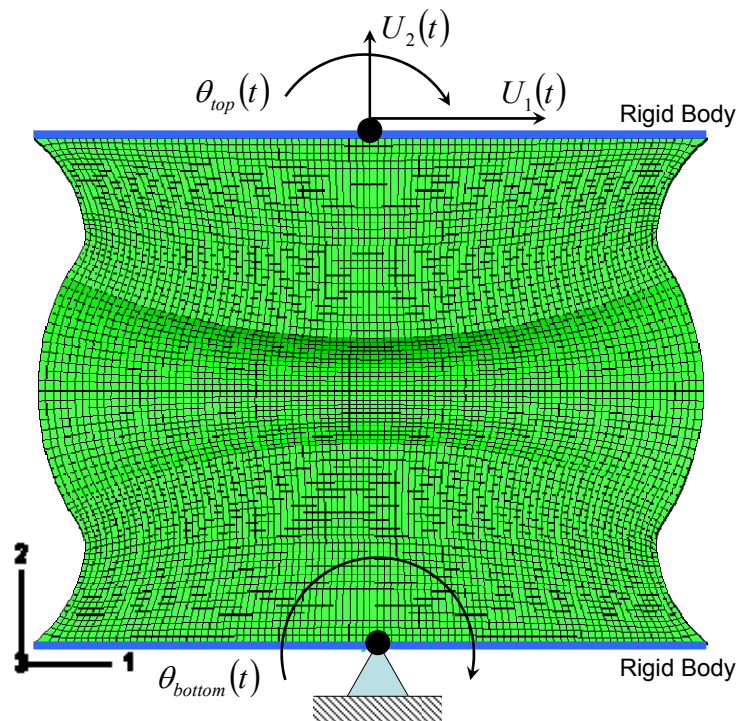
Figure 3.15: A characteristic finite element model used for analysis of the experiments. Note that only the section of the model visible to the DIC camera was modeled, and the boundary conditions on the top and bottom of the model were taken directly from DIC data.

For each specimen, the geometry of the FEA model was modified for four separate measurements: minimum thickness of the gage section, thickness of the grip section, width of the gage section, and height of the measured area. It was considered necessary to modify the geometry of each FEA model because the area of the specimens ranged from -9% of the average to 13% of the average due to manufacturing variability. This is to be expected because "good" tolerance in custom machining in the United States is considered to be 0.001 inches, which is 0.0254 mm. If this tolerance is taken on both sides of the specimen, then it is doubled and

accounts for 0.05 mm, which is 10% of the nominal thickness of the specimen. The gage section was measured before the experiments in three locations by point micrometers. The geometric representation of the lofted cut in FEA was then moved in or out of the thickness to achieve the average measured thickness. The lofted cut was not deformed or rotated in any way. This modeling assumption reflects the view that the largest inaccuracy would be in the positioning of the specimen in the milling machine and the determination of the vertical "zero" position by the machinist rather than by inaccuracies in the machine's control systems. The thickness of the grip section was measured once with point micrometers, and the geometric representation in FEA was assigned to this measurement. The width was measured with digital calipers. The radius that is 5 mm in Fig. 3.11 was increased or decreased to obtain the correct width. This choice in how to account for a non-nominal width reflects the view that errors in machining the profile were due to the cutter being a non-nominal diameter (by a very small amount) rather than errors in the control of the numerically-controlled machine that generated the profile. Finally, the height of the section that was modeled was taken as the initial height of the DIC virtual extensometer. Because the geometry of each of the simulations was slightly different, the mesh of each of them was different. However, the same software and input parameters were used for each mesh, and each geometry was approximately the same. Therefore, the meshes all had approximately the same edge lengths and aspect ratios. The centermost element of one sample case had a width (X length) of 0.1562 mm, a height (Y length) of 0.0801 mm, and a thickness (Z length) of 0.0805 mm. This can be compared to the model presented by Bai (2008), in which the smallest element was $0.15 \times 0.03 \times 0.08 mm$. The current mesh is considered superior to that of Bai's simulation because although it does not have the same very high resolution in the Y direction, it has better aspect ratio (the ratio L_{Max}/L_{min} is 5 for Bai and 2 for this model), and the resolution in the Y direction appears not to be necessary.

For each simulation, the effective plastic strain, pressure, 2nd invariant, and 3rd invariant were extracted from the centermost element of the FEA model (considered by Bai to be the critical element) and interpreted into stress triaxiality and Lode parameter and averaged as per the definitions given earlier in this paper. The point of fracture was considered in the experiments to be the time at which the force suddenly decreased, and it was at this point in the simulation that the effective plastic strain was taken for the fracture strain.

3.9 Comparison of Hasek experiments with Butterfly Experiments

The results of the Hasek (DIC interpretation) and butterfly experiments are shown in Fig. 3.16, as projected into the ductility versus stress triaxiality and ductility versus Lode parameter planes. At the initial viewing, they do not seem to agree. This can be largely blamed on the fact that the butterfly specimens experience a fully three dimensional state of stress whereas the Hasek specimens stay in a state of plane stress throughout the experiment, at least at the surface where the DIC measures them. Because the butterfly specimens break the plane stress assumption, they can not be compared in only two dimensions. Fig. 3.17 presents the 3-D comparison of the Hasek and butterfly specimens against a calibration of Eq. (3.1). As can be seen, most of the data points for both types of experiments agree very well with the fracture theory. A key difference between the calibrated fracture locus and the test points is that the Hasek test corresponding to the lowest stress triaxiality lies substantially below the surface.
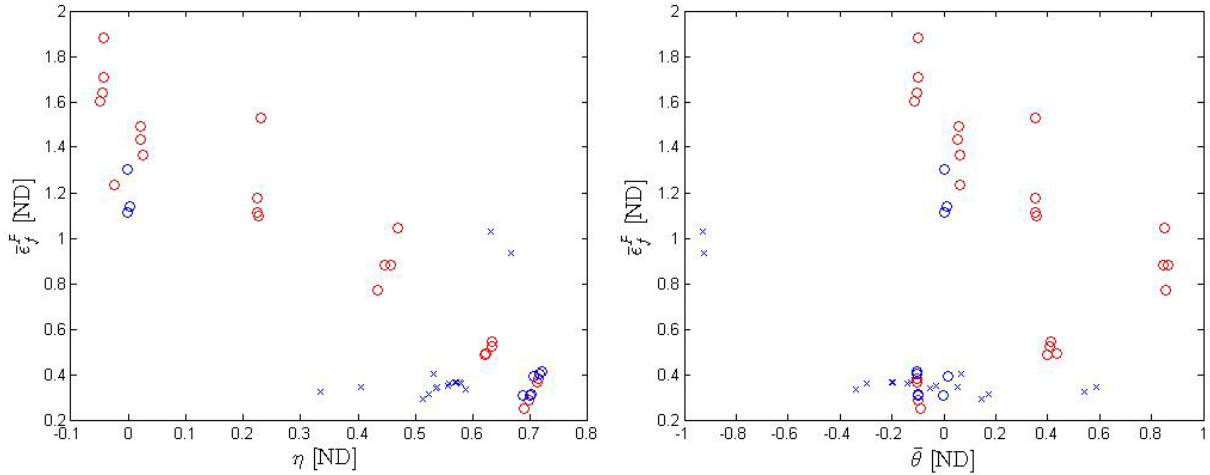
Figure 3.16: Projections of the measured fracture data onto ductility versus stress triaxiality (left) and ductility versus Lode parameter (right). The data points indicated with an "X" indicate Hasek tests; the data points indicated with red circles indicate butterfly tests run under displacement control; the data points indicated by blue circles indicate butterfly tests run under position control.
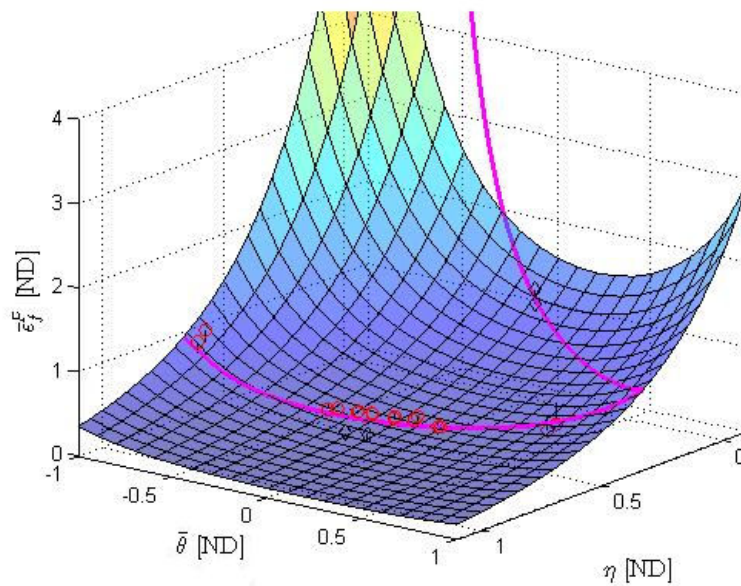
Figure 3.17: Calibrated Mohr-Coulomb fracture surface with key calibration points. The pink line indicates the plane stress assumption. Pink circles indicate Hasek data points, and diamonds indicate position control butterfly tests.

There is interest in knowing if the modified Mohr-Coulomb fracture locus can be calibrated only with tests like the Hasek test. It has been previously demonstrated that the butterfly tests provide enough data over a sufficient range that the Mohr-Coulomb fracture locus can be calibrated and effective over a wide range of strain rates (Bai, 2008). Therefore, the fracture locus was iteratively re-calibrated with various experiments removed to see what the minimum requirement of experimental data was to achieve a good calibration. Because all of the Hasek experiments

74

used specimens cut with the tensile axis perpendicular to the rolling direction, only butterfly specimens with the tensile axis perpendicular to the rolling direction were considered for this study. The fracture locus was then calibrated, and this condition is the condition with "All" experiments included in Table 3.2. Next, all butterfly experiments that used force control were excluded. This is because the specimen slightly softens after necking, and the testing machine collects very few points when running in force control mode while the force is decreasing. There was concern that the force control experiments may underestimate the ductility due to this effect. By comparing the "Hasek plus displacement control butterflies" condition with the "All" condition in Table 3.2, we can see that running the experiments in force control mode appeared to provide no large effect on the outcome. Next, the fracture locus was calculated with only Hasek experiments. As can be seen in Table 3.2, this provided unacceptably large errors in the calibration parameters, which leads to the conclusion that Hasek experiments alone can not calibrate the fracture locus. This effect can be seen geometrically in Fig. 3.17, where the Hasek experiments lie approximately in a line in the Lode parameter versus stress triaxiality plane, and they provide very little information about how the fracture locus surface should be oriented relative to that line, i.e. what the "pitch" of the surface should be relative to the Lode parameter axis. Next, to provide information on ductility that has a much lower stress triaxiality than the Hasek tests and is not on the same line that the Hasek tests are on, a butterfly experiment corresponding to pure shear was introduced with the Hasek experiments. This showed very good agreement with the calibration in which all experiments were included. Eliminating some Hasek tests to find the minimum necessary Hasek tests for calibration showed that only two Hasek tests (the one with the full diameter and the one with the deepest cutouts) plus a shear butterfly test are necessary for a successful fracture correlation. Based on this conclusion, the fracture locus is presented again in Fig. 3.18 with only the necessary experiments, both in its three-dimensional form and also as projected onto the stress triaxiality versus ductility plane.

Table 3.2: Parameters for the Mohr-Coulomb fracture model when different tests are excluded from the calibration.

c_1	c_2	c_3	$100\left(\dfrac{c_1}{(c_1)_{All}}-1\right)$	$100\left(\dfrac{c_2}{(c_2)_{All}}-1\right)$	Experiments included
0.191	738.8	1	0.%	0.%	All
0.195	728.8	1	2.%	-1.3%	Punch plus displacement control butterflies
0.214	740.	1	11.7%	0.2%	Punch
0.198	729.5	1	3.5%	-1.3%	Punch plus shear butterflies
0.195	729.1	1	2.1%	-1.3%	Three punch conditions plus shear butterflies
0.212	739.9	1	10.6%	0.1%	Three punch conditions
0.195	729.	1	1.8%	-1.3%	Two extreme punch conditions plus shear butterflies
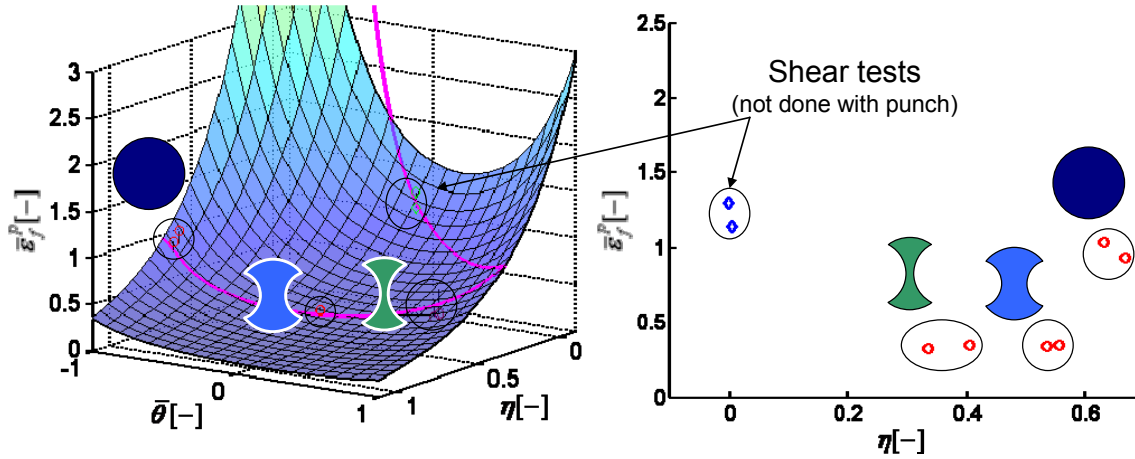
Figure 3.18: Two representations of the most critical fracture test data: full three-dimensional representation (left) and onto the ductility versus stress triaxiality plane (right).

3.10 Conclusions

A new procedure has been presented for the determination of ductility in terms of stress triaxiality and Lode parameter from sheet metal punching experiments.

These efforts have clearly shown that punching style experiments agree very well with butterfly experiments when compared in the full three-dimensional space of stress triaxiality, Lode parameter, and ductility. Moreover, it has been shown to be misleading to represent the fracture locus in only two dimensions. The Mohr-Coulomb fracture criterion has been shown to be applicable to Advanced High Strength Steels.

Another key outcome of this work is that punching style tests are not adequate in themselves to calibrate the Mohr-Coulomb fracture criteria. At least one point with a significantly lower stress triaxiality is highly recommended, and the condition of pure shear appears to fit the requirement very well.

Chapter 4

Assessment of Dynamic Plasticity

4.1 Abstract

A survey of data available in the literature has demonstrated that steels have shown a considerable variation in the effect of strain rate on plasticity, ranging from a 5% increase in flow strength at 500 s^{-1} to a 60% increase in flow strength at the same strain rate, depending on the material. A novel experimental technique is being developed at ICL in order to determine strain rate sensitivity of different sheet metals subjected to intermediate to high range of strain rates. This technique has been applied to DP780 steel at strain rates of the order of 300 to 500 s^{-1}, which is exactly the range of interest to the present thesis. The results show little or no effect of strain rate on plasticity. Finite element simulations of a series of dynamic punch experiments confirmed this finding by showing that it is not necessary to model the effect of strain rate on plasticity for this steel in this range of strain rates to achieve good correlation. While the material being used as an example for this thesis does not show a dependency of plasticity on strain rate, it is recommended that rigorous dynamic plasticity experiments be conducted to evaluate the effect of strain rate on plasticity for full generality.

4.2 Introduction

The effect of strain rate on plasticity for intermediate strain rates continues to be a subject that vexes researchers. For example, data from a large study that includes leading researchers in the field is presented in Fig. 4.1. As part of this study, Yan and Urban (2003) and their collaborators measured the stress versus strain curve of same material (TRIP600-CR) with three different force measurement methods. Data from a traditional load cell provided very wavy results. Split Hopkinson Bar (SHB) data proved somewhat more favorable, but it was noisy and ended prematurely due to the limited pulse duration possible on the researchers' equipment. A third method, in which the dogbone specimen is manufactured with an unusually long grip section and a strain gage is mounted in the grip section to measure forces, is shown in the plot. While these three methods give reasonably good correlation with each other, all three curves have much to be desired. A typical method of working with these results is to fit an analytical function to the plasticity part of the curve and then use the fitted results to represent the plasticity of the data. Based on the differences between a quasi-static stress-strain curve and a dynamic stress strain curve, a yield stress ratio, *R*, is defined in Eq. (4.1).

$$R\left(\dot{\bar{\varepsilon}}^{p}\right) \equiv \frac{\sigma_{y}^{High\dot{\bar{\varepsilon}}}}{\sigma_{y}^{Static}} \qquad (4.1)$$

The existence of such a parameter implies a decomposition of an equivalent stress into two major terms, as shown in Eq. (4.2): one term σ^0 to define the hardening curve, and one (R) to determine the effect of strain rate on fracture.

$$\bar{\sigma} = \sigma^0\left(\bar{\varepsilon}^{p}\right)R\left(\dot{\bar{\varepsilon}}^{p}\right) \qquad (4.2)$$

Cowper and Symonds (1958) proposed one such yield stress ratio (R), which is defined in Eq. (4.3).

$$R\left(\dot{\bar{\varepsilon}}^{p}\right) \equiv \frac{\bar{\sigma}}{\sigma^0} = 1 + \left(\frac{\dot{\varepsilon}}{\dot{\varepsilon}_0}\right)^{1/n_{CS}} \qquad (4.3)$$

Based on results like those of Fig. 4.1 and the decompositions given above, plots like 4.2 are compiled, showing a scaling factor for the yield stress to account for the effect of strain rate. Note that all of the curves shown in Fig. 4.2 are for steel. These results show that a meaningful effect of strain rate on plasticity should be expected for most experiments performed on steel.
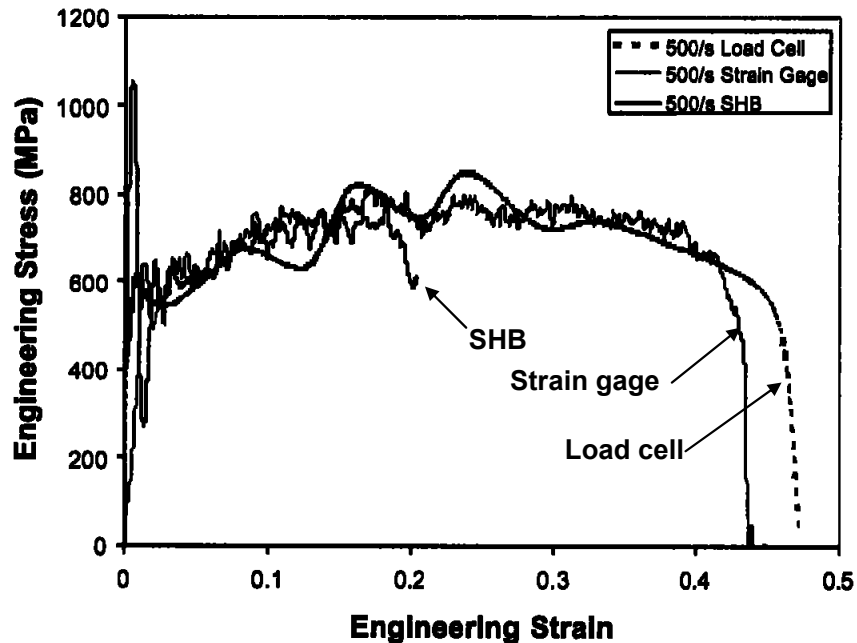
Figure 4.1: Sample stress versus strain curves determined for TRIP600-CR at 500 s^{-1} with different measurement technologies. The "load cell" indicates the measurement from a conventional load cell. "Strain gage" indicates the force measurement made by a strain gage mounted on an extended grip section. "SHB" indicates measurements made by split Hopkinson bar. After Yan and Urban (2003).
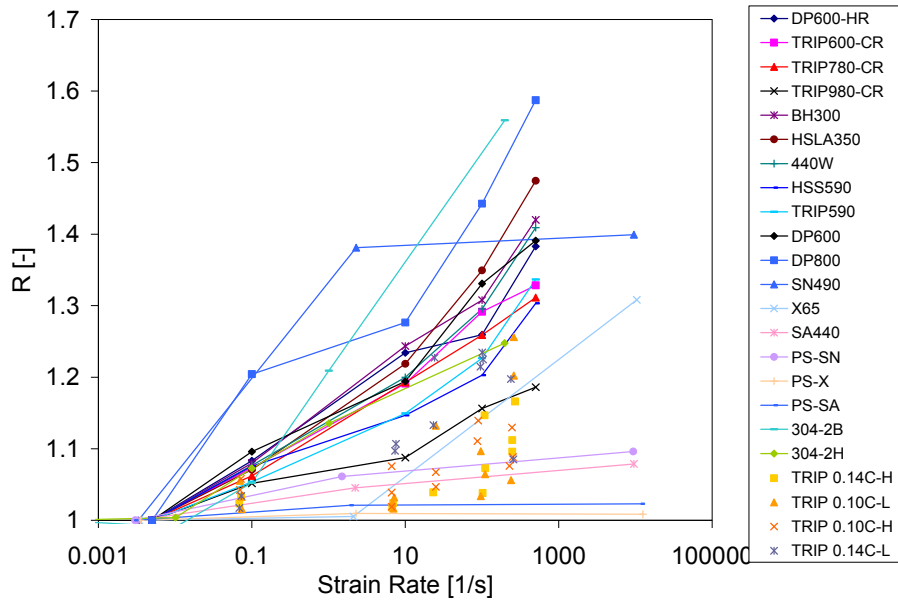
Figure 4.2: The effect of strain rate on yield strength for a variety of automotive sheet steels. Data from Choi et. al. (2002), Lee and Wang (2007), Qiu et. al. (1999), Talonen et. al. (2005), and Yan and Urban (2003).

4.3 Dynamic Shear Experiments

A device for plasticity testing in shear for both static and dynamic conditions is being developed by Bordier (2009) of the Impact and Crashworthiness Lab at MIT. Pictures of the shear specimen and corresponding fixture are shown in Fig. 4.3. In the static case, the deformation of the specimen in the provided windows was recorded with a QImaging Retiga 1300i camera. For the dynamic case, the deformation was recorded with a Phantom 7.1 high-speed camera. Displacements within the gage section were measured with DIC-2D by Correlated Solutions, Inc., and the displacments were converted into equivalent plastic strain through Hill's formulas, which are detailed in Chapter 2. Bordier (2009) tested the DP780 sheets in static (10^{-3} s^{-1}) and dynamic (305 and 564 s^{-1}), and the measured stress-strain curves are shown in Fig. 4.4. The strain rate histories of the dynamic curves from Fig. 4.4 are given in Fig. 4.5.

This type of experiment has the limitation that a mass associated with gripping must be accelerated to the speed of the drop mass over a very short period of time, resulting in longitudinal waves in the force sensor, which appear in the measurements as force oscillations, which translates into oscillations in the stress signal. The mass of the part of the grips that is subject to such accelerations has been minimized; however, it must be finite to properly grip the specimen and prevent buckling. With these limitations in mind, the dynamic curves determined by Bordier (2009) show very little change relative to the static conditions measured by Bordier (2009) or the model developed in Chapter 2 (listed as "Model" in the figure). This indicates that for this range of strain rates, it is not necessary to model the effect of strain rate on plasticity.
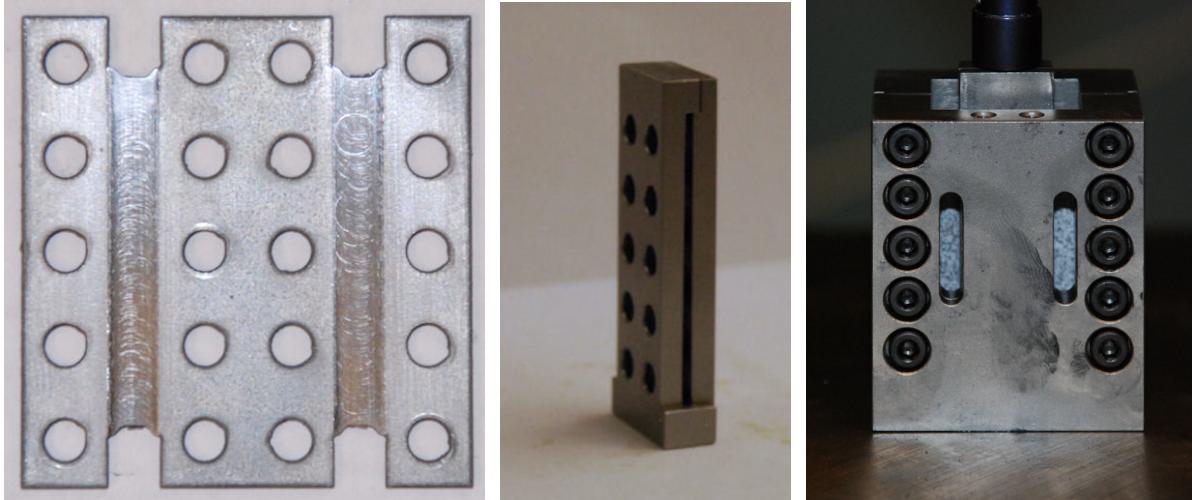
Figure 4.3: Fixture and double shear specimen for a dynamic shear test. The specimen (left) is secured by a very thin clamp in the center (center) and on the outside by a larger fixture (right). The larger fixture acts as the ground while the center fixture transmits an impact load through the center of the specimen and prevents buckling. Photos courtesy of Bordier (2009).
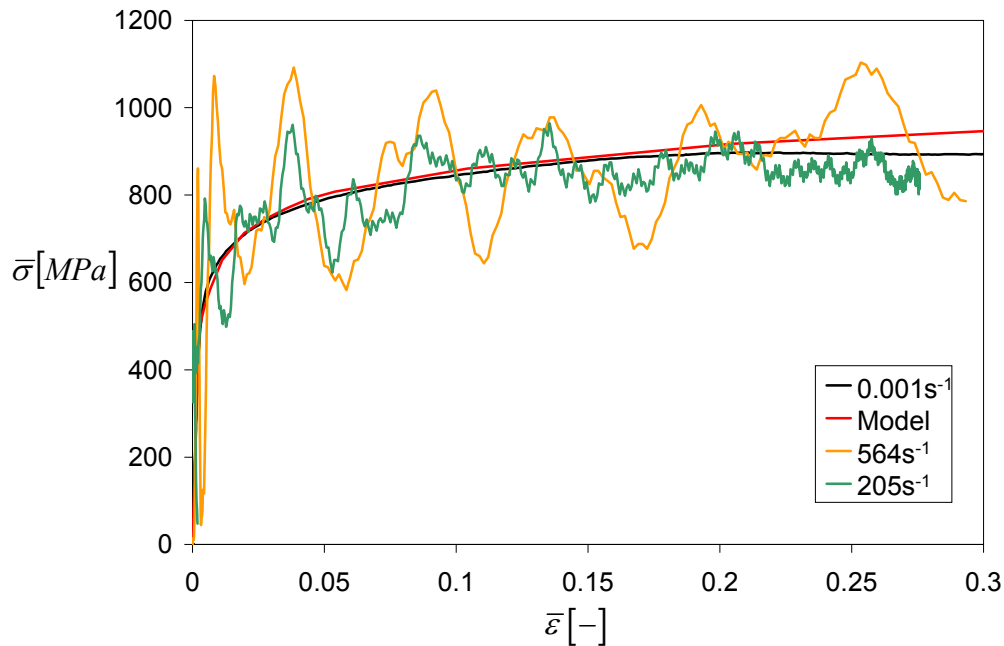
Figure 4.4: Equivalent stress versus equivalent strain curves determined from static and dynamic experiments conducted in the new apparatus, showing very little effect of strain rate on the hardening curves. The waviness of the curves is attributable to the dynamics of the experiments. Data courtesy of Bordier (2009).
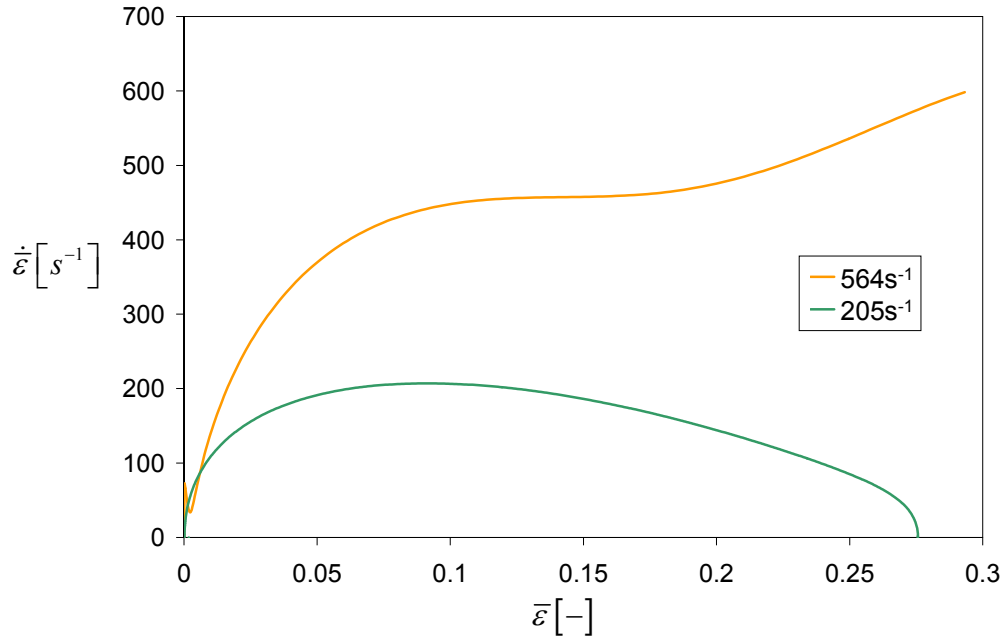
Figure 4.5: History of strain rate through one of the dynamic double shear experiments.

4.4 Parametric Assessment of Strain Rate Effect

The data for DP800 from an unknown steel supplier was published by Yan and Xu (2003). This data is shown as dark dots in Fig. 4.6 and fitted with the Cowper-Symonds plasticity law. The constants for this fitting are $\dot{\varepsilon}_0 = 12217 s^{-1}$ and $n_{CS} = 3.33$. The original data is plotted as black dots in Fig. 4.6, and the curve fit through the points is labeled 23% in Fig. 4.6 because it corresponds to a 23% increase in yield strength at a strain rate of 100 s^{-1}. For the purpose of a parametric study, a family of curves is generated by retaining the same n_{CS} and adjusting $\dot{\varepsilon}_0$ such that values of 2.5%, 5%, and 10% increase are experienced at a strain rate of 100 s^{-1}.
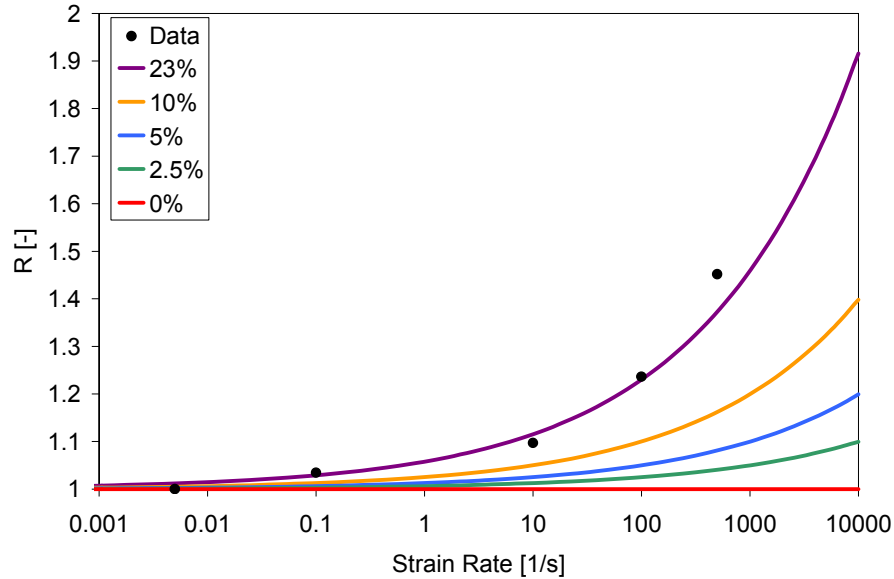
Figure 4.6: The effect of strain rate on yield strength for DP800, compared with a Cowper-Symonds fit. A family of curves is also plotted that will be used in a parametric study to assess the effect of strain rate effects on deformation. Note that the curve titles (e.g. 23%) relate to the increase in yield strength at 100 s^{-1}.

A series of experiments were run in which plates with various cutouts were clamped into a circular die and punched out of plane by a hemisphere attached to a falling mass. These experiments were essentially dynamic versions of the experiments described in Chapter 3, except that only force time histories were recorded. The dynamic experiments will be developed more fully in Chapter 5, in which they are used for fracture testing.

This family of Cowper-Symonds relationships are applied to explicit finite element models of the experiments, and the results are compared with the test data in Fig. 4.7. More details of the finite element model can be found in Chapter 5. Comparison of the simulation with the experiments shows that the simulations that correlate best with experiments are the ones that have a strain rate independent material model.
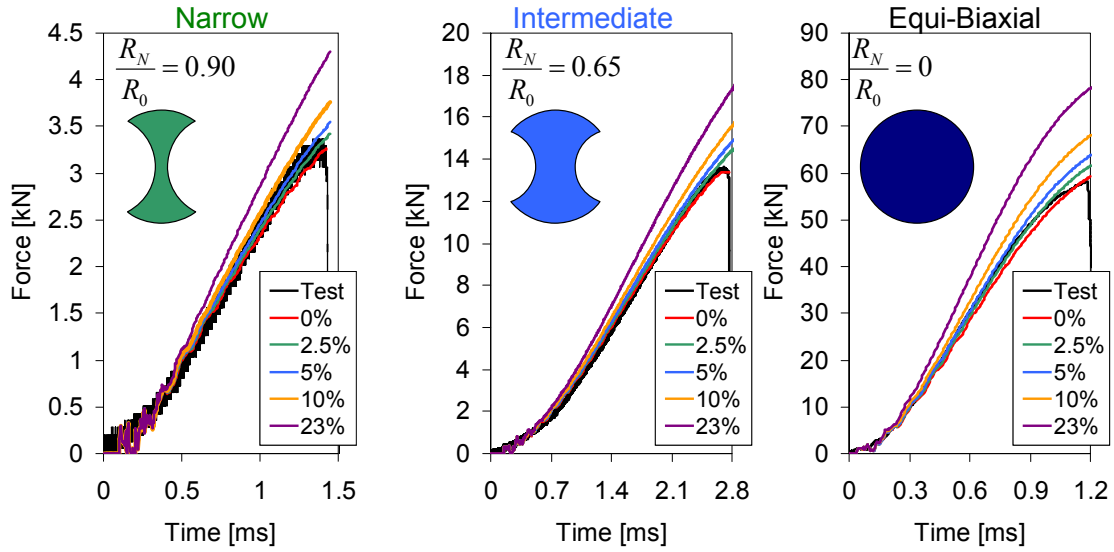
Highest Strain Rates = 443-782 s^{-1}
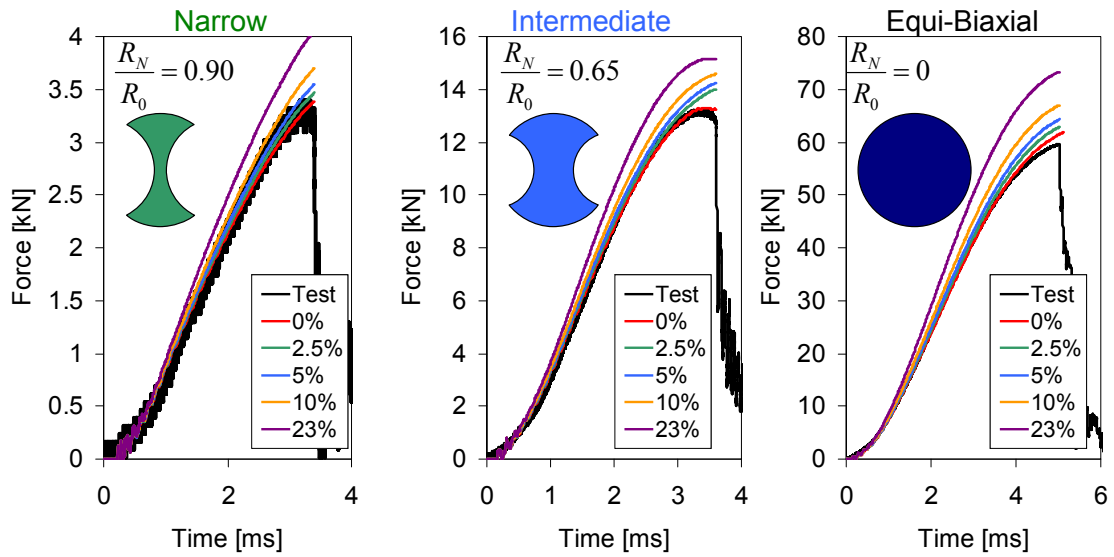
Middle Strain Rates = 164-309 s^{-1}

Figure 4.7: Comparison of test data with simulations of the same test with different contributions of strain rate on plasticity. The strain rate independent model (0%) appears to deliver the best results.

4.5 Discussion

In light of the above developments, it will be of interest to better understand what strain rates are experienced by the specimen during a typical experiment. Therefore, the strain rate was studied for the dynamic experiment in which a circular plate was impacted with an initial velocity of 13.93 m/s and a mass of 7.27 kg, corresponding to a strain rate for the center element (averaged with respect to plastic strain) of 782 s^{-1}. The effective plastic strain for a ray of elements extending from the center of the plate to the edge was exported for analysis. The studied elements are highlighted in Fig. 4.8. The strains were then numerically differentiated with respect to time by the finite difference method to obtain the strain rate. The radial distribution of strain rates is shown in Fig. 4.9 for three different times in the simulations.
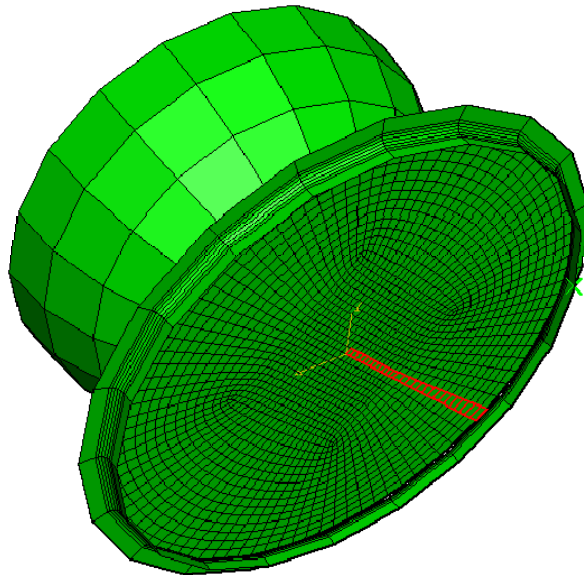
Figure 4.8: Finite element model of equi-biaxial experiment with the elements used for averaging highlighted in red.
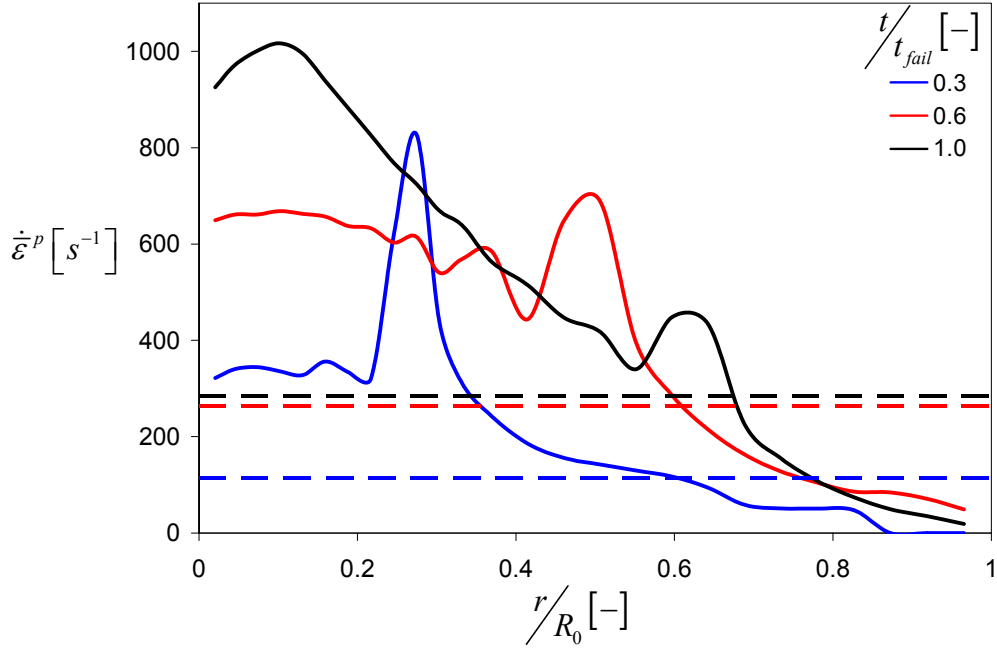
Figure 4.9: Strain rate distribution over the radius for three different time points in the simulation. The solid lines represent the spatial distribution while the dashed lines represent the spatial average.

The spatial average of strain rate was evaluated for all of the times of the simulation according to Eq. (4.4).

$$\dot{\bar{\varepsilon}}_{SpAvg}^{p} = \frac{2}{R_0^2} \int_0^{R_0} \dot{\bar{\varepsilon}}^p r \, dr \tag{4.4}$$

This spatial average is shown graphically as dashed lines in Fig. 4.9. It is interesting that the spatial averages shown in Fig. 4.9 are counter-intuitively low, and this is because the averaging in polar coordinates weights points furthest from the center stronger than those close to the center. The spatial average is compared against the strain rate of the center element in Fig. 4.10. In that figure, it can be seen that due to the low strain rate contributions of the elements at the periphery, the average strain rate is approximately one third that for the center element. The temporal average is then taken of the spatial average, according to Eq. (4.5).

$$\dot{\bar{\varepsilon}}_{TAvg}^{p} = \frac{1}{t_f} \int_0^{t_f} \dot{\bar{\varepsilon}}_{SpAvg}^{p} \, dt \tag{4.5}$$

The resulting temporal spatial average of the whole specimen for the duration of the experiment was $\dot{\bar{\varepsilon}}_{TAvg}^{p} = 188 \left[s^{-1} \right]$.
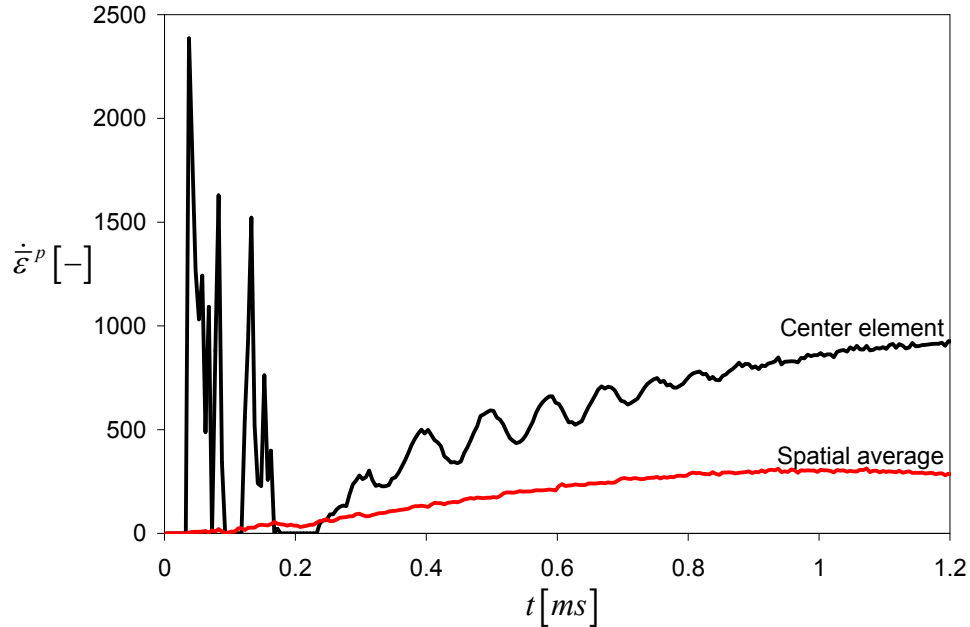
Figure 4.10: Strain rate history of the centermost element and the spatial average.

The same parametric study with the Cowper-Symonds models shown in Fig. 4.6 was evaluated for the spatial average strain rate. A comparison of the strain rate history and the spatially averaged strain rate history for simulations with all five material models is shown in Fig. 4.11. In this plot, the spatially averaged strain rates are indistinguishable from each other. The strain rates of the center element are close, but not as close as the spatially averaged strain rates. The importance of the difference between the various material models was evaluated by evaluating the temporal spatial average for each of them and plotting them as a function of the material law in Fig. 4.12. This curve has a very low slope, with the difference between the most and least strain rate sensitive model being only 7% of the temporal spatial average strain rate.
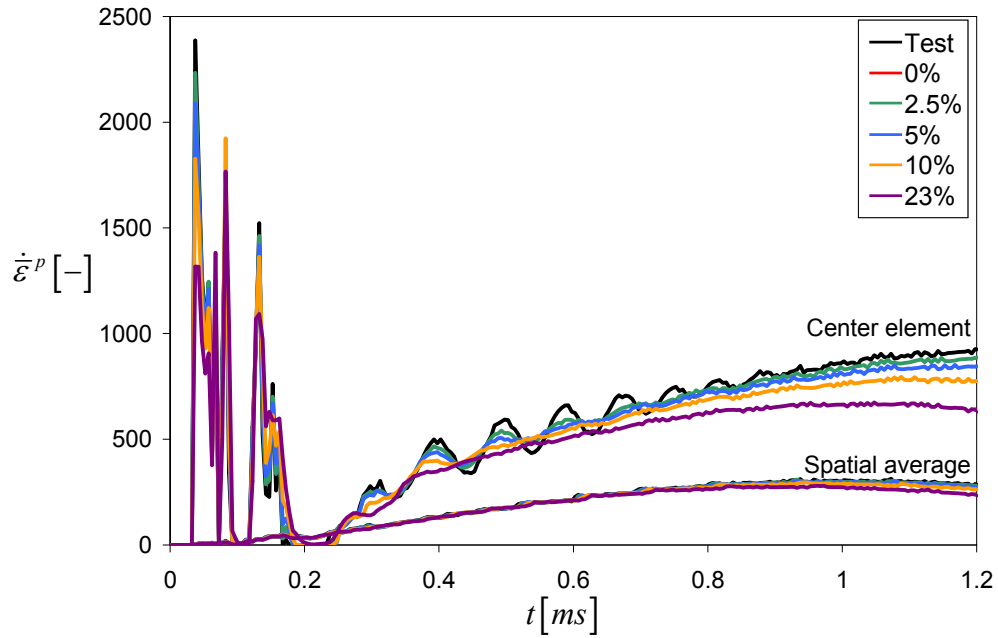
Figure 4.11: Strain rate history of the centermost element and the spatial average as compared to a family of similar simulations with varying effects of strain rate on plasticity.
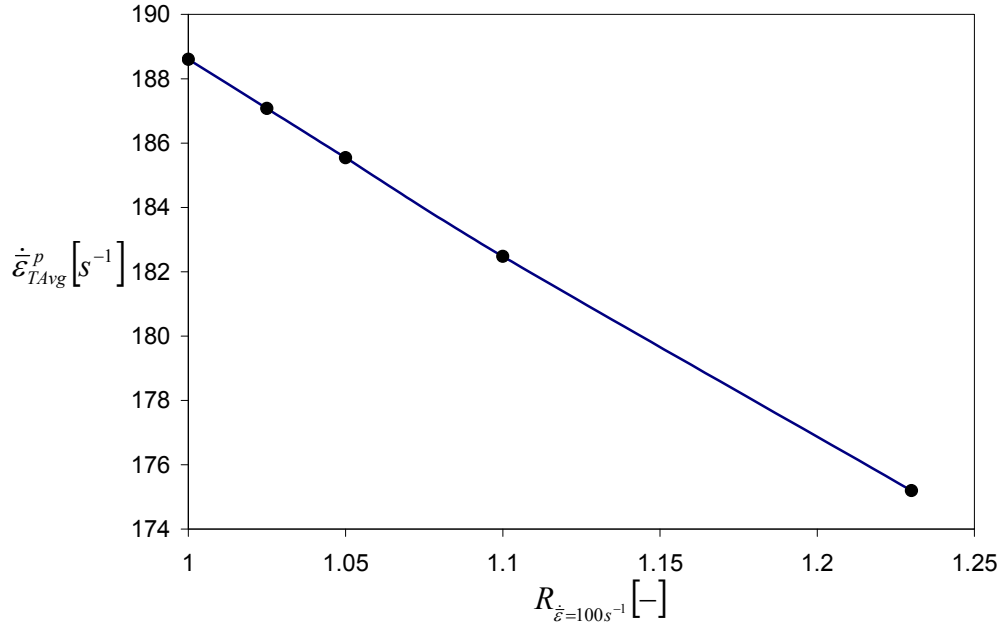
Figure 4.12: Temporal spatial average of strain rate for five different simulations, each with a different strain rate sensitive plasticity model. The plasticity models are the same as those summarized in Fig. 4.4, and they are denoted by their R value at 100s⁻¹.

4.6 Conclusions

The steel being examined in this thesis is anomalous in that it does not show strain rate sensitivity well into the intermediate range. This finding has been demonstrated both directly through dynamic shear tests and indirectly through a parametric study. However, a review of the literature pertaining to the effect of strain rate on plasticity shows that this effect must be accounted for in the general case. While it is reasonable to proceed with modeling the sample steel with strain rate insensitive parameters even for the dynamic cases, it is advisable in general to rigorously calibrate the effect of strain rate on plasticity for steels. The new technique described in this chapter can be used for that purpose.

Chapter 5

Characterization of Dynamic Fracture

5.1 Abstract

A new methodology is developed that will allow for the determination of failure parameters over a range of stress triaxialities from 0.4 to 0.67 and a range of strain rates from quasi-static through intermediate (up to 800 /s in this study). The chosen material presented a very complex relationship between material ductility, stress triaxiality, and strain rate. The presented methodology is based on a method for quasi-static failure testing of thin sheets first presented by Hasek (1978). In this method, specimens with different arced side cutouts are clamped into a circular die and subjected to lateral punching by a hemispherical punch. Through membrane stretching of the specimens, the material is tested to fracture through a variety of stress states. This experimental method is analyzed by means of the inverse method, and then extended into the strain rate dimension through instrumented drop tower Hasek experiments. Strain rate and strain rate history are controlled in the drop tower experiments by variation of the drop velocity, mass, and test geometry.

5.2 Introduction

The history of ductile fracture, including some recent attempts to assess the affect of strain rate on fracture, was introduced in Chapter 1. It was shown in Chapter 1 that even recent attempts to determine the effect of strain rate on fracture resulted in some ambiguous results, and nobody has quantified the effect of stress triaxiality, Lode angle, and strain rate on fracture.

Punching methods popular in the sheet metal forming industry were also introduced in Chapter 1. A particular punching method (the Hasek method) that features membrane loading of a specimen with cutouts was demonstrated and favorably compared with a different fracture method in Chapter 3. One of the key conclusions from Chapter 3 was also that the Hasek experiments were highly redundant, and that only two or three of them are truly relevant.

It is from this context of an existing static fracture envelope from prior chapters along with ambiguous prior results that the current chapter begins.

5.3 Dynamic Hasek Experiments

The dynamic experiments were conducted in an Instron Dynatup 9250HV drop tower. This drop tower is equipped with springs so that the drop mass can accelerate faster than gravity. Because of the spring assist, the drop speed depends on the drop mass. The maximum velocity for the drop tower is 14 m/s for its lightest mass (7.11 kg) and 6 m/s for its heaviest mass (85 kg). The drop tower is also equipped with a tup, which is a strain gage-based force sensor mounted on the bottom of the drop mass. The machine measures velocity immediately prior to impact with a velocity flag. Because the mass and initial velocity are known and the measured force is assumed to act on the bottom of the mass, the displacement can be estimated from double integration of Newton's second law. However, this method is only an approximation because small measurement errors in the measurement of force accumulate quickly when numerically integrated.

The same die and punch were used as with the static portion of this study. The contact between the punch and the specimen was lubricated as it was in the static case, with five layers of 0.05 mm thick Teflon and layers of metal-free anti-seizing lubricant between each layer. Fig. 5.1 gives an overview of the important drop tower components and experimental setup. The tested conditions are listed in Table 5.1. All data for the dynamic portion of this study was collected with an analog low-pass pre-filter of 100 kHz (the highest available frequency) before being digitized. Data sampling rates ranged from 2.05 MHz to 546 kHz, depending on the condition that was being run.
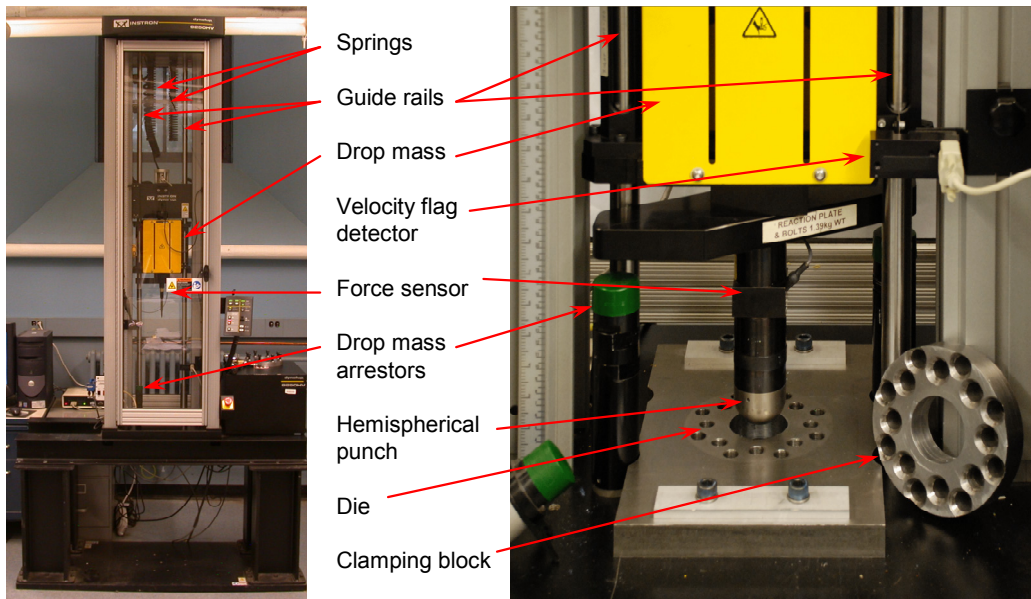
Figure 5.1: Experimental setup for the dynamic Hasek tests. The die and hemispherical punch were the same as those used in the static case.

Table 5.1: Test conditions used for calibration of dynamic fracture locus

	$R_N/R_0\,[-]$	$V_0\,[m/s]$	$M\,[kg]$	$\dot{\bar{\varepsilon}}\,[s^{-1}]$
Quasi-Static	0.45	0.000025	--	0.0024
Quasi-Static	0.33	0.000025	--	0.0028
Quasi-Static	0	0.000025	--	0.002
Mid	0.45	2.25	7.72	164
Mid	0.33	3.11	11.06	309
Mid	0	3.67	85.06	215
High	0.45	4.94	7.36	443
High	0.33	3.25	30.47	631
High	0	13.93	7.27	782

Table 5.1 shows that a different mass and velocity combination was used for every single case. This choice was driven by an attempt to accomplish approximately the same average strain rate and strain rate history for each of the experiments. Use of the same drop mass and impact velocity for the specimens with different cutouts would result in different strain rate histories and therefore make it more difficult to compare between cases. For example, the strain rate history for each of the three cutout geometries given an impact velocity of 14 m/s and a mass of 7.11 kg is shown in Fig. 5.2. Not only do these histories provide results that are difficult to compare with one another, but the very high strain rates experienced by the middle case cause ambiguities when attempting to locate the time of fracture and the corresponding state of stress and strain. Because the strain rates of the high speed equi-biaxial case could not be increased without changes to the geometry (e.g die radius) or drop tower (e.g. higher maximum speed), it was decided to keep the equi-biaxial cases and optimize the other two cases to agree with the equi-biaxial cases. An additional benefit is that the equi-biaxial case appears to have experienced a strain rate that is the most constant among all of the cases. Therefore, the cases were optimized through iterative simulations (optimizing mass and velocity combinations) to match the other two cases as closely as possible for the history of the curves in the effective plastic strain rate versus effective plastic strain coordinate system. The results are shown in Fig. 5.3. The choice to operate in the space of effective plastic strain rate versus effective plastic strain comes from the fact that stress triaxiality and Lode angle have historically been averaged with respect to effective plastic strain, so the strain rate would be evaluated in a similar way. Therefore, optimizing in this space (as opposed to, for example, effective plastic strain rate versus time) would produce average strain rates that are closest for all three cases.

It can be seen in Fig. 5.2 that the case with the intermediate cutouts had the highest strain rate. This is counterintuitive because this case was geometrically in between the case with the biggest cutouts and the case with no cutouts at all. It can be seen in Fig. 5.3 that when the impact velocity for the intermediate case is reduced to have approximately the same strain rate as the equi-biaxial case that it features a transition from lower strain rates to higher strain rates at an effective plastic strain of approximately 0.4. Both of these phenomena are easily explained with the same physical understanding. While the narrowest specimen (the one with the deepest cutouts) and the equi-biaxial case tend not to localize, the middle case tends to localize its strain in a narrow strip right across the center. This localization can be seen as an in-plane phenomenon (unlike necking) that is due to the deformation being concentrated because of the shape of the cutouts. The higher strain rate in Fig. 5.2 is attributed to the fact that the strain rate is measured at the center, where the strain has localized. The transition seen in Fig. 5.3 is due to

91

the localization, where the lower strain rate corresponds to uniform straining and the higher strain rate corresponds to the strain rate after localization in the necked region. For these reasons, this transition feature is unavoidable for the intermediate geometry, and this geometry should be avoided if possible.

Examples of tested specimens from multiple strain rates and with all three cutout geometries are shown in Fig. 5.4.
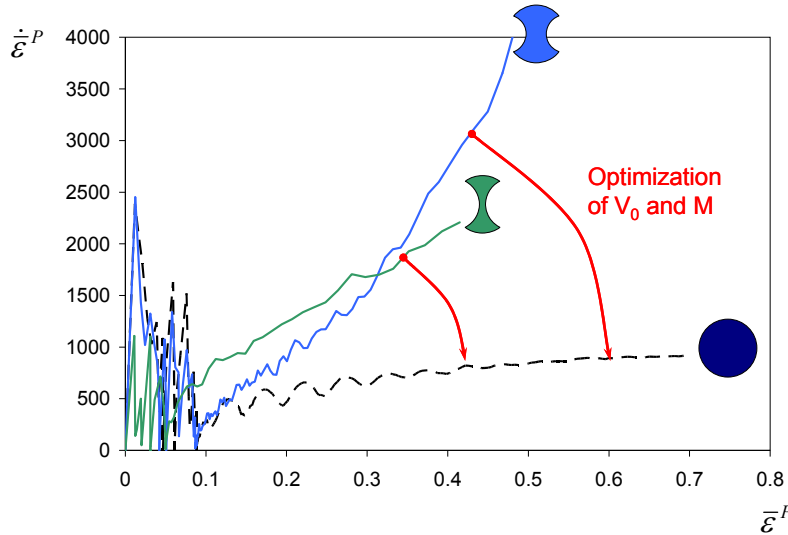
Figure 5.2: *The strain rate histories achieved when all three geometries are tested with the same impact velocity and mass, in this case a mass of 7.11 kg and a velocity of 14 m/s.*
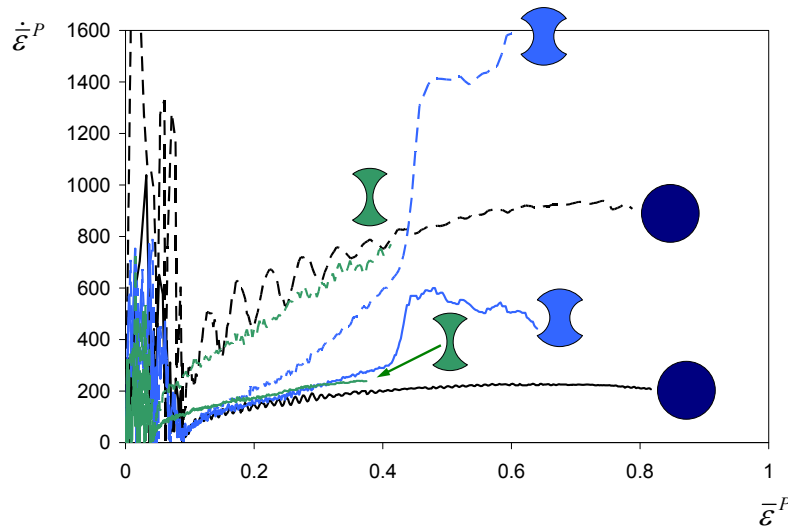
Figure 5.3: *The strain rate histories for two sets of three experiments with approximately equal average strain rates. Notice that while the equi-biaxial case and the narrowest case tend not to localize, the middle case tends to localize, producing a shift from lower strain rates to higher strain rates at a plastic strain of approximately 0.4.*
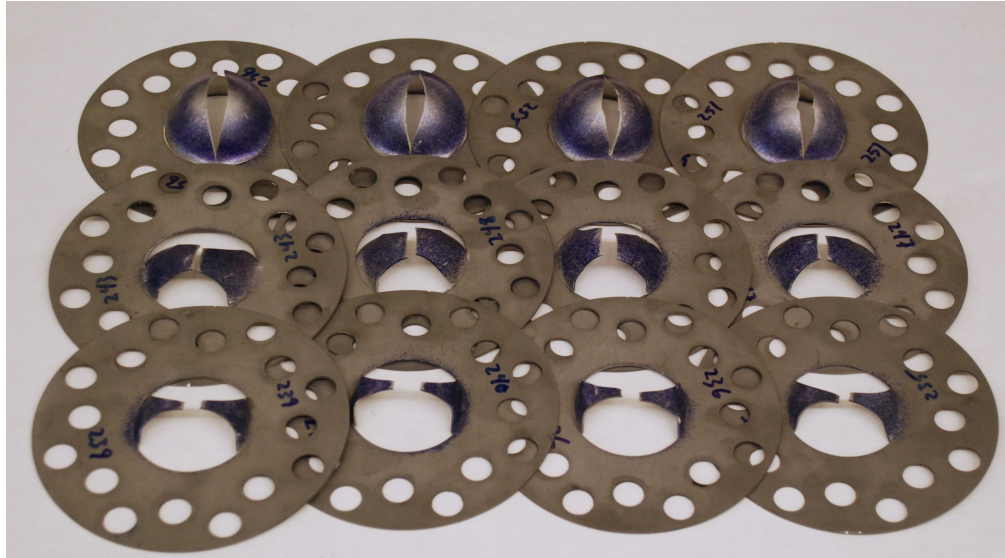
Figure 5.4: Twelve dynamic tests consisting of two tests each for three different geometries and two different combinations of mass and impact velocity. Note that all of the specimens shown have been bent back into form for DIC analysis, though the area immediately around the fracture was not strained after the test.

5.4 Analysis and Simulation of the Experiments

The longest duration of the dynamic experiments was less than 5 ms, so the available cameras were not able to capture any pictures during the test for DIC purposes. Therefore, the dynamic experiments were not able to be analyzed in the same method that was presented for the static cases. Instead, finite element models were created for all models (static and dynamic) and run. The static models were presented in Chapter 3 and were solved with an implicit solution scheme. While the rigid punch and die geometry were identical to that of the static cases, the geometry of each specimen was modified to match the dimensions measured for the specimens. The dynamic experiments were simulated with an explicit finite element solver because of its dynamic nature. Also, this set of experiments was simulated by assigning a mass and initial velocity representative of the drop mass to the impacting hemispherical punch. Because the displacement measurement of the drop tower is considered only to be an estimate for reasons mentioned before, correlation was done for force versus time curves rather than force versus displacement. A sample finite element model of one of the dynamic cases is presented in Fig. 5.5. The material model used for the simulations is described in Chapter 2. The correlation between experiment and the finite element simulation of each experiment is given in Fig. 5.6 for the dynamic cases. Overall, the correlation between the simulations and the experiments was exceptional, leading to confidence that the simulations could be used to interpret the experimental results.

The punch and die are shown in gray, represented as analytical rigid geometry.

The specimen was represented as shell elements.
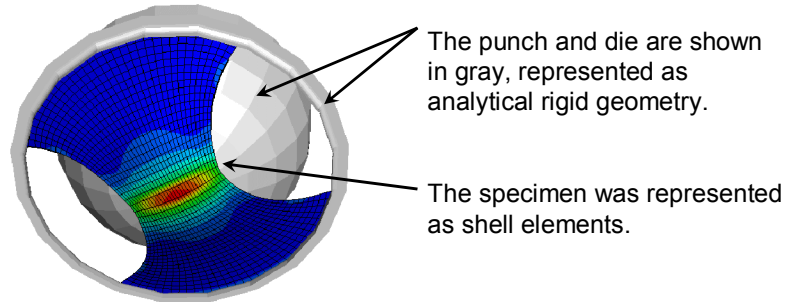
Figure 5.5: Finite element model of the experiment, showing the specimen along with the analytical rigid die and punch. Note that the faceting on the analytical rigid surfaces is only for display.
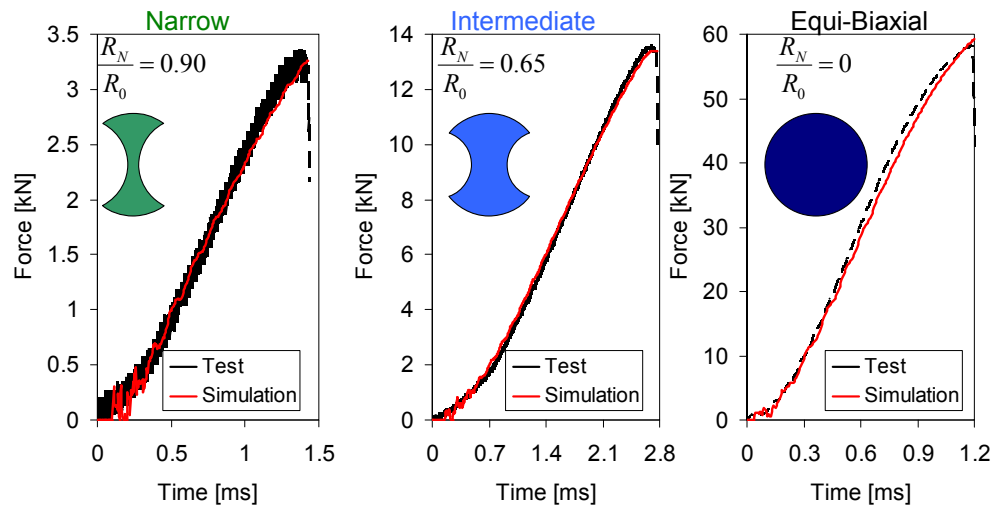
Highest Strain Rates = 443-782 /s
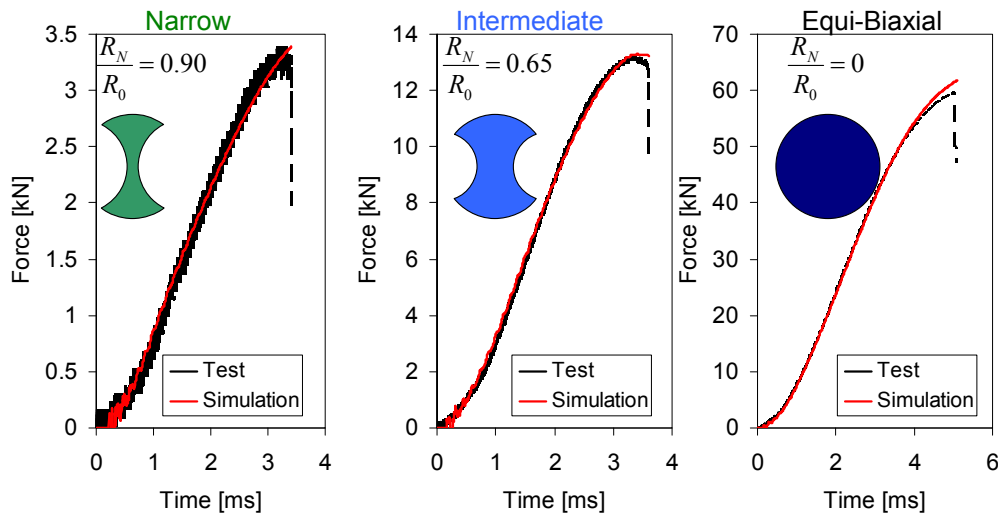
Middle Strain Rates = 164-309 /s

Figure 5.6: Comparison of dynamic experiments with the simulations of the same experiments for the set of highest strain rates tested (top) and the set of middle strain rates tested (bottom).

The state of stress for each model was extracted from the four elements closest to the center. For each of these elements, the effective plastic strain was plotted as a time history, and the specimen that had the highest effective plastic strain was selected. This procedure was followed because in-plane strain localization could easily bifurcate from one side of the center to the other, and this procedure was intended to capture the element that exhibited the most strain localization. Once the critical element was selected, the effective plastic strain, von Mises stress, third invariant, and pressure were exported for further processing. The stress parameters were processed into a time history of stress triaxiality and Lode parameter through the equations defined in Chapter 3. The effective plastic strain was differentiated with respect to time by typical finite difference method to obtain strain rate. The strain rate, stress triaxiality, and Lode parameter were then averaged. Averaging of stress triaxiality, Lode angle, and strain rate follows the same method described for quasi-static results. Eq. (3.17) from the quasi-static section is repeated here as Eq. (5.1), and Eq. (5.2) is given as the average strain rate, along the same method. This reflects the methodology set for in Bao (2003).

$$\eta_{AV} = \frac{1}{\bar{\varepsilon}_f^P} \int_0^{\bar{\varepsilon}_f^P} \eta d\bar{\varepsilon}^P \qquad , \qquad \bar{\theta}_{AV} = \frac{1}{\bar{\varepsilon}_f^P} \int_0^{\bar{\varepsilon}_f^P} \bar{\theta} d\bar{\varepsilon}^P \qquad (5.1)$$

$$\dot{\bar{\varepsilon}}_{AV} = \frac{1}{\bar{\varepsilon}_f^P} \int_0^{\bar{\varepsilon}_f^P} \dot{\bar{\varepsilon}} d\bar{\varepsilon}^P \qquad (5.2)$$

Once again, it is emphasized that these averages reflect quasi-temporal averages of a single point on the specimen that was deemed critical. They do not reflect spatial averages. The variation of stress triaxiality and Lode parameter with applied strain is shown in Chapter 3.

The fracture strain for each case was found by taking the fracture time determined from the experiment and extracting the effective plastic strain from the most critical element (described above) at that time.

5.5 Experimental Dynamic Fracture Locus

The average stress triaxialities and ductilities from section 5.4 are plotted in Fig. 5.7 for all of the conditions tested. Each dot, X, and triangle on this plot represents a different experiment, where the triaxiality is the average triaxiality for the most critical point in that experiment, and the ductility is the effective plastic strain for the same element at the time in the simulation that corresponds to fracture in the experiment. The condition of plane stress creates a unique relationship between Lode angle and stress triaxiality, so the punch tests (which are plane stress, at least at the outer surface) can reasonably be plotted in the two-dimensional projection found in Fig. 5.7. However, one must refer to the three-dimensional representation shown in Fig. 5.8 in order to fully understand the implications of the findings. All of the punch-style experiments fall on the pink line in Fig. 5.8, which represents the plane stress assumption. As can be seen, the punch experiments are confined to a narrow band of stress triaxiality, but span most of the Lode parameter in this coordinate system. Therefore, the differences observed due to strain rate effects in punch experiments can be seen as operating mostly around an axis parallel to the stress

triaxiality axis. The stress triaxiality of 0.45 (the case with the deepest cutouts in the specimen) corresponds to the Lode angle of almost unity. The stress triaxiality of 0.67 (the case of no cutouts in the specimen) corresponds to the Lode angle of negative unity. Therefore, the slight increase of ductility for the narrow specimens and decrease of ductility for the equi-biaxial case results in a twisting of the fracture locus. With this twisting, the ductility in positive Lode angles decreases while the ductility in negative Lode angles increases. This relationship is far more complex than has previously been reported in the literature; however, this is the first time that the effect of strain rate on fracture has been viewed in light of a stress triaxiality and Lode angle dependence.
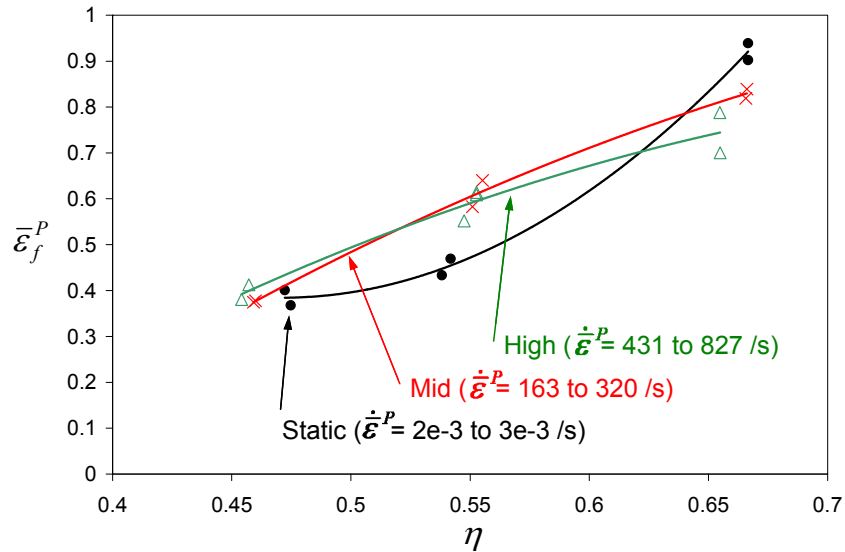
Figure 5.7: Fracture locus of DP780 showing the effect of strain rate under different stress triaxialities.
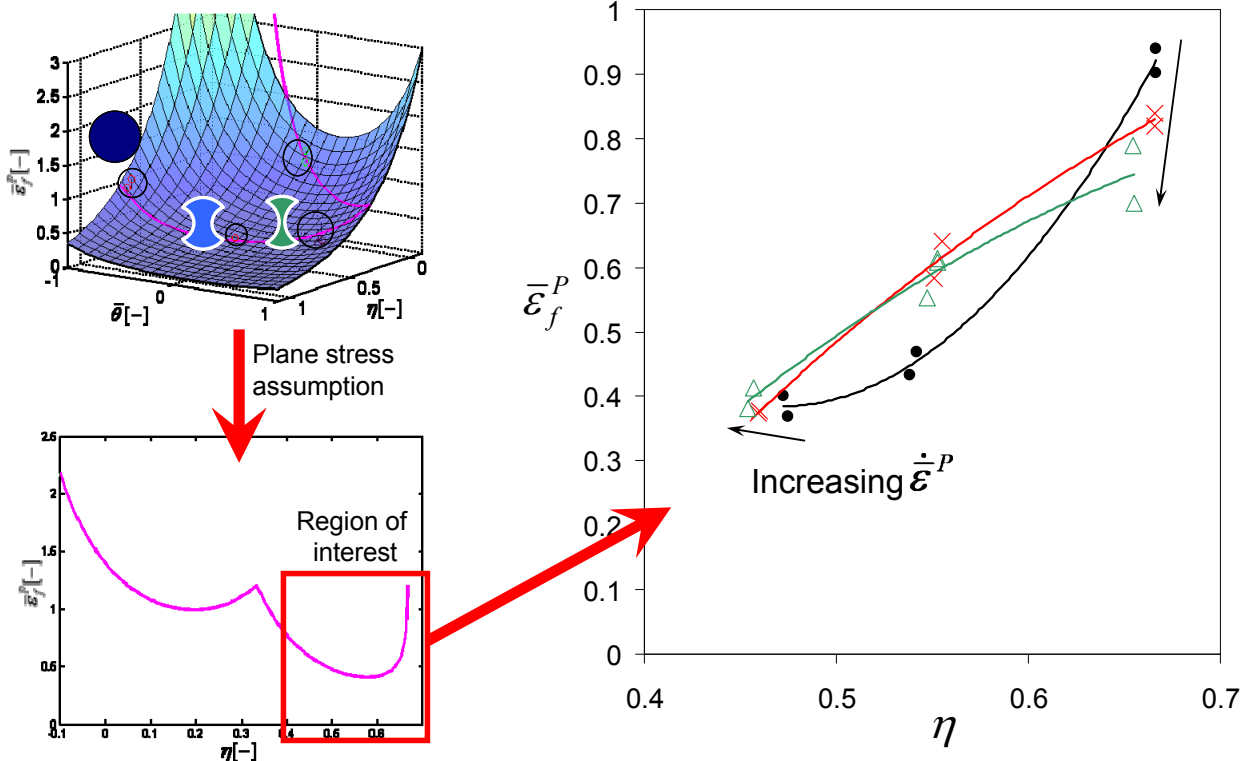
Figure 5.8: Relating figure 5.7 back to the quasi static fracture locus shows that increased strain rate tends to twist the fracture surface about an axis approximately parallel to the stress triaxiality axis.

5.6 Dynamic Modified Mohr-Coulomb Fracture Locus

The Modified Mohr-Coulomb Fracture Locus, originally derived by Bai (2008) can be easily modified for both the effect of strain rate on plasticity and the potential effects of strain rate on fracture. To understand how these effects are introduced, the derivation done by Bai (2008) will be revisited. The Mohr-Coulomb fracture criterion says that fracture occurs when the combination of the shear and normal stress on the fracture surface reaches a critical value, Eq. (5.3).

$$\max\left(\tau + c_1\sigma_n\right)_f = c_2 \tag{5.3}$$

In the space of stress invariants, Eq. (5.3) becomes

$$\overline{\sigma} = c_2\left[\sqrt{\frac{1+c_1^2}{3}}\cos\left(\frac{\pi}{6}-\theta\right) + c_1\left(\eta + \frac{1}{3}\sin\left(\frac{\pi}{6}-\theta\right)\right)\right]^{-1} \tag{5.4}$$

To transform the above equation into a criterion based on effective strain to failure, a constitutive law is required. In Bai's (2008) derivation, he used a constitutive law that depended on the Lode angle ($\overline{\theta}$). However, it was shown not to be necessary for the material with a quadratic yield

97

condition. It is assumed that the dependence of the equivalent stress on the equivalent strain and the strain rate can be written in a seperable form. In addition, the strain hardening curve is represented by a power hardening law.

$$\bar{\sigma} = \hat{\sigma}(\bar{\varepsilon}, \dot{\bar{\varepsilon}}) = C\bar{\varepsilon}^{n_H} f(\dot{\bar{\varepsilon}})$$ (5.5)

Eliminating $\bar{\sigma}$ between Eq. (5.4) and (5.5) gives the following for of fracture locus.

$$\bar{\varepsilon}_f^p = \left\{ \frac{C}{c_2(\dot{\bar{\varepsilon}})} f(\dot{\bar{\varepsilon}}) \left[\left(\sec\left(\frac{\bar{\theta}\pi}{6}\right) - 1 \right) \right] \left[\sqrt{\frac{1 + c_1(\dot{\bar{\varepsilon}})^2}{3}} \cos\left(\frac{\bar{\theta}\pi}{6}\right) + c_1(\dot{\bar{\varepsilon}})\left(\eta + \frac{1}{3}\sin\left(\frac{\bar{\theta}\pi}{6}\right) \right) \right] \right\}^{-\frac{1}{n_H}}$$ (5.6)

The present equation extends the quasi-static fracture locus derived by Bai (2008) to the dynamic one. In the special case in which the function $f(\dot{\bar{\varepsilon}})$ is given by the Cowper-Symonds law,

$$\bar{\sigma} = C\bar{\varepsilon}^{n_H} \left[1 + \left(\frac{\dot{\bar{\varepsilon}}}{\dot{\varepsilon}_0} \right)^{1/n_{CS}} \right]$$ (5.7)

Eq. (5.6) becomes

$$\bar{\varepsilon}_f^p = \left\{ \frac{C}{c_2(\dot{\bar{\varepsilon}})} \left[1 + \left(\frac{\dot{\bar{\varepsilon}}}{\dot{\varepsilon}_0} \right)^{1/n_{CS}} \right] \left[\left(\sec\left(\frac{\bar{\theta}\pi}{6}\right) - 1 \right) \right] \right.$$
$$\left. \left[\sqrt{\frac{1 + c_1(\dot{\bar{\varepsilon}})^2}{3}} \cos\left(\frac{\bar{\theta}\pi}{6}\right) + c_1(\dot{\bar{\varepsilon}})\left(\eta + \frac{1}{3}\sin\left(\frac{\bar{\theta}\pi}{6}\right) \right) \right] \right\}^{-\frac{1}{n_H}}$$ (5.8)

where the parameters $c_1(\dot{\bar{\varepsilon}})$ and $c_2(\dot{\bar{\varepsilon}})$ are no longer constant but depend on the strain rate. The key parameter relevant to the findings of the prior section is $c_1(\dot{\bar{\varepsilon}})$, which is responsible for rotating the fracture surface. The parameter $c_2(\dot{\bar{\varepsilon}})$ scales the fracture locus; it will slightly increase to compensate for the effect of $c_1(\dot{\bar{\varepsilon}})$ decreasing the fracture locus.

The damage will accumulate according to the damage accumulation rule described in Eq. (5.9).

$$D = \int_0^{\bar{\varepsilon}_f^p} \frac{d\bar{\varepsilon}^p}{\bar{\varepsilon}_f(\eta, \bar{\theta}, \dot{\bar{\varepsilon}})}$$ (5.9)

which includes the effect of strain rate, as found in Eq. (5.6).

5.7 Range of Strain Rates Possible with Current Method

To better understand the range of velocities that can be measured on the drop tower, a program was written in MATLAB that would estimate the strain rates achievable with various test parameters. The program is based around the force-displacement solution for a hemispherical punch into a plate suggested by Simonsen and Lauridsen (2000) and subsequently modified by Lee (2005). The nomenclature for this analysis is given in Fig. 5.9.
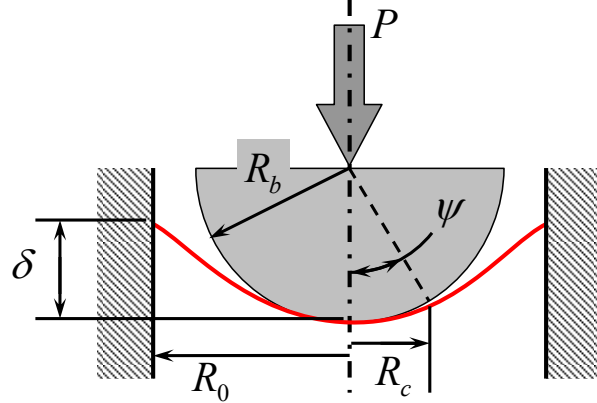
Figure 5.9: Schematic and nomenclature for analytical solution of the punching of a circular plate. After Lee (2005)

The relationship between R_c (the radius at which the punch is no longer in contact with the plate) and ψ (the angle at which the punch is no longer in contact with the plate) can be easily determined from basic geometry, Eq. (5.10).

$$R_c = R_b \sin(\psi) \tag{5.10}$$

Simonsen and Lauridsen (2000) gave the expression for the generalized membrane stress, given in Eq. (5.11) and the relationship between the contact angle ψ and the punch force (P) in Eq. (5.12).

$$N_0 = \frac{2\sigma_0 t_0}{\sqrt{3}} \tag{5.11}$$

$$\psi = \sin^{-1}\sqrt{\frac{P}{2\pi N_0 R_b}} \tag{5.12}$$

Simonsen and Lauridsen (2000) provided an expression for the punch deflection δ in terms of the contact angle ψ, but the one provided by Lee (2005) was found to be more accurate, so Lee's was used, see Eq. (5.13).

$$\frac{\delta(\psi)}{R_0} = \frac{\xi_0 \psi^2}{2} + \frac{2\xi_c^2\left(3 - \sqrt{\xi_c}\right)^2}{\xi_0}\left[\frac{1 - \sqrt{\xi_c}}{6\left(3 - \sqrt{\xi_c}\right)} - \frac{1}{9}\ln\left(\frac{2\sqrt{\xi_c}}{3 - \sqrt{\xi_c}}\right) + \frac{2\xi_c^{1.5}\left(1 + \sqrt{\xi_c}\right)}{9\xi_0^2\left(3 - \sqrt{\xi}\right)^2}\right] \qquad (5.13)$$

where the dimensionless radii are $\xi_0 \equiv R_b/R_0$ and $\xi_c \equiv R_c/R_0$.

This system was analyzed as a single-degree-of-freedom dynamic system in which the stiffness is given by Eq. (5.13). The differential equation governing the dynamics of the drop mass encountering the specimen is given by Eq. (5.14):

$$P(\delta) = M\ddot{\delta} \qquad (5.14)$$

The discrete form of Eq. (5.14) is Eq. (5.15):

$$P_i = M\ddot{\delta}_i \qquad (5.15)$$

where the mass M is constant throughout the experiment. The acceleration $\ddot{\delta}$ is found by application of Eq. (5.16).

$$\ddot{\delta}_i = \frac{\dot{\delta}_{i+\frac{1}{2}} - \dot{\delta}_{i-\frac{1}{2}}}{\Delta t} = \frac{\dfrac{\delta_{i+1} - \delta_i}{\Delta t} - \dfrac{\delta_i - \delta_{i-1}}{\Delta t}}{\Delta t} \qquad (5.16)$$

Substituting Eq. (5.16) into Eq. (5.15) and solving for δ_{i+1} gives Eq. (5.17):

$$\delta_{i+1} = \frac{P_i}{M}(\Delta t)^2 + 2\delta_i - \delta_{i-1} \qquad (5.17)$$

Once the displacement was found for time step $i+1$, the corresponding force was found by applying Eq. (5.12) and (5.13).

Based on the assumption of membrane tension and vertical displacement of material points, Simonsen (2000) proposed that the normal strain in the radial and thickness directions could be approximated as Eq. (5.18), and the tangential and shear strains could be approximated as Eq. (5.19).

$$\varepsilon_{rr} = -\varepsilon_{tt} = \ln\left(\frac{1}{\cos\psi}\right) \qquad (5.18)$$

$$\varepsilon_{\theta\theta} = \varepsilon_{\theta r} = 0 \qquad (5.19)$$

Once the strain was found, the radial strain rate was approximated according to Eq. (5.20):

$$\dot{\varepsilon}_i = \frac{\dot{\varepsilon}_i - \dot{\varepsilon}_{i-1}}{\Delta t} \tag{5.20}$$

For all cases, the Δt was taken to be 0.012 milliseconds, which resulted in a different amount of integration steps, depending on how long each of the conditions was.

Because the case of a hemisphere pushing into a circular plate without cutouts was the only condition that an analytical solution existed for, that was the only condition that was analyzed in this way. The circular plate absorbs more energy than any of the cases with cutouts, so it is anticipated that it will have the lowest strain rate. The results are summarized in Fig. 5.10, which shows the effect of various geometrical effects on the maximum strain rates achievable by the current drop tower for the highest drop mass and for the highest velocity of the machine. Note that the die radius used in this study was 24.5 mm (closest to the red dot-dash line), and that the ratio R_0 / R_b used in the current study was 1.1. Ratios of R_0 / R_b less than 1 are impossible because the radius of the punch would be greater than the radius of the die.
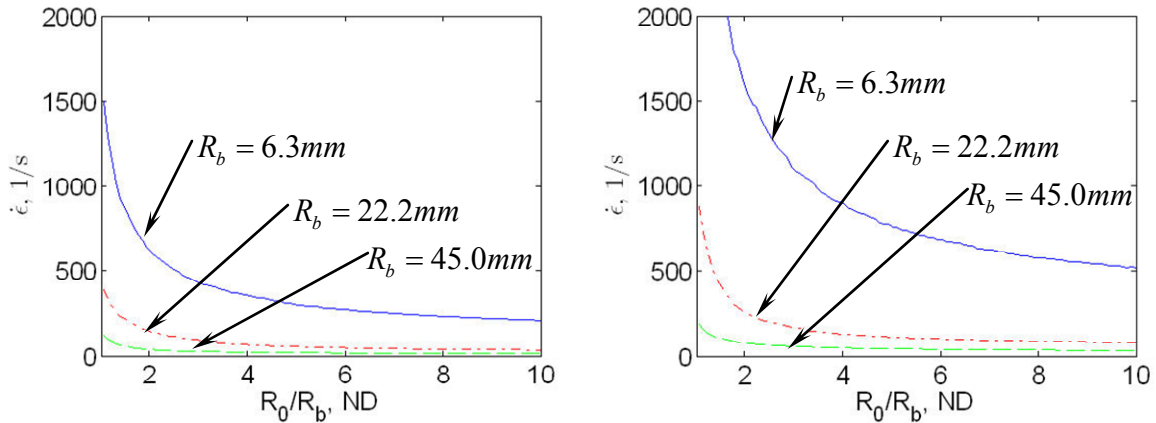
Figure 5.10: Strain rates that the drop tower is capable of achieving for punching a circular plate with various punch radii (R_b) and die radii (R_0). The plot on the left corresponds to the maximum drop mass with the corresponding maximum drop velocity. The plot on the right corresponds to the maximum drop velocity with the corresponding drop mass.

An important conclusion from this section is that there is a very wide range of strain rates achievable if different die and punch diameters are chosen. The strain rates achievable in the drop tower in the current thesis were bounded between 163-827 s^{-1} because the strain rate was modified only through changes in initial velocity and mass. Die and punch radii were chosen beforehand and held constant for all conditions. The lower bound came from the constraint that there is a maximum mass available in the drop tower, so there is a minimum critical energy to fracture. For example, some of the low strain rate conditions were exactly at the critical energy to fracture. Still lower strain rates could have been achieved by using a lower-diameter die. The upper bound of the strain rates was limited by the maximum velocity of the drop tower. This bound could have been increased by using a smaller die.

5.8 Conclusions

A novel methodology has been laid out whereby fracture in sheet metals can be tested over a wide range of stress states and strain rates. The stress state can be varied over a wide range of Lode parameters and a narrow range of stress triaxialities. A range of dynamic strain rates spanning 163-827 s^{-1} has been demonstrated, and a much wider range is achievable given different punch and die choices.

The new procedure is based on an inverse method, in which simulations of experiments are used to determine critical testing parameters. The application of this inverse method requires a good plasticity model that accounts for all mechanical effects experienced in the experiment, including strain rate effects. For these effects, the reader is referred to Chapters 2 and 4.

A very complex relationship between stress triaxiality, Lode parameter, strain rate, and ductility has been found. This relationship shows that the fracture three dimensional fracture locus twists with strain rate, resulting in reduced ductility with positive Lode angles and increased ductility in negative Lode angles.

Chapter 6

Conclusions and Future Work

6.1 Introduction

This chapter is divided into two major sections: conclusions and future work. The conclusions review some of the major accomplishments of the prior chapters. The section on future work reviews some possible directions that this work could take in the future and comments briefly on some of it that is already underway. While this work is believed to be complete, there are always paths that can be further developed and new questions that are raised. The section on future work is intended to help address some of these questions.

6.2 Conclusions

There are a number of important conclusions that fall out from the prior chapters, and they will be summarized below. The conclusions fall into two main categories: general conclusions and particular conclusions. The general conclusions represent major contributions to the literature and are intended to provide guidance and experience to future researchers. They tend to focus on methodology. The particular conclusions are findings about the particular material that was tested and are believed to be of interest to those who would apply this data in simulations or do further research on DP780 by US Steel.

6.2.1 General Conclusions

An overall methodology has been laid out and demonstrated for the determination of the effect of strain rate on fracture for a variety of multi-axial states of stress. This method relies very heavily on punching-style experiments. Along the way, the static fracture locus was determined by a parallel method in which a butterfly-shaped specimen is subjected to various combinations of tension and shear. It has been shown that other than for a shear fracture experiment, the butterfly method is redundant with the punch-style experiment. Therefore, a procedure similar to that presented in Chapter 1 is outlined in Fig. 6.1 with the exception that it excludes butterfly experiments for the fracture characterization. It is noted in Fig. 6.1 that dynamic plasticity must be studied. While the sample material in this thesis appeared to be strain rate insensitive over the range of strain rates studied, it is necessary to assess the effect of strain rate on plasticity in the general case, in which the material may experience a much higher sensitivity. The present

experimental technique would work equally well for strain rate sensitive and strain rate insensitive materials.

It should be noted that because the punch tests are not fully capable of spanning the states of stress necessary to model fracture that a new shear experiment is recommended for the future. The development of a shear fracture experiment will be the subject of future research.

```
┌─────────────────┐        ┌─────────────────┐
│                 │        │    Dynamic      │
│ Static Plasticity│──────▶│   Plasticity    │
│                 │        │                 │
└─────────────────┘        └─────────────────┘
        │                          │
        ▼                          ▼
┌─────────────────┐        ┌─────────────────┐
│  Static Punch   │──────▶│ Dynamic Punch   │
│   Fracture      │        │    Fracture     │
└─────────────────┘        └─────────────────┘
```
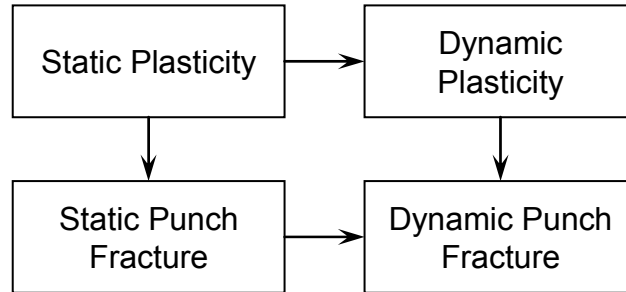
Figure 6.1: Recommended procedure for the determination of a dynamic fracture envelope.

In addition to the procedure that was developed, Chapter 3 demonstrated that punch style and butterfly style experiments agree quite well when plotted in the three dimensional space of stress triaxiality, Lode parameter, and ductility. This has brought the academic community together with the sheet metal forming community, and it has also shown the necessity of a three-dimensional fracture locus, rather than the two-dimensional locus traditionally used by the sheet metal forming industry.

It was also shown in Chapter 3 that while the butterfly experiments are sufficient to calibrate a three-dimensional fracture locus, punch-style experiments alone are not. A single point (most preferably shear) is necessary in addition to the punch-style experiments for a full three-dimensional calibration of the fracture locus. However, it has been shown that more than two or three Hasek experiments are redundant. Therefore, there is a recommendation to the sheet metal community to reduce the number of punch experiments traditionally done and instead add an in-plane shear fracture test.

In Chapter 5, it was shown that the dependence of ductility on stress triaxiality, Lode angle, and strain rate is far more complex than previously thought. While positive Lode angles reduce ductility, negative Lode angles tend to increase ductility.

Chapter 2 unveiled the use of a biaxial plasticity specimen that has no thickness reduction in the gage section. This specimen holds the potential to contribute to the understanding of full-sheet plasticity parameters rather than assuming that material properties are homogenous through the thickness of the sheet.

6.2.2 Particular Conclusions

Chapter 2 demonstrated that US Steel DP780 can be characterized as a Hill '48 material with in-plane isotropy. A full hardening curve and Hill coefficients were delivered in that chapter.

Chapter 3 delivered the MMC coefficients for US Steel DP780, and showed the applicability of this model for both punch-style and butterfly-style experiments.

Chapter 4 demonstrated a method being developed by Bordier (2009) for dynamic double shear plasticity testing and showed that the test material is very close to strain rate independent for the range of strain rates up to almost 600 s^{-1}.

6.3 Future Work

The first and most straightforward application of this thesis would be to simply apply it to a different material. Application of this methodology to a different material would show if the findings regarding the dependence of fracture on strain rate are generalizable to other grades of AHSS, other steels, or metals in general.

Another pressing need is for further development of the effect of strain rate on plasticity in the intermediate range. As outlined in Chapter 1, researchers are struggling to develop tensile testing experiments in the intermediate range that do not suffer from large vibrations due to dynamics. Some researchers use upsetting tests either in high-speed hydraulics or in split Hopkinson bars, but upsetting tests can be challenging for the in-plane direction for sheet metals.

Work is already underway to develop more advanced techniques for testing the effect of strain rate on plasticity within the Impact and Crashworthiness Laboratory (ICL). One contribution is the work of an undergraduate, (Chan, 2009), in which a fixture and specimen was designed for tensile testing in the drop tower. With this fixture, the specimen is bent into a "U" shape, with dogbone specimens on the vertical sides of the "U", which are subjected to tension when the hemispherical end of the drop tower tup pushes into the bottom of the "U". See Fig. 6.2 for a schematic of this fixture. This fixture promises to exactly span the intermediate range, with maximum strain rates near 1000 s^{-1}. However, this device remains unproven and has several technical hurdles yet to overcome. The first and largest technical hurdle will be the fact that the impact of the hemispherical tup onto the bent sheet metal specimen will result in bending waves propagating through the specimen. While the bending waves can be partially accounted for by mounting strain gages on both faces of the specimen, simulations have shown that they will continue to introduce unwanted dynamic effects into the experiment.
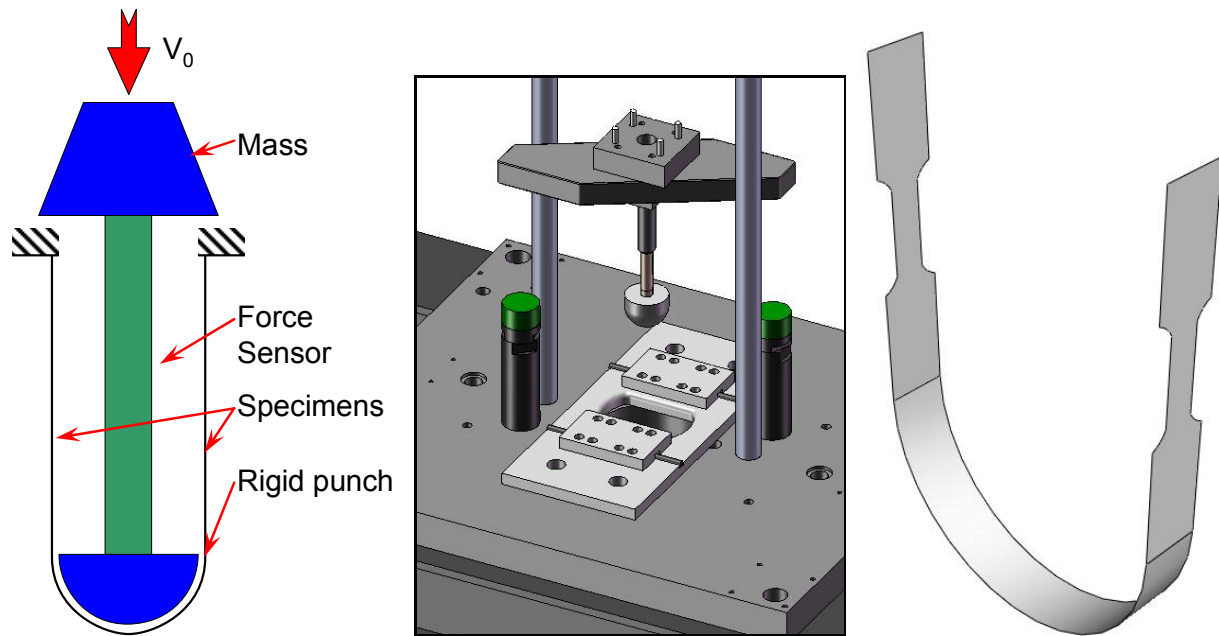
Figure 6.2: Fixture and specimens developed for tensile testing of sheet metals in a drop tower. The schematic shows how the drop mass impacts onto a curved specimen that is clamped on the top (left). The CAD model shows the clamping fixture, force sensor, and impacting tup in the context of the drop tower (center). The image on the right shows the curved specimen with dogbone specimens machined into the sides. After Chan (2009).

Another avenue of finding the effect of strain rate on plasticity is a dynamic shear test currently being developed by Bordier (2009). The experimental setup and preliminary work by Bordier's (2009) was described in Chapter 4. As mentioned in Chapter 4, the design is quite promising, but it is not yet fully mature and validated. This line of research will continue under the efforts of Bordier.

It was shown in Chapter 5 that the drop tower punch method of fracture characterization is capable of higher and lower strain rates than those tested in the current work. It would be of interest to take advantage of the effect of changing die sizes to explore strain rates higher and lower than those tested. While the figures in Chapter 5 showed a very large range of punch radius to die radius, it is recommended that this ratio be kept approximately constant to achieve similar histories of stress state. This is because a sufficiently small punch relative to the die would result in approximately equi-biaxial conditions even in specimens with large cutouts through most of the experiment.

Finally, collaboration has already begun with the group of Professor R. Radovitzky at MIT to use the existing experiments as validation for a Cohesive Zone approach to fracture.

Appendix A

Calibration of a Drop Tower Force Sensor

A.1 Abstract

A procedure was obtained from Instron (Banik, 2003) and applied to re-calibrate the 200 kN force sensor provided with the drop tower. As compared with the load cell installed on the MTS testing machine, the Instron drop tower force sensor was slightly nonlinear and measured approximately 17% less force than was applied.

A.2 Introduction

Force sensors can drift over years. The force sensors provided with the drop tower used for the main experimental work for this thesis were last calibrated in 2003 and were already three years overdue for a new calibration by the start of major drop tower testing. As well, the calibration certificates provided with the force sensors indicated that the force sensors had a slightly nonlinear force versus voltage output. Preliminary drop tests had shown forces that were lower than expected. The procedure "Work Instruction: Dynatup Force Verification Procedure Using Impulse DAQ Software," written by M. Banik at Instron and dated September 15, 2003 was used for the calibration of the 200 kN force sensor.

A.3 Procedure

Under construction
Before the force sensor could be calibrated, a plan needed to be developed to allow for the sensor to be loaded to high forces (in excess of 50 kN) with little risk of the sensor buckling, being overloaded, or being otherwise damaged. It was decided that the force sensor should not be simply crushed between platens because the stiffness of such a system could possible cause either the Instron force sensor or the MTS load cell to be overloaded accidentally. An early attempt at reducing the stiffness of the system was to introduce wood or bulk polymers (e.g. one inch thick nylon) between the MTS load cell and the Instron force sensor. However, these materials were too strain rate sensitive, and it required constant adjustment of the crosshead location in order to maintain a force steady enough for readout. Instead, an aluminum part was created with a large through-hole and a chamfer at the top of the through-hole. This part was crushed between a flat platen on top and a hardened hemispherical punch on the bottom. (The chamfer was against the hemisphere.) The configuration is shown in Fig. A.1. The aluminum proved to be rate insensitive enough to allow a constant force while the whole system proved to be flexible enough that it was easily loaded to the appropriate force through displacement

control. However, ONLY THE THUMB WHEEL WAS USED TO CONTROL THE DISPLACEMENT OF THE MTS CROSSHEAD; THE ARROWS (FAST JOG) WERE NOT USED AND ARE ILL-ADVISED. It is strongly recommended that anyone calibrating the force sensor with this procedure practice by configuring the system and very slowly using the thumb wheel of the MTS machine to go to target forces below the capacity of either MTS load cell or Instron force sensor.

This procedure has only been validated up to 80 kN, and safety can't be assured higher than that. It is critical that the load path be well centered and that appropriate safety precautions be taken in the event that the elastic energy of the system is unexpectedly released.
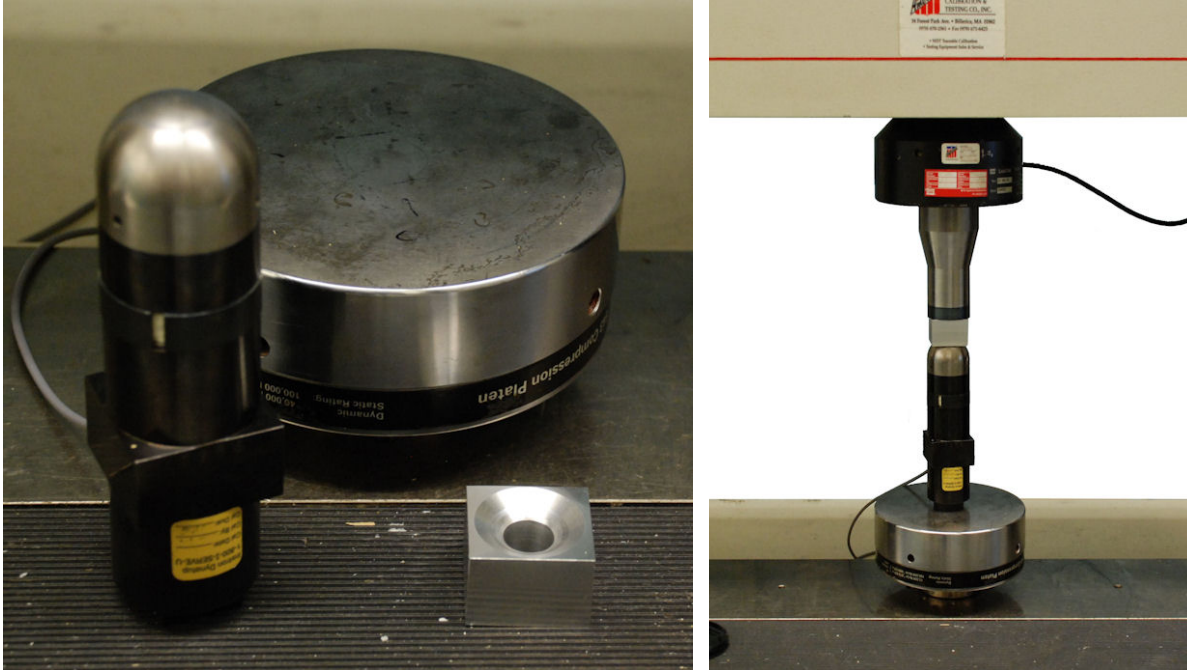
Figure A.1: Hardware and installation of the Instron force sensor in series with the MTS load cell.

The tup cable was extended by adding an additional DSUB-9 cable so that it could reach from the MTS load frame to the ISCU attached to the drop tower. The platens and force sensor were arranged in the MTS load frame in the configuration shown above. The file Impulse.ini on the drop tower computer was modified so that a test could be run for 30 seconds. The velocity flag detector was located at an appropriate position, and the drop mass was picked up so that the flag was at an appropriate height above the flag detector. A "velocity test" was set up in the Impulse software on the dropt tower computer. The drop tower data acquisition was started by dropping the mass so that the velocity flag went through the detector. During the course of the next thirty seconds, the Instron force sensor was then loaded to a target force. The force measured by the MTS load cell system was then recorded by hand based on the readout of the computer associated with the MTS system. The force recorded by the Instron force sensor was retrieved from the Impulse software after the test. This procedure was repeated several times to find many pairs of MTS load cell versus Instron force sensor force measurements. The details of this procedure relating to the operation of the drop tower and Impulse software can be found in Banik (2003).

A.4 Results

The Instron data acquisition software (called Impulse) requires the input of a "tup calibration factor," which allows the user to adjust the calibration factor slightly for different anticipated maximum forces. By executing the above procedure with different tup calibration factors, it became clear that the tup calibration factor merely scales the data. Therefore, it was found that the data could be retrospectively changed from one tup calibration factor to another simply by multiplying the data by a ratio of the desired one to the one used during the experiment. Therefore, all results of the calibration were taken at the same tup calibration factor, or they were multiplied by the appropriate factor to act as if they had been. The tup calibration factor used for the calibrations was 117.219 kN.

The forces measured on the MTS load cell are plotted against the forces measured by the Instron force sensor ("tup") in Fig. A.2. Ideally, the relationship will start at the origin and have a slope of unity, and this relationship is plotted in the figure and labeled "ideal." The difference between the measured points and the ideal curve can be clearly seen. Because of the slightly nonlinear nature of the Instron force sensor, a quadratic equation with a zero intercept was fit through the data. Use of the quadratic equation is believed to eliminate the need for different tup calibration factors for different anticipated force magnitudes in the experiments. Applying the quadratic correction equation to the measured Instron force sensor data resulted in the corrected data also shown in Fig. A.2. The correction equation is given in Eq. (A.1).
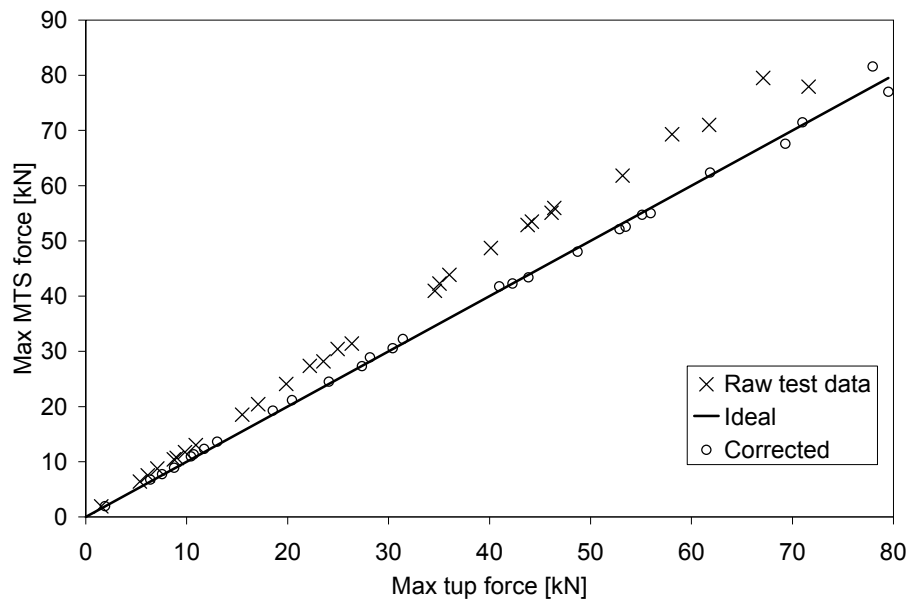
Figure A.2: Calibration results of the MTS Load cell versus the Instron force sensor ("tup") showing original measurement and the same measurement when adjusted with the suggested quadratic equation.

$$F[kN] = -0.00183142 \left(F_{measured} \frac{117.219}{TupCalFactor} \right)^2 + 1.2704764 \left(F_{measured} \frac{117.219}{TupCalFactor} \right)$$

(A.1)

A.5 Recommendations

The equation A.1 should be applied to all force data measured on the drop tower by the 200 kN force sensor. The 15 kN force sensor should be calibrated in a similar fashion. Both force sensors should be verified before any large testing series and periodically. The calibration of the 200 kN force sensor should be verified if attempting to measure forces much greater than 80 kN.

References

1. ABAQUS, Reference manuals v6.4-1, ABAQUS Inc, 2003.
2. Alves, M., Jones, N. "Influence of hydrostatic stress on failure of axisymmetric notched specimens." Journal of the Mechanics and Physics of Solids 47 pp 643-667.
3. ASTM "Standard Test Methods for Tension Testing of Metallic Materials [Metric]" ASTM International E 8M-04
4. Bai, Y. (2008) "Effect of Loading History on Necking and Fracture." Ph.D. Thesis (MIT).
5. Bao, Y. (2003) "Prediction of Ductile Crack Formatio in Uncracked Bodies." Ph.D. Thesis (MIT).
6. Banabic, D. et. Al. (2000) "Formability of Metallic Materials." Springer, Berlin.
7. Banik, M (2003) "Work Instruction: Dynatup Force Verification Procedure Using Impulse DAQ Software." Instron.
8. Bleck, W. and Larour, P. (2003) "Measurement of the mechanical properties of car body sheet steels at high strain rates and non ambient temperature." J. Phys. IV France 110 pp 489-494.
9. Bleys, P, Kruth, J-P., Lauwers, B., Schacht, B., Balasubramanian, V., Froyen, L., Humbeeck, J. V. (2006) "Surface and Sub-Surface Quality of Steel after EDM." Advanced Engineering Materials, Vol 8, N 1-2 pp 15-25.
10. Bodner, S. R. and Symonds, P. S. (1978) "Experiments on Viscoplastic Response of Circular Plates to Impulsive Loading." J. Mech. Phys. Solids Vol. 27, pp 91-113.
11. Bordier, R. (2009) Personal correspondence.
12. Bronkhorst, C. A., Cerreta, E. K., Xue, Q., Maudlin, P. J., Mason, T. A., Gray III, G. T. (2006) "An experimental and numerical study of the localization behavior of tantalum and stainless steel." International Journal of Plasticity 22, pp 1304-1335.
13. Chan, J. J. (2009) "Design of Fixtures and Specimens for High Strain-Rate Tensile Testing on a Drop Tower." B.S. Thesis (MIT).
14. Chen, M., and Zhou, D. J. (2008) "AHSS Froming Simulation for Shear Fracture and Edge Cracking." Great Designs in Steel 2008 Seminar Presentations.
15. Cheng, J., Nemat-Nasser, S., Guo, W. (2001) "A unified constitutive model for strain-rate and temperature dependent behavior of molybdenum." Mechanics of Materials 33 pp 603-616.
16. Choi, I. D., Bruce, D. M., and Kim, S. J., Lee, C. G., Park, S. H., Matlock, D. K., and Speer, J. G. (2002) "Deformation Behavior of Low Carbon TRIP Sheet Steels at High Strain Rates." ISIJ International, Vol. 42 (2002), No. 10, pp 1483-1489.
17. Cowper, G. R. and Symonds, P. S. (1958) "Strain hardening and strain rate effects in the impact loading of cantilever beams." Brown, University, Division of Applied Mechanics No. 28.
18. Erichsen, A. M. (1914) "Ein neues Pruefverfahren fuer Feinbleche [A new test for thin sheets (in German)]" Stahl und Eisen 34, 879-882.
19. Follansbee, P. S., Kocks, U. F. (1988) "A constitutive description of the deformation of copper based on the use of the mechanical threshold stress as an internal state variable." Acta metal. Vol. 36, No. 1 pp 81-93.
20. Gurson, A. L. (1977) "Plastic Flow and Fracture Behavior of Ductile Materials Incorporating Void Nucleation, Growth and Interaction". Ph.D. Thesis. (Brown University).

21. Hancock, J. W. and Mackenzie, A. C. (1976) "On the Mechanisms of Ductile Failure in High-Strength Steels Subjected to Multi-Axial Stress-States." J. Mech. Phys. Solids. Vol 24 pp 147-169.
22. Hasek, V. (1973) "On the strain and stress states in drawing of large unregular sheet metal components (in German)." Berichte aus dem Institute fuer Umformtechnik, Universitaet Stuttgart, Nr. 25, Essen, Girardet.
23. Hasek, V. (1978) "Untersuchung und theoretische Beschribung wichtiger Einflussgroessen auf das Grenzformaenderungsschaubild [Research and theoretical description concerning the influences on the FLDs (In German)]." Blech Rohre Profile 25, 213-220, 285-292, 493-399, 617-627.
24. Hopperstad, O. S., Borvik, T, Langseth, M., Lubibes, K., Albertini, C. (2003) "On the influence of stress triaxiality and strain rateon the behaviour of a strucutral steel. Part I. Experiments." European Journal of Mechanics 22 pp 1-13.
25. Jacquemin, J. (2007) "Experimental Investigation on the Effect of Shear Stresses on the Yield Behavior of Anisotropic Austenitic Stainless Steel Sheets." Rapport de Stage D'Option Scientifique (Ecole Polytechnique).
26. Johnson, G. R., Cook, W. H. (1985) "Fracture Characteristics of Three Metals Subjected to Various Strains, Strain Rates, Temperatures and Pressures." Engineering Fracture Mechanics Vol. 21, No. 1, pp. 31-48.
27. Larour, P., Verleysen, P., Vermeulen, M., Gomes, M.A.R., Wedemeier, A. Geoffroy, J-L., Bleck, W. (2004) "Influence of Pre-Straining and Microstructure on the Dynamic Properties of High Strenght Sheet Steels." Materials Science & Technology Conference Proceedings.
28. Lee, W. S. and Wang, B. K. (2007) "High strain rate mechanical properties of austenitic manganese steel." Materials Science and Technology Vol. 23, No. 2, pp 151-157.
29. Lee, Y.W. (2005) "Fracture Prediction in Metal Sheets." Ph.D. Thesis (MIT).
30. McClintock, F. A. (1968) "A Criterion for Ductile Fracture by the Growth of Holes." Journal of Applied Mechanics. June pp 363-371.
31. McClintock, F. A. and Zheng, Z. M. (1993) "Ductile fracture in sheets under transverse strain gradients." International Journal of Fracture, Vol 64 pp 321-337.
32. Mirza, M. S., Barton, D. C. (1996) "The effect of stress triaxiality and strain-rate on the fracture characteristics of ductile metals." Journal of Materials Science 31 pp 453-461.
33. Mohr, D., Dunand, M, and Kim, K.H. (2008) "Evaluation of Associated and Non-associated Quadratic Plasticity Models For Advanced High Strength Steels Sheets under Multi-axial Loading." Submitted to the International Journal of Plasticty.
34. Mohr, D and Henn, S. (2007) "Calibration of Stress-triaxiality Dependent Crack Formation Criteria: A New Hybrid Experimental-Numerical Method." Experimental Mechanics Vol 47, pp 805-820.
35. Mohr, D. and Oswald, M. (2008) "A new experimental technique for the multi-axial testing of advanced high strength steels." Experimental Mechanics, Vol 48 N 1 pp 65-77.
36. Nakazima, K., Kikuma, T., Hasuka, K. (1971) "Study on the formability of steel sheets." Yawat Tech. Rep. No. 284, 678-680.
37. Needleman, A., Tvergaard, V. (1984) "An analysis of ductile rupture in notched bars." J. Mech. Phys. Solids Vol. 32 No. 6, pp 461-490.
38. Nemat-Nassar, S. Guo, W. G., and Cheng, J. Y. (1999) "Mechanical Properties and Deformation Mechanisms of a Commercially Pure Titanium." Acta Mater. Vol. 47, No. 13, pp. 3705-3720.

39. Nowacki, W. K., Gadaj, S. P., Luckner, J., Nowak, Z., Perzyna, P., Pecherski, R. B. (2006) "Effect of Strain Rate on Ductile Fracture." Report of the Award No FA 8655-05-1-3049 from the European Office of Aerospace Research and Development.

40. Outeiro, J. C., Umbrello, D., and M'Saoubi, R. (2006) "Experimental and FEM Analysis of Cutting Sequence on Residual Stresses in Machined Layers of AISI 316L Steel." Materials Science Forum Vols. 542-525 pp 179-184.

41. Park, Y. B., Park, J., and Chin, K. G. (2002) "Through-Thickness Texture Inhomogeneity and its Effect on Formability in IF Steel Sheets." Materials Science Forum Vols. 408-412 pp 1079-1084.

42. Qiu, H, Enoki, M., Mori, H., Takeda, N. and Kishi, T. (1999) "Effect of Strain Rate and Plastic Pre-Strain on the Ductility of Structural Steels." ISIJ Internationl, Vol. 39, No. 9, pp 955-960.

43. Rice, J. R. and Tracey, D. M. (1969) "On the Ductile Enlargement of Voids in Triaxial Stress Fields." J. Mech. Phys. Solids Vol 17, pp 201-217.

44. Roos, E. and Mayer, U. (2003) "Progress in testing sheet material at high strain rates." J. Phys IV France. 110 pp 495-500.

45. Rusinek, A. Nowacki, W. K., Gadaj, P., Klepaczko, J. R. (2003) "Measurement of temperature coupling by thermovision and constitutive relation at high strain rates for the dual phas sheet steel." J. Phys. IV. 110 pp. 411-416.

46. Rusinek, A., Zaera, R., Klepaczko, J. R. (2007) "Constitutive relations in 3-D for a wide range of strain rates and temperatures – Application to mild steels." International Journal of Solids and Structures 44 pp 5611-5634.

47. Schmid, K. (2008) "Evaluation of DP780 and DP980 for B-Pillars". Proceedings of Great Designs in Steel.

48. Shaw, J. (2003) "ULSAB-Advanced Vehicle Concepts ULSAB-AVC". Proceedings of Great Designs in Steel.

49. Simonsen, B. C. and Lauridsen, L. P. (2000) "Energy Absorption and Ductile Failure in Metal Sheets Under Lateral Indentation by a Sphere," International Journal of Impact Engineering Vol. 24, pp. 1017-1039.

50. Steinberg, D. J., Lund, C. M. (1988) "A constitutive model for strain rates from 10-4 to 106 s-1." J. Appl. Phys Vol 65 No. 5, pp 1528-1533.

51. Sutton, M. A., McNeill, S. R., Helm, J. D., Chao, Y. J. (2000) "Advances in Two-Dimensional and Three-Dimensional Computer Vision." Photomechanics, Topics Appl. Phys. Vol. 77, pp 323-372.

52. Symonds, P. S. and Chon, C. T. (1974) "Approximation techniques for impulsive loading of structures of time-dependent plastic behaviour with finite deflections." Mechanical Properties at High Rates of Strain, The Institute of Physics, London and Bristol, Oxford, April 1974. No. 21, pp 299.

53. Talonen, J, Nenonen, P., Pape, G., and Haenninen, H. (2005) "Effect of Strain Rate on the Strain-Induced gamma to alpha prime Martensite Transformation and Mechanical Properties of Austenitic Stainless Steels." Metallurgical and Materials Transactions, Vol. 36A, No. 2, pp 421.

54. Van Slycken, J., Verleysen, P., Degrieck, J., Bouquerel, J. (2006) "Constitutve equations for multiphase TRIP steels at high rates of strain." J. Phys. IV France 134 pp 69-74.

55. Van Slycken, J., Verleysen, P., Degrieck, J., Bouquerel, J. De Cooman, B. C. (2007) "Dynamic response of aluminum containing TRIP steel and its consituent phases." Materials Science and Engineering A 430-461 pp 516-524.
56. Woertz, J. C. (2002) "Quasi-static Tearing Tests of Metal Plating." M.S. Thesis (MIT).
57. Xue, L. (2007) "Ductile Fracture Modeling - Theory, Experimental Investigation and Numerical Verification." Ph.D. Thesis (MIT).
58. Yan, B. and Urban, D. (2003) "Characterization of Fatigue and Crash Performance of New Generation High Strength Steels for Automotive Applications." AISI/DO Technology Roadmap Program Final Report.
59. Yan, B. and Xu, K. (2003) "High Strain Rate Behavior of Advanced High Strength Steels for Automotive Applications." Iron and Steel Maker, June, pp 33-42.
60. Zerilli, F. J. and Armstron, R. W. (1986) "Dislocation-mechanics-based constitutive relations for material dynamics calculations." J. Appl. Phys. Vol 61 No. 5 pp 1816-1825.
61. Zhao, H. (1997) "A consititutive model for matals over a large range of strain rates Identification for mild-steel and aluminum sheets." Materials Science and Engineering A230 pp 95-99.
62. Zhao, H., Gary, G. (1996) "The testing and behaviour modeling of sheet metals at strain rates from 10^{-4} to 10^{4} s^{-1}." Materials Science and Engineering A207 pp 46-50.